Development and Testing of a Biologic Dosimetric Phantom for Proton and Ion Beam Therapy

Division of Surgery & Interventional Sciences,
Faculty of Medical Sciences
University College London (UCL)

Doctorate Research Degree

Candidate

Thiago Viana Miranda Lima
ID Number 722745/2

Thesis Advisors

Prof. Gary Royle
Dr. Kate Ricketts

Co-Advisors

Prof. Manjit Dosanjh
Dr. Alfredo Ferrari

Thesis defended on 21 April 2016
in front of a Board of Examiners composed by:

Mr. Richard Amos
Dr. Andrzej Kacperek

Development and Testing of a Biologic Dosimetric Phantom for Proton and Ion Beam Therapy
Ph.D. thesis. University College London

Version: August 3, 2016

Author's email: thiago.lima.09@ucl.ac.uk

This work has been funded within the
ENTERVISION Initial Training Network
by the European Commission,
FP7 Grant Agreement N.264552.
The student has also being supported by
UCL and Welcome Trust ISSF
award number 097815/Z/11/B

Declaration

I, Thiago Viana Miranda Lima, confirm that the work presented in this thesis is my own. Where information has been derived from other sources, I confirm that this has been indicated in this thesis.

Date:

_____

Signed:

_____

Acknowledgements

I would like to express my appreciation and thanks to my supervisors Prof. Manjit Dosanjh, Dr. Alfredo Ferrari, Prof. Kate Ricketts and Prof. Gary Royle, I would like to thank you for encouraging my research and for allowing me to grow as a research scientist. I would especially like to thank all contributors that participated in different stages of this project in special Dr. A Mairani, Dr. T Boehlen, Prof. F Marchetto, Dr. A Fedynitch, Mr. L Morejon, Dr. V Vlachoudis, Dr. P Velten, Dr. Cirilli and Prof B Jones. Also my kindest gratitude for the help provided during the experiments by the Medical Physics Departments at both CNAO and HIT. A special thank you to Dr. I Dokic at Uni Klinikum Heidelberg for all support and help with the biological experiments. The Physics Department at INFN-To/University of Turin for their help and endurance during the production of several prototypes and modifications. To Ms. Bulling and Prof. Bernier at Genolier Clinique Geneva for the tests performed at their facility and ULICE Network Transnational Access for providing the beam time needed for this project.

This work has been funded within the ENTERVISION Initial Training Network by the European Commission, FP7 Grant Agreement N.264552. I was also supported by UCL and Welcome Trust ISSF award number 097815/Z/11/B

Finally, I would like to thank my family, particularly my wife Amy, for their help and support throughout the course of my PhD.

Abstract

The development of clinical treatment protocols for particle therapy depends on the availability and quality of radiobiological data. Studying available commercial and in-house phantoms, showed that the current solutions either lack dosimetry or this dosimetry introduces uncertainties to the biological results. Therefore new radiobiological tools with improved dosimetry response were required. The chosen material, the effect of detectors uncertainties and the impact of detectors? positions were studied so the effect of the introduced uncertainties in the measurements could be evaluated. The phantom was subsequently tested at different experiments with both protons and carbon ion beams where a number of dose fields were simulated and delivered. Simulated and measured doses were compared to establish accuracy of simulation. Finally, a clonogenic survival assay was performed to assess the viability and capabilities of the phantom. No disturbance was introduced in the cell region by the detectors where 95.3% of the cases were within the 95% confidence level. Additionally, the detector measurements were free from any disturbance arising from the adjacent detectors (sigma 0.76). When evaluating the simulation accuracy, a good agreement was obtained between measurements and dose modelling where the average dose deviation was between 1.05% and 2.39%. Superior effectiveness was obtained for protons and carbon ions in respect to X-rays (1.2 and 2 times for protons and carbon ions respectively) and the phantom was able to correlate the cell survival and dose deposition. Concluding, these results showed that the phantom limitations were accounted for which enabled the measured physical dose and the dosimetry in the cell compartment to be correctly correlated. The results demonstrate the superior dosimetry obtained in respect to other set-ups either by correctly describing the dose profile (additional 1.5% mean deviation due to dose delivery uncertainties) or by not introducing uncertainties in the beam path (up to $\pm$ 2%).

Contents

Chapter 1

Introduction

1.1 Aim

This chapter aims to provide the contextual background for the thesis. After a brief introduction of the principles of Hadron Therapy (HT) and its current status, the role of radiobiology in the patient dose calculation and its importance in Hadron Therapy will be considered.

1.2 Introduction to Hadron Therapy

Radiotherapy with protons or ions, also called Hadron Therapy, Particle Therapy or Ion Beam Therapy is, in principle, able to target the tumour more effectively while sparing surrounding normal tissues. Due to its physical properties (see section 1.2.1 below), ions can play an important part in providing good tumour/dose conformity while reducing the integral dose. The idea of using the superior depth dose for ions in relation to photons in medicine was first introduced by Robert Wilson (Wilson 1946). This concept is shown in Figure 1.1, which compares the difference between the energy deposition in relation to the depth for ions and electromagnetic radiation. Because ions have a defined range, they are the perfect candidate for treating deep-seated tumours and sparing organs and structures seated near the tumour site.

A further favourable factor for the use of ions in therapy are their improved

biological efficiency in cell killing (see section 1.2.2 below). This fact reiterates the importance of high precision in the dose delivery as this improved efficiency also affects the surrounding normal tissues (Schulz-Ertner et al. 2006). This improved efficiency is mainly owing to the increased ionisation density along the individual tracks of the ions, which introduces more clustered Deoxyribonucleic acid (DNA) damage, making it more difficult for the cell to repair (Kraft 2000). Besides the reduced repairability, ions are also expected to be less susceptible to biological characteristics known to reduce the sensitivity to radiation damages like the oxygenation level (Churchill-Davidson 1966) and cell cycle.

In addition to the presented positive aspects, the use of ions also presents some disadvantages. These are associated to range calculation uncertainties (Paganetti et al. 2002) and the errors associated with modelling biological efficiency and its translation into the calculated biological dose (Boehlen et al. 2012). The calculated biological dose is affected by either the dose calculation models (Paganetti et al. 2002; Carabe et al. 2012; Boehlen et al. 2012), or the uniqueness of the particle accelerator/dose delivery systems used (Rossi 2011). Tools to aid with the study of biological responses in conjunction with dosimetric information still need to be further developed in order to translate these findings into clinical practice and to help compare multi-centre systems.

1.2.1 Physical Properties

As described above, the energy deposition in matter by an ion is inversely proportional to its velocity, allowing a small deposition at the beam entrance and high deposition at the end of its path (known as Bragg Peak (BP), which can be seen in Figure 1.1 in relation to other radiation types). In the clinical scenario, since the width of the BP is smaller than the width of the tumour and its position is related to the initial kinetic energy of the beam, it is possible to arrange a combination of different peaks to cover the whole extent of the tumour (called Spread-out Bragg Peak (SOBP)).

Compared to ions, electromagnetic radiation interacts with the matter

by stochastic processes (mainly Photoeletric and Compton) that yield an exponential decay of absorbed dose with penetration (Kraft 2000). Around the clinical energies (circa hundreds of MeV), the energy loss of ions is mainly influenced by the electronic collision, which can be described by the Bethe-Bloch formula:

$$\frac{dE}{dx} = \frac{4\pi Z_{eff}^2 e^4 Z N}{m_e v^2} \ln \frac{2mv^2}{I} + \text{relativistic terms} \tag{1.1}$$

Where $\frac{dE}{dx}$ is the energy loss per length, Z is the target atomic number, N the electron density of the target, m_e and e the mass and charge of the electron, $v = \beta c$ the projectile velocity and I is the mean ionisation potential. Z_{eff} corresponds to the effective projectile charge which can be approximated by the Barkas formula:

$$Z_{eff} \simeq Z(1 - \exp -125\beta Z^{\frac{2}{3}}) \tag{1.2}$$

The Bethe-Bloch equation is strongly shaped by the $\frac{1}{v^2}$ and Z_{eft} dependency that provides the increase of dose deposition at the end of the particle's path where its velocity is smaller.

Linear Energy Transfer (LET)

The rate of loss of energy, known as the Linear Energy Transfer (LET), depends on the energy and type of radiation as well as the material. LET is described as the average energy deposited per unit of track length of radiation. Its unit of measurement is $keV/\mu m$. As the ion beam loses its energy along its path, the rate of the energy loss, as described above (Equation 1.1) will increase, and therefore the LET increases as the particle continues to slows down.

Hence, the increased LET at the end of the particles' track. The use of LET to describe the density of ionisation is especially important to understand the biological effects of radiation. This happens because the different effectiveness of different radiations are dependent on the radiation's type and LET. Usually, directly ionising radiation (charged particles) have higher LET than indirectly

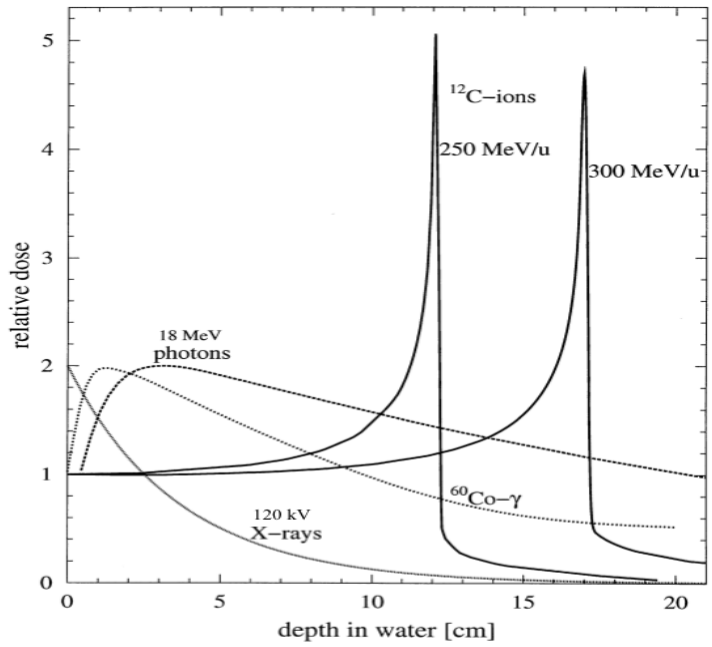

Figure 1.1. Comparison of the depth dose profiles for different particle types (Kraft 2000).

ionising radiation (X and γ rays) because of their greater energy deposition along the track (IAEA 2010).

Absorbed dose

The amount of energy absorbed per mass is known as the radiation dose. The Radiation dose is the energy (Joules) absorbed per unit mass of tissue and has the (S.I.) units of gray (1 Gy = 1 J/kg) (IAEA 2010).

1.2.2 Biological Properties

The biological effects are directly related to the DNA damage produced by the ionising effects in the target cell. This DNA damage can occur directly or indirectly, from either the ionisation or the excitation of the atoms belonging to the DNA, or from the products of the interaction of the radiation with the atoms and molecules other than the constituents of DNA.

The pattern in which radiation ionises the cell is described by the LET, and

particles with higher LET are associated with having greater energy deposition and therefore greater DNA damage. In comparison to X-ray, which is considered a low-LET radiation, ions will more often produce damage of the DNA structure within one cell which is more difficult to be repaired (Goodhead 1999). LET is a characteristic related to the radiation type that describes the energy deposited per unity of distance (normally expressed in $keV/\mu m$) and is commonly used to compare biological effects from different radiation types (Kraft et al. 1992; Zirkle 1954).

Relative Biological Effectiveness (RBE)

In order to quantify these effects and compare them with other radiation treatment modalities, the additional biological effect needs to be measured in a meaningful way such as a dose equivalent increment or factor. This is conceptualised as the relative biological effect (RBE), and in practice the RBE-weighted dose, used clinically for patient treatments, is the product of the absorbed dose and RBE. RBE compares the biological effect observed with a radiation type to a reference radiation in order to produce the same biological effect (Equation 1.3). Figure 1.2 shows the survival curves for the RAT-1 (dunning rat prostate cancer cells) cell line for both X-rays and carbon ions and the calculated RBE_{10}, which represents the ratio of dose between the different radiation types required to achieve the same cell survival of 10% (Tinganelli et al. 2013).

To compare the effectiveness of different ionising particles, the RBE has been defined. It is the ratio between the dose absorbed from the γ decay of ^{60}Co needed to produce the wanted outcome and the dose of the radiation under study (IAEA 2000), needed to produce the same consequence:

$$RBE = \left(\frac{D_{(\gamma^{60}\mathrm{Co})}}{D_{(\mathrm{test})}} \right)_{\mathrm{isoeffect}} . \tag{1.3}$$

RBE is a combination of a physical effect, namely the ionisation density, and of a biological phenomenon, that is the DNA repair capacity of the cell. In

general, RBE increases with the increase of the radiation LET up to a value of around 100 $keV/\mu m$ and above this value starts to decline due to energy deposition in excess of that needed to cause the biological effect (overkill) as seen in Figure 1.3. Energy loss events are essentially randomly distributed along the track of the photon or charged particle. For low LET radiations the energy deposition events along the track are sparse relative to the dimensions of biomolecules such as DNA with the result that photons may pass through such a molecule without depositing any energy. For high LET radiation the energy loss events are much more closely spaced and significant energy similar in dimension to biomolecules will be deposited along all parts of the track (IAEA 2010).

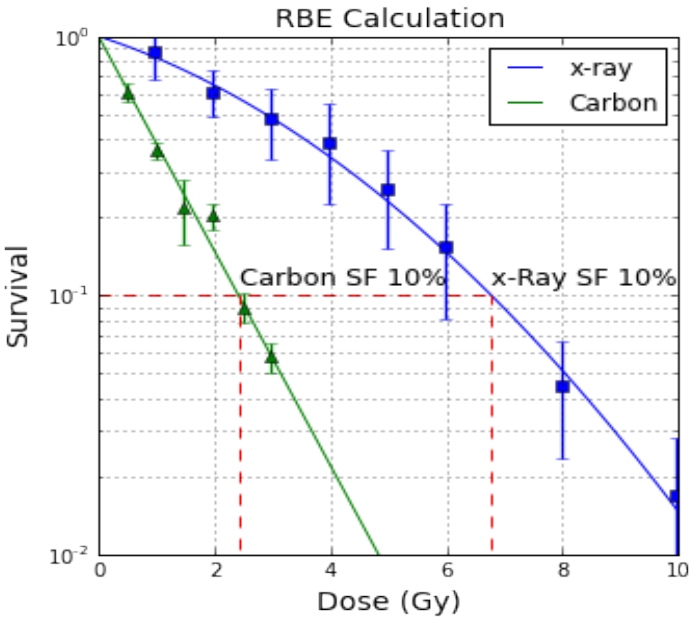

Figure 1.2. Cell survival curves for RAT-1 rat prostate cancer cells irradiated with carbon ions and X-rays (LET 150 $keV/\mu m$ for carbon ion beam and X-rays from an Isovolt DS1 X-Ray machine at 250 kVp and 16mA). Data from Tinganelli et al. with kind permission (Tinganelli et al. 2013). The horizontal lines follow the 10% isoeffect level and the vertical line follow the dose required for this isoeffect. The RBE_{10} is the ratio of these doses. In this case the RBE_{10} is the ratio of the dose 6.77 by 2.41 resulting in a RBE_{10} of 2.81.

RBE is used in the treatment planning process (the biological dose given to the patient is the dose of reference radiation divided by RBE for the particle

used in the treatment), so over-estimation of RBE could result in reduced tumour control since the physical dose given to a patient is over-reduced. Similarly, under-estimation of RBE in normal tissues could cause excess side effects. In the experimental determination of RBE, the natural variations associated with living organisms must be separated from the uncertainties introduced by the experimental set-up and its own detailed dosimetry. These factors introduce limitations in reproducibility and are responsible for the large reported variations in biological effects (Figure 1.3 - Sørensen et al. 2011 reviewed the reported RBE for different cell lines. In this figure the Chinese Hamster Lung V-79 cell line was replotted as an example because of the high number of available data). Desrosiers et al. (Desrosiers et al. 2013) associated this lack of understanding with the unavailability (or poor availability) of accurate dosimetry.

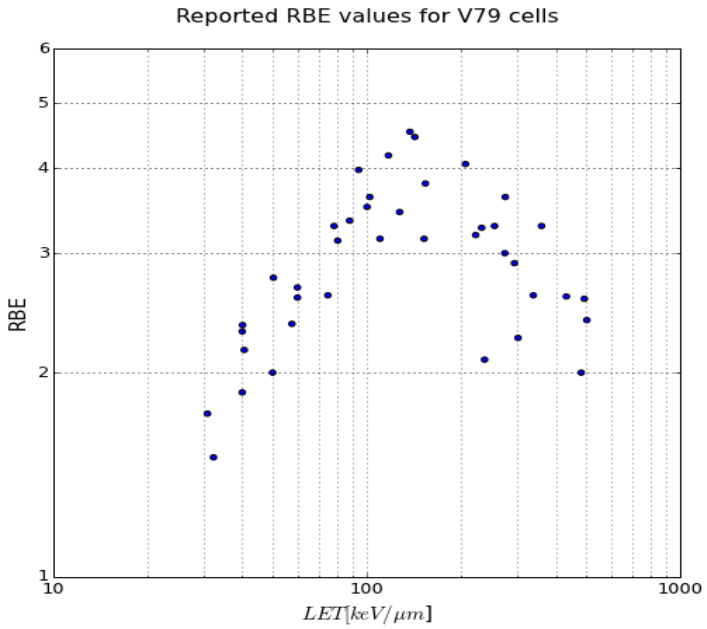

Figure 1.3. Plot of reported (Sørensen et al. 2011) RBE values for Chinese hamster lung fibroblast V-79 cells irradiated with carbon ion beams. The variations seen are probably due to biological variability and dosimetry uncertainties. Data reproduced from Sorensen et al. with kind permission.

1.3 Introduction to Radiobiology

1.3.1 Radiation Interaction with Cells

The main result of the interaction of ionising radiation with atoms and molecules is the production of free radicals which is generated due to the energy absorption and breakage of chemical bonds. These free radicals are responsible for some of the radiation effects on biological tissues and organisms. In addition to being highly reactive, these radicals are found in a number of biological processes, metabolism, oxidation, reduction, and pathological diseases and cancer induction (IAEA 2010).

Radiation causes a wide range of DNA lesions (Figure 1.4) such as:

- Single strand breaks in the phosphodiester linkage;
- Double strand breaks on opposing sites or displaced;
- Base damage;
- Protein-DNA crosslinks and protein-protein crosslinks involving nuclear proteins such as histones and non-histone proteins.

Although the number of DNA lesions generated by irradiation is large, thanks to repair mechanisms only a smaller fraction of these lesions give rise to cell inactivation/kill. Of the different types of cell damage, double strand breaks (or DSB) have been recognised as important for cell killing and in regard to the ability of cells to repair such lesions. Evidence has increasingly shown the importance of complex DSB lesions after high LET irradiation (IAEA 2010; Kraft et al. 1992; Zirkle 1954).

Cell death is achieved once cells lose their ability to divide and duplicate following radiation. This loss of reproductivity can occur by (discussed by Lauber et al. 2012 and described in Figure 1.5):

- **Apoptosis -** Apoptosis is one type of programmed cell death. It is commonly considered to be the prevalent form of cell death underlying

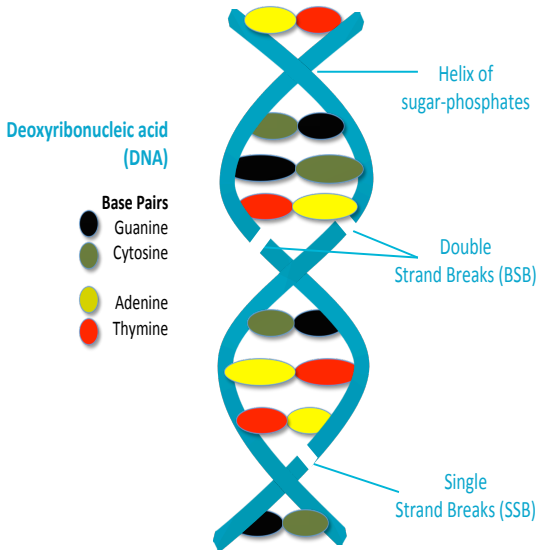

Figure 1.4. Different types of DNA damage by radiation.

daily tissue regeneration and renewal. Morphologically, it is characterized by cellular shrinkage, chromatin condensation, nuclear fragmentation, and membrane bleeding.

- **Necrosis or necroptosis -** In tumour cells of epithelial origin, which reveal limited apoptosis induction in response to radiotherapy, radiation-induced DNA damage has been reported to stimulate necroptosis. The crucial events in this context include the hyperactivation of the DNA repair enzyme and the subsequent and substantial depletion of intracellular ATP levels. Necroptosis is characterized by the production of reactive oxygen species, lipid peroxidation, swelling of organelles, rupture of the plasma membrane, and release of intracellular contents. Apart from necroptosis, ionizing radiation can trigger necrosis, an accidental, uncontrolled form of cell death as a consequence of excessive physico-chemical stress. Moreover, secondary necrosis can occur when apoptotically dying cells are not properly and timely engulfed by neighbouring cells or profes-

sional phagocytes, respectively. In both cases the integrity of the plasma membrane is lost and cellular contents, often in an oxidatively modified and partially degraded form, leak into the surrounding tissue.

- **Mitotic catastrophe -** Mitotic catastrophe is a form of cell stress, which occurs in the context of as a result of aberrant mitosis owing to uncoordinated or improper entry into mitosis. It has been assigned to be the major death mechanism in response to irradiation-induced DNA damage of cells with defects in cell cycle checkpoints and impaired DNA repair mechanisms.

- **Induced senescence -** Radiation-induced senescence is a condition of permanent cell cycle arrest, which can be observed in cells, where DNA damage is excessive and cell cycle checkpoints are still intact.

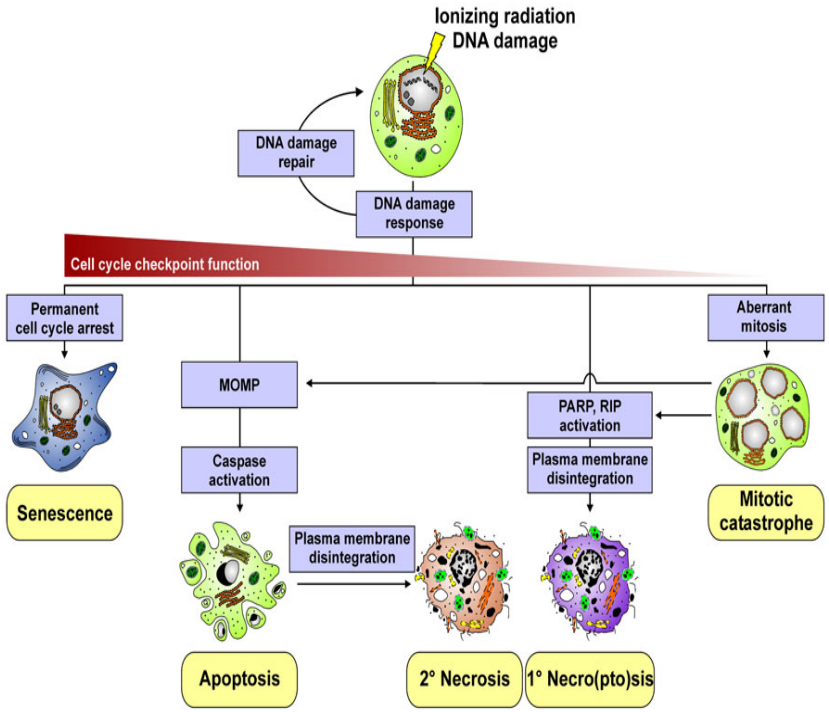

Figure 1.5. Different cell death modalities induced by ionizing radiation. (Lauber et al. 2012)

Apart from the induced senescence, all the cell deaths described above result in physical loss of the cell. Despite that, the result of these processes are not

immediate and require different cell divisions before they occur, e.g. mitotic catastrophe may not happen until several divisions have taken place (IAEA 2010).

Radiobiological Models In order to evaluate the different responses (or sensitivities) of cell types, the accepted gold standard is the evaluation of the cell's retention of its reproductive integrity or mitotic intactness, i.e. its ability of a cell to undergo cell divisions and produce a viable colony (IAEA 2010).

Survival curves are best shown as a semilog plot of survival against irradiation dose and the most common model used in order to represent this cell survival is the linear-quadratic model (LQM). The rationale for such quantitative method is the need to predict dose-response relationships. This is specially important when predicting isoeffect relationships for alternate treatments. In contrast to earlier methodologies, which were essentially empirical descriptions of past clinical data, the LQM formalism has become the preferred tool largely because it describes a mechanistically based model, with tumour control and normal-tissue complications attributed specifically to cell killing. The rationale here is that a formalism with a mechanistic underpinning is less likely to be subject to catastrophic failure, as had occasionally happened with empirically based models (Brenner et al. 1998).

The LQM assumes that lethal radiation damage is created either by a consequence of a single ionisation event or as a consequence of two, separated, sub-lethal event which combined create a lethal damage (Dale 2004). These different types of lethal damages are represented in Figure 1.6 below.

LQM is obtained by fitting a second-order polynomial, with the constants α and β describing the decline of survival (S) with increasing dose (D) (as seen in Equation 1.4 below). An example of cell survival curve was shown in Figure 1.2, where cell survival curves for the RAT-1 rat prostate cancer cells were irradiated with different doses and radiation types (in this example X-rays and carbon ions).

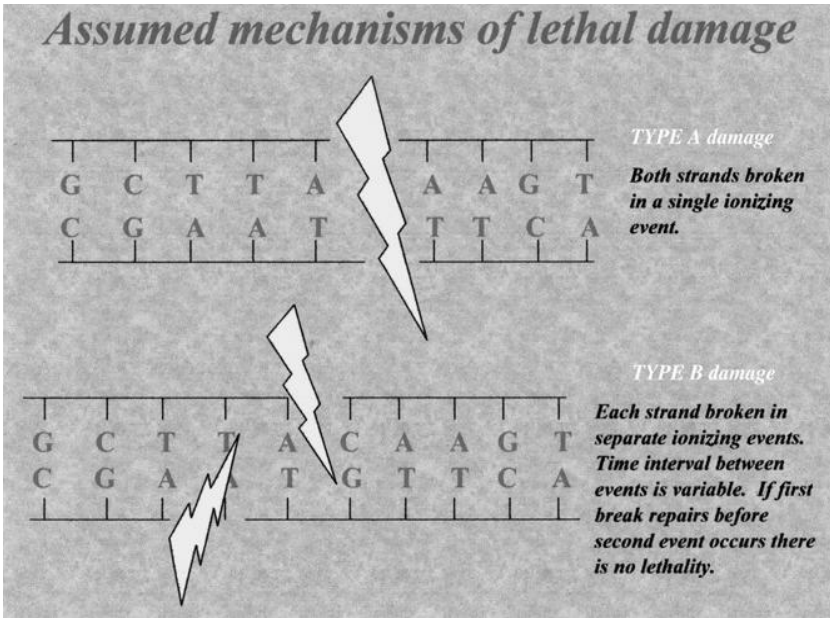

Figure 1.6. Schematic showing the formation of radiation damage as a result of double-strand breaks (DSBs) in the DNA. The DSBs may be created in a single ionizing event (Type A damage) or by complementary interaction between two separate ionising events (Type B damage). In each case, the base sequence on both strands is disrupted and cell lethality results. With Type B lethality, it is necessary for the second ionizing event to occur before the first has had time to repair itself. It is also necessary for the two events to be located within a few base pairs of each other (Dale 2004).

$$S = exp[-(\alpha D + \beta D^2)] \tag{1.4}$$

The α and β are regarded as the radiosensitive parameters of certain cell line. The LQM assumes that there are two components to cell killing, where the linear parameter (α) is correlated to the number of DSB associated to a single event and the quadratic parameter (β) to DSB originated from two separate events.

1.3.2 Repair of Radiation-induced Damages

Most DNA damages are repaired and just some rare lesions fail to do so. Specialised repair systems are capable to detect and repair damage to:

- Bases - base excision repair (BER)

- SSB - single-strand break repair (SSBR), closely related to BER
- DSB - homologous recombination (HR) and non-homologous end-joining (NHEJ)

DSB are considered to be the most lethal of the different damages induced by radiation. If not repaired, or wrongly repaired, DSBs can lead to loss of chromosomal material, cell death, mutations and chromosomal rearrangements (Kogel and Joiner 2010; McKinnon 2009). Figure 1.7 describes the different repair mechanisms.

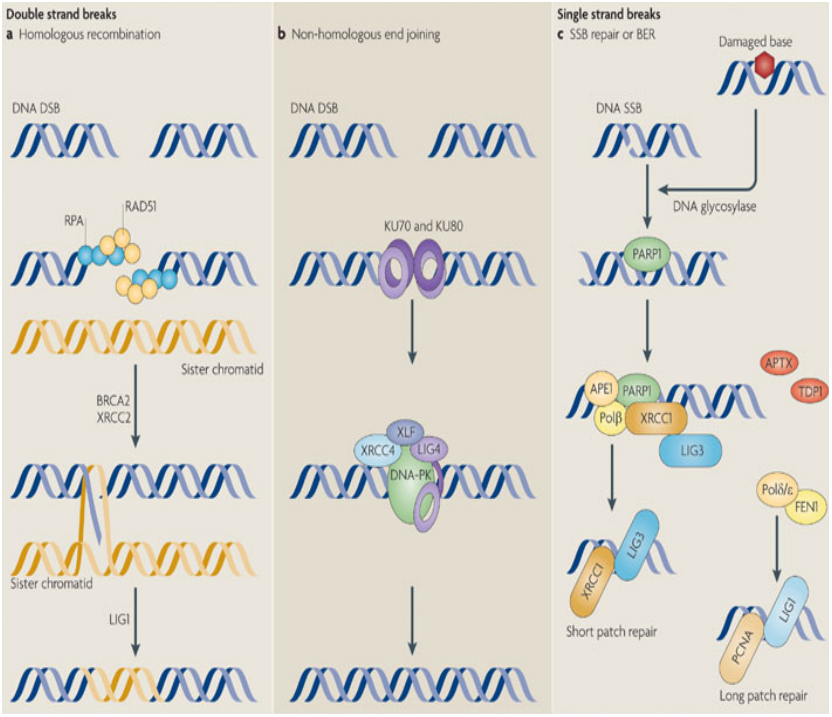

Figure 1.7. Different DNA repair mechanisms. (McKinnon 2009)

Homologous recombination (HR) As suggested by the name, HR uses homologous undamaged DNA (that with an identical sequence) as the template to repair the DNA with the DSBs in it. By using DNA with the same sequence as a basis for repair, the process is error free (Kogel and Joiner 2010; McKinnon 2009).

Non-homologous end-joining (NHEJ) NHEJ joins two DNA DSB ends together without requiring homologous DNA sequences. This is a faster process than in comparison to HR but it comes at the cost of accuracy, including small deletions or insertions often resulting at the repaired break site. Although this can lead to mutations, it allows the cell to survive (Kogel and Joiner 2010; McKinnon 2009).

Other repair mechanisms As previously discussed even though DSBs are associated as being the most lethal lesion induced they are not the most common. Base damage and SSBs far outweigh DSBs in number, being up to 50 times more frequent (Kogel and Joiner 2010; McKinnon 2009).

Since base damage and SSBs can also occur without irradiation due to normal metabolism, their repair pathways (BER and SSBR) have evolved and are capable of repair much more efficiently and preserve the genome integrity. In BER, most of the damaged bases in the DNA will be detected and removed by specialised proteins. These proteins, in addition to enzymes, will cut out the damaged bases leaving a nick, or SSB. Subsequent repair involves replacing the damaged base only or using a long patch repair where up to 10 nucleotides are cut out and replaced. Repair of SSB is similar, but since the damages were induced by radiation, there is an extra end-processing step to prepare the connection ends, mainly through the use of an enzyme. Short (base only) or long patch repair can then follow, in the same manner as BER (Kogel and Joiner 2010; McKinnon 2009).

1.4 Discussion and Conclusion

A major challenge in Hadron Therapy is to accurately predict RBE for clinical scenarios, and to determine which are the best mathematical models to correlate LET and dose with RBE (Fossati et al. 2012). A contradiction compared to photon (or conventional) radiotherapy is that currently a 2% tolerance in dose variation is used as a quality assurance limit for accurate delivery of the dose

(Miller et al. 2013), but the radiobiological uncertainties with protons and carbon ions exceeds this value. Currently uncertainties on RBE are in the order of 10-20% (Karger et al. 2010) with RBE varying clinically between 1.5-3.4 for carbon (Tsujii and Kamada 2012).

For protons, the prescription method is currently simplified by the use of a generic RBE value of 1.1 (Paganetti et al. 2002). Although experimental in vitro and some more limited in vivo data have been used to obtain this RBE value (RBE from 0.6 to 1.5 with average between 1.1 and 1.2), some concerns exist about the data sets and dose ranges used, with reports of more side effects than expected (Jones and Errington 2000). This results in large variations in the delivered biological dose in the target volume. These variations have the potential for increased risk of normal tissue damage (Tsujii and Kamada 2012). The large RBE variability has been reported as possible reason to why despite the improved conformity no reduction of adverse events were observed for brain tumours (Combs et al. 2013). This can be explained by the increased biological effect over the last few millimetres of the particles' path, especially when within or close to a critical structure (Paganetti et al. 2002).

Carabe et al. 2013 investigated the use of the 1.1 factor in proton therapy versus a varying RBE. The authors discussed that, while this constant factor had been proven to be a good average representation across the SOBP, in order to achieve improved accuracy biological effects variations must be considered. The authors also mentioned that in order for patient treatments to use these biological RBE modelling, more reliable radiobiological data would be needed for different cancer cell types and normal tissues.

One of the main challenges of modelling RBE is limiting its approximations and therefore associated uncertainties. Boehlen et al. 2012 evaluated a clinically used model and its susceptibility to errors due to its uncertainties or precision in the parameters used. In their work, the Local Effect Model (LEM) was used and in a sensitivity study the variability of the parameters used by this model were evaluated. They suggested that by accounting for biological uncertainties in treatment plans the outcome of these therapy modalities could be improved.

Another possible limitation to modelling RBE is that since mathematical models are as good as the data the model is based on, and, as it will be discussed in the next chapters, the current available data may have introduced uncertainties. By developing new tools, these uncertainties could be avoided.

There is also a divergence of opinion between researchers and clinical institutions as to which are the most suitable biological approaches. This can be seen by the presence of a large number of proposed models (Jones 2015a; Kraemer and Scholz 2000; Lomax et al. 2004; Carabe et al. 2013; Fossati et al. 2012).

Lastly, it is difficult to detect clinically the misestimations of RBE and survival (Boehlen et al. 2012). Especially given that the treatment outcome (including toxicity evaluation) of such precise treatment techniques can not be single out to uncertainties in RBE without excluding other factors such as physical limitations.

Therefore, in order to achieve the best possible clinical outcomes after Hadron Therapy, a larger range of experiments using human cell lines, tissue explants and in vivo experiments at clinically relevant doses must be performed in order to account for the limitations of current radiobiological experiments. In addition, it is important to recognise current set-up limitations so that improvements can be made to RBE estimations. This thereby allows for better evaluations of treatment doses for tumour control and better protection of normal tissues from unintended over-dosage. This must be undertaken in conditions that simulate actual treatments with variations in depth of targets, LET and dose ranges etc. For example the evidence that proton RBE varies with depth has been previously suggested (Britten et al. 2013) but more evaluations are needed.

All proton and carbon ions irradiations in this thesis were performed using the active scanning method. Some of the uncertainties described in my work (read beam uniformity, irradiation length, etc) could have been avoided or reduced by using the passive scanning method. However this method was not used since it is not widely available in new treatment facilities which mainly

rely on active beam scanning method. Furthermore, the variation in dose rates between different irradiation methods in respect to biological response (passive scanning 1Gy/second and active scanning up to 10^3Gy/second) was not thought to be relevant, particularly since, even at higher dose rates (laser driven accelerators - 10^9Gy/second), comparable biological responses have been obtained (Bin et al. 2012) .

1.4.1 ENTERVISION

The work presented in this thesis was done as part of my fellowship in the ENTERVISION project. ENTERVISION was a Marie Curie Initial Training Network (Dosanjh et al. 2015) project that was established in response to the clinical need for further research into online imaging and improvements into clinical protocols.

I was part of the work-group focused on pre-clinical development and simulation of imaging strategies for image-guided hadrontherapy. As a subgroup, our main task was the development of clinical treatment protocols for cancer radiation therapy, which required high quality information on the biological effectiveness of radiation doses using a range of beam qualities. This is especially true in terms of hadrontherapy (Boehlen et al. 2012). Therefore, verification procedures and future clinical protocols, multiple cell irradiation experiments must be performed at different dose points using a range of generic and patient specific tumour cell lines so as to gain robust data, which would ultimately aid biological dose model developments. Consequently, the development of radiobiological tools was extremely important and would serve to quickly verify the biological effects of complex dose distributions in homeomorphic phantoms, along with measurements of physical dose.

Chapter 2

Literature Review of Radiobiological Approaches

2.1 Aim

Different approaches have been used in radiobiological experiments. This chapter will discuss the challenges presented by these approaches and evaluate how these different uncertainties affect the final result.

The aim of this chapter is to evaluate and understand the difficulties presented by the current approaches in radiobiological experiments and use this knowledge to design a more suitable tool. These learning outcomes will be the basis of a new phantom design that aims to reduce these uncertainties and improve the final reported result.

The capability of this design to improve current radiobiological experiments, will be evaluated in the following chapters in respect of its dosimetric precision (Chapter 4) and biological output (Chapter 5), without introducing extra uncertainties in the final results (Chapter 3). Finally, Chapter 6 summarises the results obtained from both capabilities of the phantom and draws conclusions on their impact on RBE and the biological dose which is needed for Hadron Therapy.

2.2 Introduction

Despite its relatively long history and accumulated experience, radiobiology is still considered to be very imprecise. A recent review (Desrosiers et al. 2013) identifies dosimetry, or the lack of it, as the main concern for the reliability of radiobiological experiments. This improvement in dosimetry is even more important in the field of HT where uncertainties associated with the physical and biological properties of the ion beam and modern delivery techniques are challenges for the delivery of the correct dose (Carabe et al. 2012; Paganetti 2012).

A review was performed in order to understand the previously described uncertainties for the different experimental approaches used in radiobiological ion beam experiments with respect to their characteristics. This allowed conclusions to be drawn regarding advantages and disadvantages of each approach. Once these conclusions had been drawn, the need for a new device for radiobiological experiments was evaluated. An optimal phantom would be able to reduce the different sources of uncertainties in order, and, by doing so, it would be able to achieve improved reproducibility. The ideal phantom would be able to host different detectors and would therefore be able to reduce uncertainties related to dose reporting and would provide improved dosimetry. It would also be able to reproduce clinical treatment settings in terms of dose and LET distributions with depth.

2.3 Methods

In this chapter, a literature review of existing phantoms and set-up conditions for radiobiological experiments and their statistical reporting was performed. It was observed that uncertainties are related to both dosimetry (physical output) and the statistics of the biological output. The review was divided into the verification of:

- *Dosimetry or physical output* which can explain the large error bars re-

lated to reported dose. At this point, the dose measurement accuracy, or estimation, was evaluated through the reported uncertainties associated with the chosen detector and detector positioning limitations. The limitations due to the positioning include some systematic errors due to user variability, which can be reduced by the introduction of fixed detector positions and room positioning tools, for example with the aid of alignment lasers. For consistency, it was established that whenever a detector was not used (or not reported) the uncertainty was associated with the maximum acceptable uncertainty of 6% (Jaekel et al. 2001b), when performing measurements in phantoms from calculated doses in more complicated dose configurations.

- *Biological output* which includes the statistical uncertainties as documented by the error bars associated with the reported cell survival. Most of the biological uncertainties are caused by variations in technical parameters (i.e. cell maintenance) when samples are processed in multiple batches (known as batch the effect (Leek et al. 2010)). These uncertainties can be minimised by improving the experimental design allowing for large amount of samples to be processed in the same way and at the same time. This remains a very challenging task especially when clinic-like irradiation settings are needed. The unique design of the novel phantom proposed here will help to reduce technical sources of variation for the preparation of samples and to obtain high quality experimental data.

Close attention was also paid to how to produce the best statistical interpretation of RBE from the combined dose and cell survival uncertainties.

2.4 Results

Within the literature, three approaches are used in the majority of radiobiology experiments:

- Cell Culture Flasks or Multiwell Plates. This technique consists of

placing either a cell culture flask or a multiwell plate perpendicular to the beam direction. In addition, the effects of the irradiation at different positions along the beam path can be assessed by using multiples of such items(Figure 2.1).

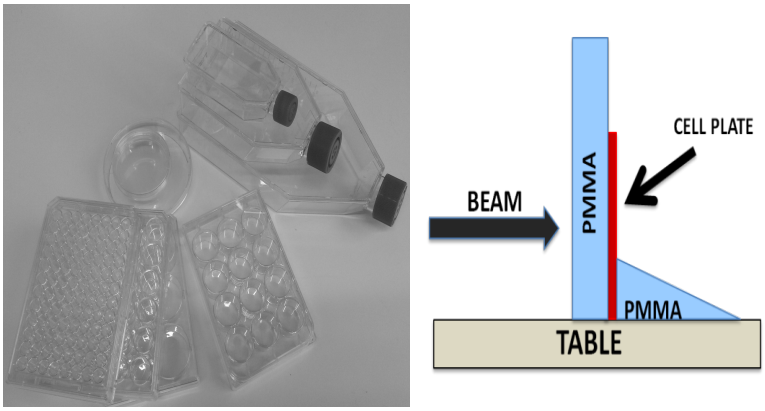

Figure 2.1. Left - The variety of cell culture plates and flasks that can be used in ion beam studies. The present phantom design uses the 12-wells plates. Right - The most commonly used experimental set-up for cell irradiation, which features a vertically mounted cell plate irradiated by a horizontal beam.

- Physical Phantoms Adapted to Biological Experiments. This technique involves tools that were initially created to assess beam parameters (i.e. absorbed dose, beam fluence, etc.), which can also accommodate cell flasks or plates (Figure 2.2).

- In-house Biological Phantoms. This technique encompasses different in-house solutions which best suit the patient treatment or specific scenarios (e.g. study of different oxygenation levels) (Figure 2.3).

The majority of radiobiological experiments (Barazzuol et al. 2012; Combs et al. 2012) use the first technique described above (cell culture flasks or multiwell plates). The advantage of this approach is its simplicity since most of the required tools are commercially available and are ready for use with very little preparation. In contrast, however, a few uncertainties may appear in the form of poor reliability and reproducibility effects, due to a lack of online beam information Desrosiers et al. 2013 discussed how to address these problems

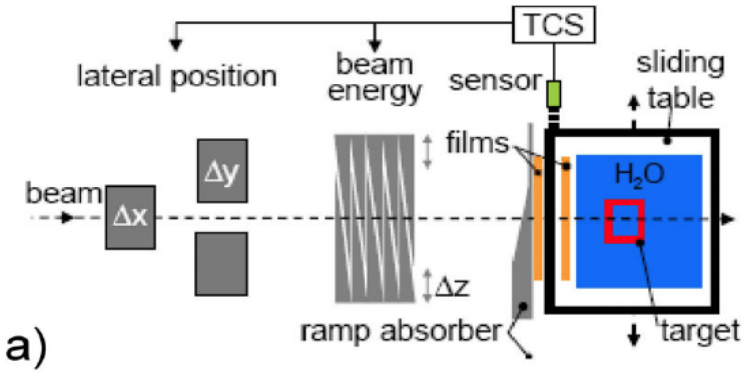

Figure 2.2. Examples of the second described set-up for ion beam experiments, with specifically designed dosimetry systems used for cellular irradiations. This figure shows the experimental approach used by Bert et al (Bert et al. 2010) with kind permission. In this set-up, the cell flasks are positioned in the marked red square in the figure labelled target.

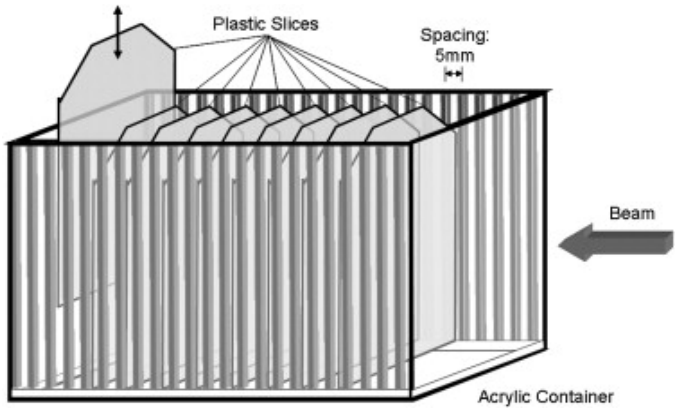

Figure 2.3. Example of the third described set-up, an in-house ion beam phantom used in radiobiological experiments. This Figure shows the experimental approach used by Elsaesser et al (Elsaesser et al. 2010) with kind permission. The cells are positioned in these in-house made plastic slices. One of the limitation of these set-ups is that re-sterilisation is required prior to further use of these plastic slices, which does not allow for multiple irradiations on the same day.

associated with poor dosimetric approaches, which undermine the reliability and reproducibility of available results in the literature. They found that these problems were associated with different techniques of measurement, reporting of radiation dosimetry, and setup conditions for radiobiology research. They also pointed out that dosimetry for research in radiobiology in published papers is frequently inadequately described, which suggests that the dosimetry itself may have been inadequate.

This can also be seen in the PIDE (Particle Irradiation Data Ensemble) database (Friedrich et al. 2013), which compiles the results obtained from several cell survival experiments with ion beam irradiation. In comparing these data to the α_{x-ray} and β_{x-ray} (x-ray linear quadratic model radiosensitivity parameters), variations were reported for Chinese hamster lung fibroblast V-79 cells ranging from 0.098 to 0.184 $[Gy^{-1}]$ for α_{x-ray} , which may reflect the poor reproducibility of this set-up. Some of these deviations can be explained by the fact that different V-79 cell lines contain variations in chromosome number and radiosensitivity. As discussed, these variations can be due to the unpredictable nature of working with living organisms, but there are also other systematic physical uncertainties at play. For example, limitations in positioning and dosimetry cannot be ruled out, but could have been avoided with a more robust system.

The second technique described above (Physical Phantoms Adapted to Biological Experiments) covers the use of what were originally physics-designed phantoms for quality assurance procedures (Bert et al. 2010; Arjomandy et al. 2010), which were adapted for radiobiology experiments. As an example of this approach, Bert et al. (Bert et al. 2010) (Figure 2.2) studied the effect of moving compensation techniques in cell survival. In contrast to the first approach, this technique allows for precise dosimetric assessment. Despite this, these approaches are generally more labour intensive in the preparation stages, which contributes to the difficulty in transportation and inter-centre comparisons (whenever both centres do not possess all tools). Another possible limitation is that not all physical phantoms can be adapted to host cell cultures.

The final technique described above (In-house Biological Phantoms) consists of the development of in-house solutions for radiobiology phantoms. The positive aspect of this approach is that it comes the closest to representing a patient treatment, as the beam distribution and cell conditions tend to reproduce different desired scenarios. General examples of this approach include the head phantom proposed by C. Gübitz et al (Guebitz et al. 2007, Sep 20.) and evaluated by Mitaroff et al. (Mitaroff et al. 1998) and the array of cell plates described by Elsaesser et al. (Elsaesser et al. 2010) (Figure 2.3 top and bottom, respectively). Another example is the work described by Tinganelli et al. (Tinganelli et al. 2013) where they were able to study the different dose responses at different oxygen concentrations.

On the designs used by Elsaesser et al. (Elsaesser et al. 2010) and Mitaroff et al. (Mitaroff et al. 1998), since multiple positions are available, and therefore multiple points along the beam are analysed, fewer irradiations would be necessary in order to understand how radiosensitivity changes at different LET and/or dose values. The orientation of the Mitaroff et al. (Mitaroff et al. 1998) phantom enabled the user to evaluate the effect of a mixed particle beam (containing both the primary beam particle and all other fragment particles produced from its interactions) in simulating the patient scenario. Another disadvantage of all these phantoms is the fact that all surfaces (the ones which enter in contact with the cell culture) must be sterilised prior to use which leads to increased preparation steps and a lower throughput of experiments per day, and could lead to increased uncertainties in the final biological results.

Therefore, as they have the ability to represent desired cellular conditions for studying the radiation effects in cell and tissue cultures, these phantoms introduce great complexity to experimental preparation and analysis. Moreover, not all of these phantoms are optimised for detector placement and evaluated for the disturbance in the cell compartments produced by these detectors.

By studying different commercial and in-house solutions available for dosimetric and/or biological phantoms it became clear that in order to achieve the required project goal, more than one type of phantom would be required

for improved dosimetry and biological readouts. The main characteristic we pursued for the phantom was the ability to have both physical and biological measurements in a device which is transportable and has lower complexity for usage and analysis of results. We also designed the phantom with the aim of performing multiple irradiations in the smallest amount of time in order to reduce for possible biological differences (Leek et al. 2010). In addition to its unique characteristics, the phantom design was inspired by some positive traits observed in previously reviewed phantoms.

In summary, Tables 2.1 and 2.2 compare the dosimetric and biological outputs for the reviewed set-up and describe the advantages and disadvantages of each technique, respectively.

From these observed uncertainties we were able to evaluate which effects these uncertainties have on the calculated RBE. The discussion of these can be found below.

2.4.1 Implications of the Observed Uncertainties

The observed uncertainties were divided into dosimetric ones due to the limitations of chosen detectors and statistical ones due to biological output. The implications of the different levels of these uncertainties were evaluated.

1. Dosimetric Uncertainties

   The dosimetric uncertainties were evaluated by observing the effect of the different reported dose uncertainties. This was done by obtaining different fitted curves at different levels of uncertainty. Using the data in Figure 1.2, I was able to estimate these effects by calculating the original fitted curves and their respective curves at different levels of uncertainty (1.0, 5.0 and 10.0%), which can be seen in Figure 2.4. With that data, I was able to evaluate the RBE variation. To estimate the survival curve variability (shown as shaded regions), we fitted the same functional form to the measurement points which were perturbed normally around the mean. The errors were treated as being of either a systematic nature (the

Table 2.1. Comparison between different commercial and in-house phantoms and their usability

	Physical Output (Uncertainties associated with dose measurement and positioning)	Biological Output (Uncertainties related to statistical limitations)
Criteria	*Relative Detector Uncertainty (for ions)*	*Number of dose response points*
Barazzuol et al. 2012	GafChromic films 4.6-5.1 % (Martišíková and Jäkel 2010)	Up to 96 laterally, and not limited to a certain number of in depth as stack is possible
Combs et al. 2012	Nothing or non reported 6.0 % (Molinelli et al. 2013)	Up to 96 laterally, and not limited to a certain number of in depth as stack is possible
Bert et al. 2010	Ion chambers 3.0 - 3.4% (Karger et al. 2010)	1
Mitaroff et al. 1998	TLDs 4% (Hoffmann et al. 1999)	587
Elsaesser et al. 2010	Nothing or non reported 6.0 % (Molinelli et al. 2013)	1 in xy 30 in depth
Proposed Phantom	Ion chambers 3.0 - 3.4% (Karger et al. 2010)	Up to 96 (8 laterally and 12 in depth)

error in the dose is likely due to a wrong dosimeter) or , of a statistical nature. For the systematic assumption, the maximum deviation was used and for the statistical variation these maximal errors were used, but, instead of using the same value for all dose points, uncertainties were applied randomly (with normal distribution) with the mean at the measurement and sampled 100,000 times.

The original RBE obtained at 10% survival (RBE_{10}) was 2.81, and when 1% of the reported dose was used the calculated RBE_{10} became 2.81 $\pm$ 0.05 (1 standard deviation). For 5% and 10% uncertainties, I obtained RBE_{10} values respectively of 2.81 $\pm$ 0.23 (8%) and 2.83 $\pm$ 0.46 (16%).

Table 2.2. Advantages and disadvantages of compared phantoms and proposed phantom.

	Advantages	Disadvantages
Cell Culture Flasks or Multiwell Plates (Barazzuol et al. 2012) (Combs et al. 2012)	Commercially available tools allowing for multiple irradiations	Dosimetric accuracy
Quality Assurance phantoms adapted to biological experiments (Bert et al. 2010) (Arjomandy et al. 2010)	Highest dosimetric precision	Low number of dose points increasing necessity for repetitions
In-house Biological Phantoms (Elsaesser et al. 2010) (Mitaroff et al. 1998)	Possibility of emulating patient irradiation conditions	In-house cell tools; increased sterilisation uncertainties and fewer possibility of re-irradiations
Proposed phantom	All of the above	Limited number of dose points owing to commercially available products

These results highlight the importance of reducing the levels of uncertainty related to the reported dose, including detectors and positioning. Figure 2.4 represents the obtained fitted curves at different levels of uncertainty.

2. Biological Uncertainties

The biological uncertainties, as mentioned above, were mainly statistical due to the limited number of sampled points. Moreover, there is no consensus on how to optimise the obtained results and correctly report their confidence interval. The statistics of cell survival fraction have been recently reviewed (Paganetti 2014) for protons. The statistical uncertainties associated with the survival fraction as well as the data fitting to provide the parameters α and β in the linear quadratic model are understood well, but there is little guidance in the literature regarding

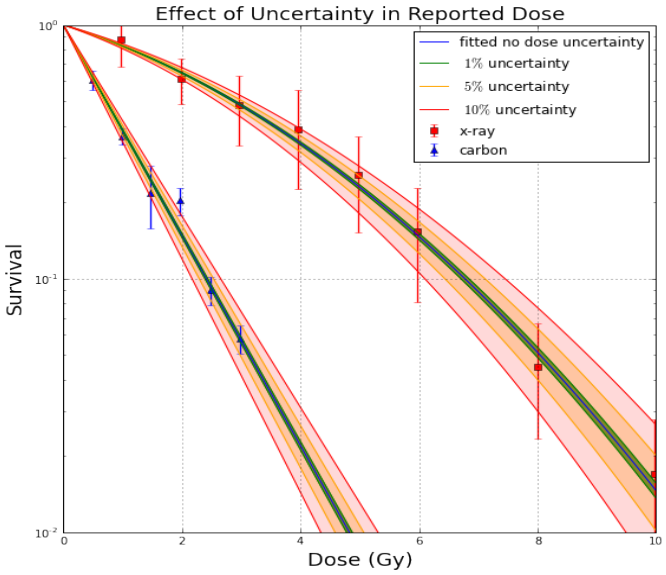

Figure 2.4. Evaluation of the effect of different levels of uncertainty in the reported dose on the fitted curves. The shaded area represents different levels of statistical uncertainties in the dose measurement. The uncertainty for the different detectors described in Table 2.1 are within these studied levels.

the calculation of RBE confidence limits. Based on Fieller's theorem, the proposal by Gupta et al. (Gupta et al. 1996) can be applied to RBE as described in the biological experiment chapter, in Section 5.3.5. This method allows for more precise calculations of RBE and its confidence limits, taking full advantage of the optimised biophysics of the phantom.

Current Radiobiological Uncertainties

I then evaluated this approach with the data presented by Tinganelli et al. (Tinganelli et al. 2013), since there are a limited number of papers that present current radiobiological uncertainties and their confidence limits. The original reported values were 0.136 ± 0.044 and 0.029 ± 0.004 for α and β $x - rays$, respectively. For carbon ions the reported curve was fitted with a linear fit instead of a linear quadratic. The reason for forcing the β to zero and using a linear fit instead of a linear quadratic is owed to the fact that at certain experimental data the obtained β factor can be negative if a linear quadratic curve is fitted. The reported α for the carbon ions was 0.936 ± 0.056 and the

RBE was 2.8 ± 0.2.

In Figure 2.5, the data from Figure 1.2 were re-plotted with the fitted curves ($y = exp(-\alpha x - \beta x^2)$) with these reported values and with maximum deviations (α + delta(α), β + delta(β), and α- delta(α), β- delta(β)). As mentioned above, as per the reported values, $y = exp(-x)$) was used for the carbon ions data. With these variations, the reported levels of uncertainties currently present in the literature can be seen.

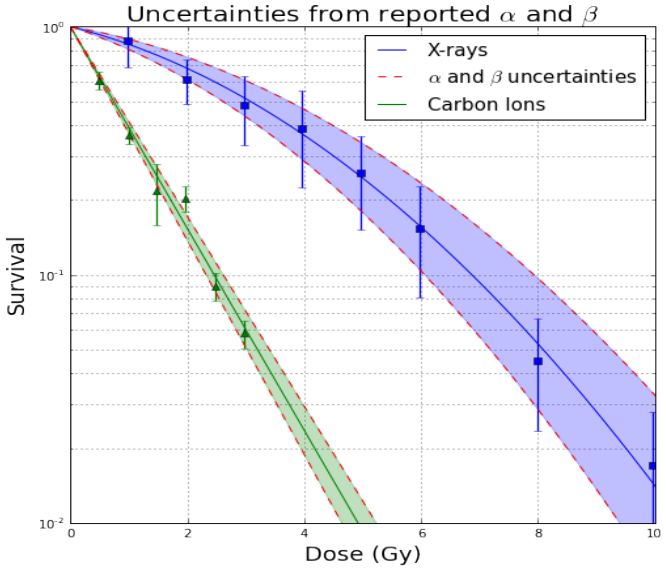

Figure 2.5. Plotted values from reported fitting parameters for RAT-1 rat prostate cancer cells irradiation with carbon and x-rays. The dotted lines have been used to represent the fitted curves with higher deviation and the shaded area represents the variations. The blue curve is for x-rays and the green one for carbon ions. Data from Tiganelli et al. (Tinganelli et al. 2013) used with kind permission.

Proposed Statistical Approach

As proposed by Gupta et al (Gupta et al. 1996), the uncertainties of a ratio of two quantities (C = A/B) can be expressed by Fiellerś Theorem:

$$\left\{C + \left(\frac{g}{1-g}\right) * C\right\} \pm \left(\frac{Z}{B*(1-g)}\right) * \sqrt{(C^2 * V_B) + V_A * (1-g)} \quad \text{where, } g = \left(\frac{Z}{B}^2 * V_B\right) \tag{2.1}$$

where V_B and V_A are the variances of B and A respectively and Z-score allow us to describe the confidence interval (CI) in terms of probability value. With this theorem I was able to derive the uncertainty of the final calculated RBE value (Equation 2.4) by calculating its confidence interval (Section 5.4.2).

The uncertainty of every measured survival at different dose points was calculated as described in Section 5.3.2. Then the survival curve could be obtained by fitting these to a linear quadratic equation, in order to describe the cell survival at different dose points. The RBE_{10} (Equation 1.3) is a ratio that relates the dose to obtain a isoeffect (in my case, the 10% survival) between a radiation test and a reference radiation and is easily obtained from the fitted curves.

The Maximum Likelihood Estimation (MLE) optimisation was used in order to obtain the optimised fitting curve. It works by maximising the agreement between the calculated survival points and fitted curve and thereby reducing the uncertainties associated with the values obtained from the fitted curve (Dorfman and Alf Jr 1969). The likelihood function is defined by (equation 2.2):

$$\mathcal{L}(\theta : x_1, ..., x_n) = \sum_{i=1}^{n} f\left(x_i|\theta\right) \tag{2.2}$$

Since optimisers in statistical packages typically minimise a function, it is possible to mathematically modify this equation. As the logarithm function is a monotonic function, optimising the logarithm of the function is the same as optimising the function itself. And using available optimisers (Science Python Statistic Library Minimise Function (Jones et al. 2001)) and minimising the

negative log-likelihood is equivalent to maximising the log-likelihood or the likelihood itself (Equation 2.3).

$$\begin{aligned} \mathcal{L}(\theta : x_1, ..., x_n) &= ln\mathcal{L}(\theta : x_1, ..., x_n) \\ ln\mathcal{L}(\theta : x_1, ..., x_n) &= -\sum_{i=1}^{n} ln\ f\left(x_i|\theta\right) \end{aligned} \tag{2.3}$$

Once the uncertainties associated with the fitted curves are known (in this example V_{x-ray} and V_{carbon}), the Equation 1.3, and therefore the 95% RBE Confidence Interval (CI_{RBE}), can be expressed in terms of the obtained parameters.

$$\begin{aligned} RBE_{10} &= \frac{D_{x-ray}}{D_{carbon}} \\ 95\%CI_{RBE} &= \left\{ RBE_{10} + \left(\frac{g}{1-g} \right) * RBE_{10} \right\} \\ &\pm \left(\frac{1.96}{D_{carbon} * (1-g)} \right) \\ &* \sqrt{(RBE_{10}^2 * V_{carbon}) + V_{x-ray} * (1-g)} \\ \text{where, } g &= \left(\frac{1.96}{D_{carbon}}^2 * V_{carbon} \right) \end{aligned} \tag{2.4}$$

This method was used in order to obtain the new optimised α and β parameters and RBE confidence interval. From these new parameters and their uncertainties (Table 2.3), Figure 2.5 was re-plotted as described above in order to evaluate the effect of different uncertainties on the survival curves.

Table 2.3. Before and after optimised fitting of radiobiological results.

Parameters		Reported	After optimisation
X-rays	α	0.136 ± 0.044	0.166 ± 0.021
	β	0.029 ± 0.004	0.026 ± 0.003
Carbon Ions	α	0.936 ± 0.056	0.954 ± 0.028

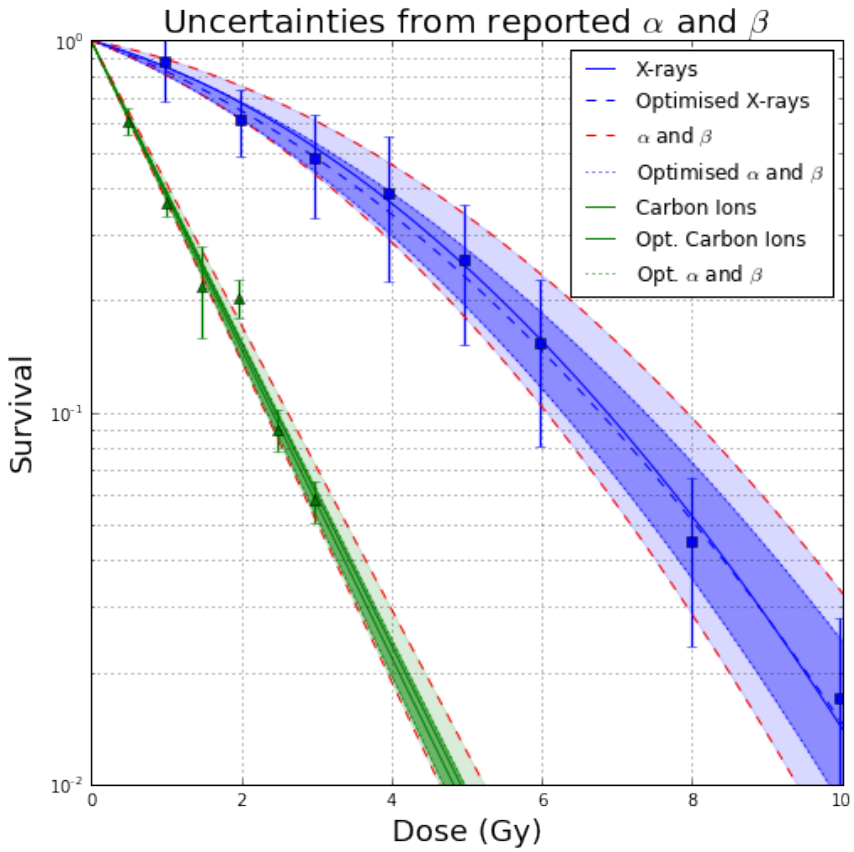

Figure 2.6. From these new optimised parameters and their uncertainties (Table 2.3), Figure 2.5 was re-plotted as described above in order to evaluate the effect of different uncertainties in the survival curves. The darker shaded area represents the optimised values and the lighter area represents the original values for fitted curves its variations. The blue curve is for x-rays and the green one for carbon ions. Data from Tiganelli et al. (Tinganelli et al. 2013) used with kind permission.

From the optimised fitted curves, the RBE_{10} value was calculated. Fiellerś theorem was applied and the RBE 95% confidence interval was calculated ($RBE_{10} = 2.76$ with 95% $CI_{RBE} = 2.53, 3.02$). The reduced uncertainty in the fitting, due to the optimisation, can be directly observed from the difference between the shaded areas in Figures 2.5 and 2.6. The variation of the RBE can be expressed in terms of the reduction of uncertainties of the fitting parameters. When the RBE was calculated for the obtained parameter uncertainties the RBE varied between 2.32 (-17.1%) to 3.42 (+21.7%) compared to the reported 2.81. With the optimised parameters the RBE obtained was 2.76 varying from 2.51 (-9.1%) to 3.11 (+12.6%). This demonstrates the possibility of reducing uncertainties in RBE estimation and reporting by using an optimisation method.

2.5 Evidence for a New Design

The new design, shown in Figure 2.7, is a dosimetry tool aimed at inter-facility comparisons, for verification of the delivered dose and radiobiological effects at different positions (and thereby also the beam quality) of a given plan. This particular phantom set-up would allow us to verify different radiobiological models that link LET to bio-effect in conditions where the dose is constant but LET is variable, as is the case in different positions along the SOBP. The phantom could also be used for beam profiling and treatment plan verification. The phantom offers two options: the first concentrates on the physical properties of the delivered beam and the second on delivering biological response information.

By using the described methods, multiple irradiations can be performed at the same beam time and on the same day. This will facilitate high-throughput data acquisition from biological samples prepared in the desired experimental setting. Also, with a formal statistical method accounting for the improved physical and biological estimations and an optimisation fitting method, a more accurate RBE and its confidence limits can be reported with reduced uncertainty.

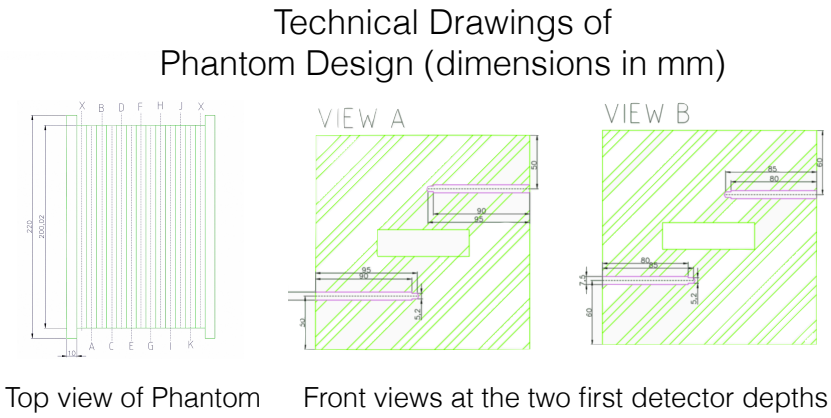

Figure 2.7. Technical drawings of the designed biological dosimetric Phantom. The different detector positions available and the cell holders can also be seen for the first two depths. In this design, the cell holder plates are then positioned along the beam axis covered by SOBP with the beam entry at the front of the phantom. All the reported dimensions are in mm.

2.5.1 Design

The proposed phantom, shown in Figure 2.7, consists of a PMMA block with dimensions of 240.0 ± 0.1 x 240.0 ± 0.1 x 146.0 ± 0.1 mm (in HWL), machined to accommodate a standard multi-well cell holder, for cell irradiations, and ionisation chamber pinpoint detectors at different positions. PMMA was chosen as it has similar properties to water (Yajima et al. 2009; Brusasco et al. 2000), to enable an easy dose to water conversion to be performed (see Material Selection Section 3.2.3). Dosimetric water equivalence is evaluated by uniformity of effective densities for relevant interactions and is essential to energy degrading of ion beams for range shifting, range compensation, and dosimetry (Kanematsu et al. 2013). An insert, from the same phantom material, was made for the commercial 12 multiwell plates used in this thesis in order to reduce uncertainties in the range calculation due to the air gaps present. Additional visual description of the phantom can be found in the Appendix A.

The design enables on-line information about the requested SOBP to be obtained from the available detector positions at the same time as cell cultures are irradiated. The phantom offers two options for experimental set-up:

- The first concentrating on a radiobiology experiment, which consists of a

laterally uniform dose distribution, enabling the user to obtain several irradiation points (the number of irradiation samples is limited by the type of multi-well cell holder used) for different depths without the need to repeat the irradiation; and

- The second concentrating on evaluating a complex dose distribution. This can provide a biological dose assessment with respect to lateral and depth distribution and the absorbed dose.

By measuring the dose deposition at the different known detector positions, an improved dosimetry at the cell holders location is obtained. Thus, by using a dose distribution calculation (for example by using Monte Carlo simulation as described in the coming chapter), it is possible to obtain the dose distribution in the different locations of the phantom, including the known detector positions. This makes it possible to verify the accuracy of the delivery plan, to benchmark the calculated dose distribution and a chosen resolution, and therefore to rely on the dose in different positions according to the obtained calculation.

2.5.2 Detectors

Radiation detectors are extremely important in all radiotherapy modalities, and hadrontherapy is no exception. Detectors permit the measurement of the absorbed dose, allowing control of the beam delivery and quality. Ionisation chambers were selected as the main detectors due to their widespread use in reference dosimetry by all major national and international bodies (IAEA 2000) and due to their common use as the main detectors in quality assurance procedures (Karger et al. 1999; Molinelli et al. 2013). Although ionisation chambers were chosen as the main detectors, alanine detectors and radiochromic films could also be considered appropriate for both dosimetric purposes and/or beam quality assessment (Herrmann et al. 2011; Spielberger et al. 2002). Table 2.1 describes the estimated uncertainties for different types of detectors used by radiobiological experiments, these uncertainties are associated with dose measurement and positioning. Table 2.4 provides an overview of the advantages

of the chosen detectors for this project. A complete table with several possible detectors can be found in the literature (Karger et al. 2010).

Table 2.4. Proposed detector types for this phantom including their advantages, disadvantages, and clinical applications. (Karger et al. 2010)

Detector Type	Advantage	Disadvantage	Application
Ionisation Chamber	High accuracy and reproducibility, small LET and energy dependence, easy to handle, many chamber types for different applications	Corrections for deviation from calibration conditions required, incomplete knowledge of corrections (chamber dependent)	Reference dosimetry, commissioning, dosimetric QA, dose verification, beam monitoring
Films	High spatial resolution, 2D measurement	LET and energy dependence, dose cannot be obtained from optical density in mixed fields, off-line analysis required	Measurement of lateral dose profiles, beam widths, field geometry and homogeneity, documentation of beam ports
Alanine	Nearly water-equivalent, linear response	LET and energy dependence, off-line evaluation with electron spin resonance	Point measurements

2.5.3 Criteria of Radiobiology Phantom

The ideal phantom is able to obtain dose response during cell irradiation, this allows for improved dosimetric accuracy and better correlation between biological response and irradiation profile.

The criteria for the phantom were:

- Dosimetric accuracy - which depends on the uncertainty associated to the detector type used. For this thesis, ionisation chambers were used, and as described in Table 2.1 their uncertainty is 3-4% (Karger et al. 2010). This choice was due to their low uncertainty for ion beam irradiations and their availability clinically. In Section 2.4.1-1, the effects of detectors uncertainties were evaluated for RBE estimation. Figure 2.4 demonstrates these detector uncertainties in the fitted curves.

- Biological uncertainties - which can be divided into the capability to perform multiple irradiations in order to produce the statistical variation, and the ability to correlate cell survival to the physical dose. For this thesis, the 12 multi well plate was used, but the phantom is capable of holding up to the 96 multi well plate (Table 2.1).

And by obtaining dose response during cell irradiation, it is possible to study cell survival by multivariate physical quantities (for example LET and Dose).

2.5.4 Justification of Criteria of Phantom Design

Section 2.4.1 discussed the implications of these dosimetric uncertainties in the final RBE estimation, where 5% and 10% uncertainties translated into 8% and 16% uncertainties in the RBE, respectively. As has been described (Section 1.4) most radiobiological experiments either use detectors which have uncertainties in this range or adopt dose calculation uncertainties within this range (Table 2.1).

The biological uncertainties, which translates into the clinical level of RBE uncertainty and therefore patient biological dose, also need to be taken into account particularly when they lay within the order of 10-15 % (for protons and higher for carbon ions) (Paganetti et al. 2002; Tsujii and Kamada 2012). This is one of the main negatives aspects associated to the hadrontherapy (Jaekel et al. 2013) as the treatment outcome is defined by the biological dose that is obtained by the multiplication of the RBE with the physical dose. Therefore

in order to maximise hadrontherapy treatment capabilities, efforts need to be made to keep these uncertainties to a minimum (Boehlen et al. 2012; Carabe et al. 2013; Carabe et al. 2012).

2.6 Conclusion

In order to improve our knowledge of enhanced radiobiological effectiveness, which is necessary to support clinical proton and ion beam applications, more dedicated tools need to be developed. In cases where observed disadvantages with some experimental set-ups (Table 2.1 and 2.2) can be reduced, a phantom with dosimetric information about the delivered beam would allow radiobiological experiments to gain the necessary reliability and reproducibility (Desrosiers et al. 2013). I have introduced a new design with the potential to reduce uncertainties in reported dose and biological effect associated with the experimental set-up. The phantom was designed to accommodate different types of detectors, which will reduce the uncertainties related to dose reporting (more than 50% if taking into account the reduction in uncertainties by using a more precise detector) and reproducibility. It also allows the investigations of the biological response and in relation to both dose and LET in the same manner as in clinical treatments. By using commercially available tools to host the cell cultures, the phantom permits several irradiations to be performed with the minimum introduction of biological deviations (same cell preparation, use of sterile tools, etc.). In addition, a statistical approach based on Fieller's Theorem was described in order to improve the confidence interval in reported RBE. It was shown that by the use of such techniques, a further reduction in RBE uncertainties is possible. The results from the phantom testing are described in the following chapters for the phantom's dosimetric and biological characteristics and its overall ability to reduce statistical uncertainties at different hospital facilities with different ion beams. The presented approach of a formal statistical method, which takes into account the improved physical and biological estimations, will provide a more accurate RBE and its confidence limits.

Chapter 3

Phantom Modelling and Design Evaluation in Monte Carlo Simulations

3.1 Aim

In the previous chapter, the evidence for a new phantom was presented, and from that a new design was introduced. The aim of this chapter is to study the implications of the chosen design and steps taken into account in order to reduce the possible uncertainties introduced and, by doing so, benchmark the computational tools developed.

The phantom aims to provide a radiobiological tool for studying biological dose delivery along with the ability to obtain improved dosimetric information from the delivered beam. This tool would be used to assess the biological response from different beam distribution configurations, allowing optimisation and biological verification of the treatment dose calculations and performance comparison of different Treatment Planning System (TPS) and Dose Delivery Systems (DDS) at different centres.

The work presented in this chapter was performed by using MC simulations. In order to verify the results and the accuracy obtained by those simulations,

benchmarking was performed with experimental data. Moreover, this study aims to understand the trends and uncertainties of the chosen phantom geometry and design with respect to improving its final dosimetric accuracy. The following sections present the methods employed to study these limitations, the expected performance based on MC simulations, and a discussion of potential effects of any found limitations on the results obtained in radiobiological experiments.

3.2 Introduction

The main areas of concern regarding the development of the phantom were the uncertainties associated with the radiobiological experiments including biological uncertainties and dosimetric accuracy (Section 2.5.3), and the uncertainties introduced by the chosen phantom design. After introducing the design, the main concern was to understand the effects of the chosen materials and detectors on the introduction of uncertainties.

Firstly, the range of uncertainties in the dose calculation due to the chosen phantom material was evaluated (Section 3.2.3). Subsequently the effect of the chosen detector positions was investigated. For this step, we evaluated whether the ionisation chambers placed at the chosen positions suffered from chamber-chamber effects (Section 3.4.3). We defined the chamber-chamber effect as the interference suffered by ionisation chambers, or any chosen detector, due to the interaction of the particle beam with the neighbouring ionisation chambers. This effect has previously been investigated (Parcerisa 2012) for carbon beams, but since protons are more susceptible to beam perturbation, for example beam widening due to scattering, I saw a need for further investigation. We also evaluated the effect of possible disturbance on the dose distribution in the central region where the cell culture to be studied was located, which would have been introduced by the inhomogeneities of the chosen detector (Section 3.4.3). All these evaluations were done with MC simulations.

3.2.1 Monte Carlo Simulations

MC simulations have been used for different applications in medical physics for several years (Rogers 2006). This use is even more intense in areas which are directly affected by radiotherapy dosimetry calculations, for example treatment planning dose calculations, dose verification for complex treatment techniques, radiation detector response calculations, image reconstruction and correction, and so on (Verhaegen and Seuntjens 2003). Although MC simulation is considered the gold standard in dose calculation, in the clinical environment it is not yet possible to benefit fully from this superiority since MC simulations are still considered too time consuming. Several approaches have been attempted to improve this, from the use of graphical processing units (or GPUs) (Giantsoudi et al. 2015) to the use of approximation steps (Fix et al. 2013), but for clinical scenarios, pencil beam algorithms, which are considered to offer a reasonable compromise between accuracy and computational speed for treatment planning, are still employed.

For HT, this is even more challenging as not the pencil beam algorithm needs to account for not only the primary, but also all the secondary products of the interaction of the primary beam particles and the medium. Kraemer et al. (Kraemer et al. 2000) proposed a pencil beam model for treatment planning which can be used to calculate the dose generated by a single heavy ion beam with E_{beam}:

$$D(E_{beam}, x)[\mathrm{Gy}] = (1.6\mathrm{x}10^{-8})\mathrm{d}(\mathrm{E_{beam}}, \mathrm{z})\left[\frac{\mathrm{MeV}}{\mathrm{g/cm^{-2}}}\right]\frac{\mathrm{N}}{2\pi\rho^2[\mathrm{mm}^2]}\exp(-\frac{1}{2}\frac{\mathrm{r}^2}{\rho^2}). \tag{3.1}$$

where r is the distance from the beam centre, ρ is the width of the Gaussian beam profile, and N is the total number of particles. Most importantly, $d(E_{beam,z})$ describes the energy loss as a function of penetration depth, z, taking into account contributions from all different particle species, T, with their given energy spectra, which are the products of projectile fragmentation.

$$d(E_{beam}, z) = \sum_T \int_E dE \frac{dN}{dE}(E_{beam}, z, T, E) \frac{dE}{\rho dx}(T, E) \tag{3.2}$$

As the applied beam model which calculates the deposited dose uses water or water-equivalent material as a reference, the concept of Water Equivalent Path Length (WEPL) was introduced in order to account for density variations on the beam path. Then the TPS is able to interpret the CT information and convert the obtained Hounsfield units (HU) into WEPL by the creation of a look-up table where high-density or low-density voxels are translated into a modified path factor that is shorter or longer, respectively, than the one used if water is present. So once a correlation between HU and WEPL has been created, a translation grid between the original CT voxels' positions and the WEPL corrected positions is created. The advantage of this approach is that it is possible to apply any models developed for water. Figure 3.1 shows the representation of this path modification and the experimental data used to create an example of a fitting to interpolate between different materials (Jaekel et al. 2001a), but as shown by He et al. 2012, this fitting is CT scanner specific and the use of a general approach can lead to deviations larger than 10 mm.

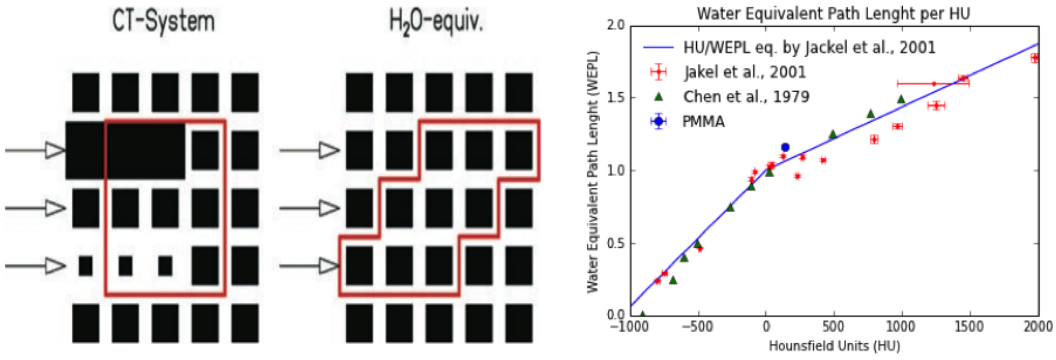

Figure 3.1. Left - Conversion between imaged information and WEPL. Right - And the proposed HU-to-WEPL conversion with the PMMA value marked.

These algorithms need some physical quantities that are computed with MC codes, such as the depth-dose distribution, beam widening and fragmentation production in water for different ions. For instance, MC simulations have been used to compute the input parameters of the TPS that is in clinical

use for both protons and carbon ions since the start of patient treatment in November 2009 in Heidelberg Ion Beam Therapy Center (HIT) (Parodi et al. 2012). Besides for beam characterisation of the TPS, MC simulations can be used to validate some dose calculations, especially in cases with great tissue heterogeneities (Mairani et al. 2013), to accurately analyse the dose delivered to patients and the calculation of biological effects (see Chapter 5). Additional areas of MC simulation applications for Hadron Therapy are support for risk-estimation for secondary cancer induction, radioprotection, and aiding developments for monitoring tools. For example, estimation of the production of $\beta+$ emitters, such as ^{11}C and ^{15}O, important for Positron Emission Tomography (PET) imaging and the production of prompt photons produced by the nuclear interactions (Boehlen et al. 2014).

FLUKA Monte Carlo Code

FLUktuierende KAskade or Fluctuating Cascade (FLUKA) is a multi-purpose MC transport code originally designed for high-energy physics but with extensive use in medical applications. FLUKA is intrinsically an analogue code, but it can be run in biased mode for a variety of deep penetration applications. For all MC simulations within this thesis FLUKA, (Boehlen et al. 2014; Ferrari et al. 2005) was the Monte Carlo code chosen for this project due to its demonstrated capabilities (physical and biological dose calculations, range verifications, setting up of different libraries necessary for the treatment plan commissioning, etc...) in HT (Mairani et al. 2010; Mairani et al. 2013; Parodi et al. 2012) and its powerful graphical tools (Vlachoudis 2009). All geometry simulation, updates and modifications were completed with the aid of FLAIR (a graphics user interface of FLUKA). There are currently two ways of describing the geometry within FLUKA: either by using a combinatorial boolean approach (Emmett 1975), and/or by the use of voxels, a possibility that allows detailed tridimensional representations and interconnection with medical imaging modalities like Computed Tomography (CT), PET and so on. This feature is particularly useful for dosimetry or treatment planning

purposes.

For the purpose of this thesis, the HADROTHErapy suite of physical settings (known as defaults) was selected. This suite handles the selection of the appropriate electromagnetic physics parameters (EMF package) related to the transport of electrons, positrons, and photons; inelastic factor corrections to Compton scattering and Compton profiles; particles transport threshold; multiple scattering threshold for both primary and secondary charged particles and δ-ray production.

For all hadrons except neutrons, the transport threshold, that is, the energy below which particles are deposited uniformly over the residual path, was set to 100 keV as suggested (cf. FLUKA manual). Neutrons are slowed down to thermal energies. To reduce computing time without compromising accurate energy deposition calculations, the electrons/positrons and photons transport thresholds, that is, the levels below which energy is deposited locally, were set to 30 keV and 3 keV, respectively. The effect of these different thresholds (delta-ray productions and transport, electromagnetic and neutron processes etc.) have been previously extensively evaluated and benchmarked for the selected geometries. The main part of the geometry description is the description of the beam line, and the part of the MC code representing both beam lines used have been evaluated and good agreement was obtained as such that the MC simulations aid on the treatment plan acceptance at both HIT and Centro Nazionale di Adroterapia Oncologica (CNAO) (Mairani et al. 2010; Mairani et al. 2013; Parodi et al. 2012).

Limitations of Monte Carlo Simulations

Monte Carlo simulation is the use of randomized numerical experiments to evaluate mathematical expressions. The main advantages are its simplicity since extensive knowledge is not required when using complete packages in order to obtain a solution. The MC simulations should be used with care due to several limiting factors. First, MC simulations values are only as good as the description of the geometry adopted in the simulations (Lima et al. 2016).

This also influences the estimation of error. The probabilistic error, which is essentially based on the variance, may not be a good measure of the simulation precision. This explains the need to benchmark against measurements. The second limitation relates to the required time to perform these simulations. MC simulations are slow as many samples are required in order to obtain acceptable precision. This is due to the fact that probabilistic error decreases as the reciprocal square root of the number of iterations.The third limitation concerns the uncertainty of the interaction modelling. On the whole, the physics is not exactly known, so MC can only be useful in making predictions if someone is using the code to actually look and compare the simulation of specific scenarios to data. These errors are systematic errors; they are separate from the variance and are not quantified by the variance. Systematic errors can only be evaluated from comparison with experiments and/or from knowledge of the uncertainties of each model.

3.2.2 Details about the Set-up of the Monte Carlo Simulation

In this section we will introduce the different terms and steps associated with FLUKA simulations used in this thesis.

The MC simulations are divided into two parts: beam description and irradiation target. Each of these parts needs to be validated individually. The beam description represents the description of the irradiation profiles (calculated by the TPS) and geometrical description of structures that may affect this irradiation profile until the target. The irradiation target, is the geometrical representation of the desired target to be irradiated. In this thesis the target is the phantom. The beam description depends on which facility the test has been conducted at.

Beam Description CNAO is a synchrotron accelerated hadrontherapy facility clinically delivering both protons and carbon beam treatments. A complete detailed description of CNAO facility current clinical capabilities are further

described in Section 4.3.3 (Rossi 2011; Molinelli et al. 2013). In order to correctly simulate the dose deposition, it is necessary to account for the different structures present in the beam path during the description of the geometry. These structures are the vacuum window, the monitor units and the ridge filter (only for the carbon irradiations). Below, Figure 3.2 and 3.3 show the schematics of the accelerator and treatment rooms, and the dose delivery system including the structures present. Figure 3.5 shows the same dose delivery system description in a three-dimensional model generated for the FLUKA simulations.

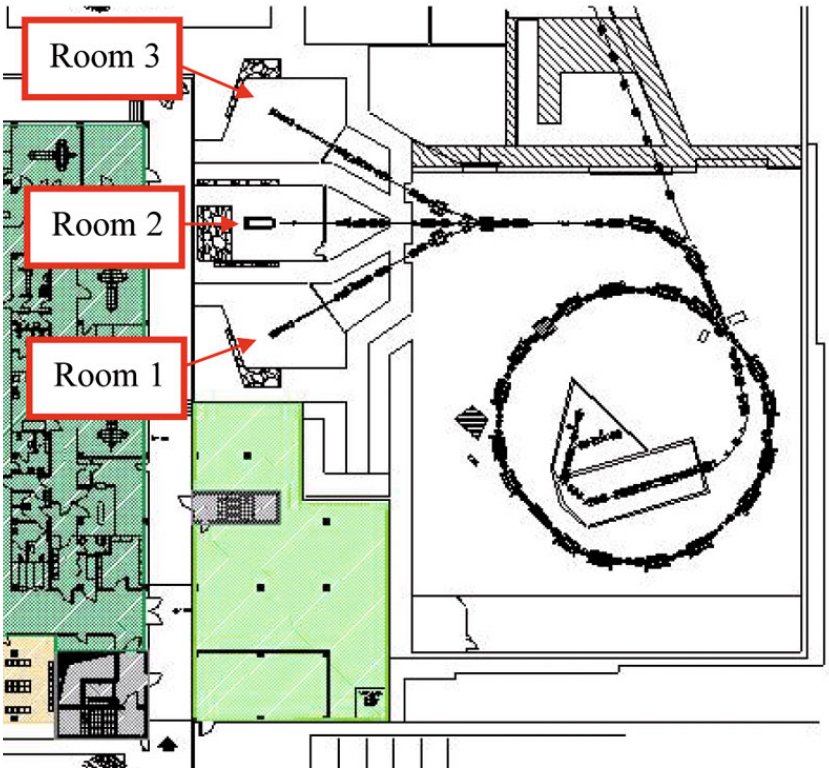

Figure 3.2. The CNAO accelerator design, including its pathway to the 3 treatment rooms are included in the schematics of the synchrotron design (Rossi 2011).

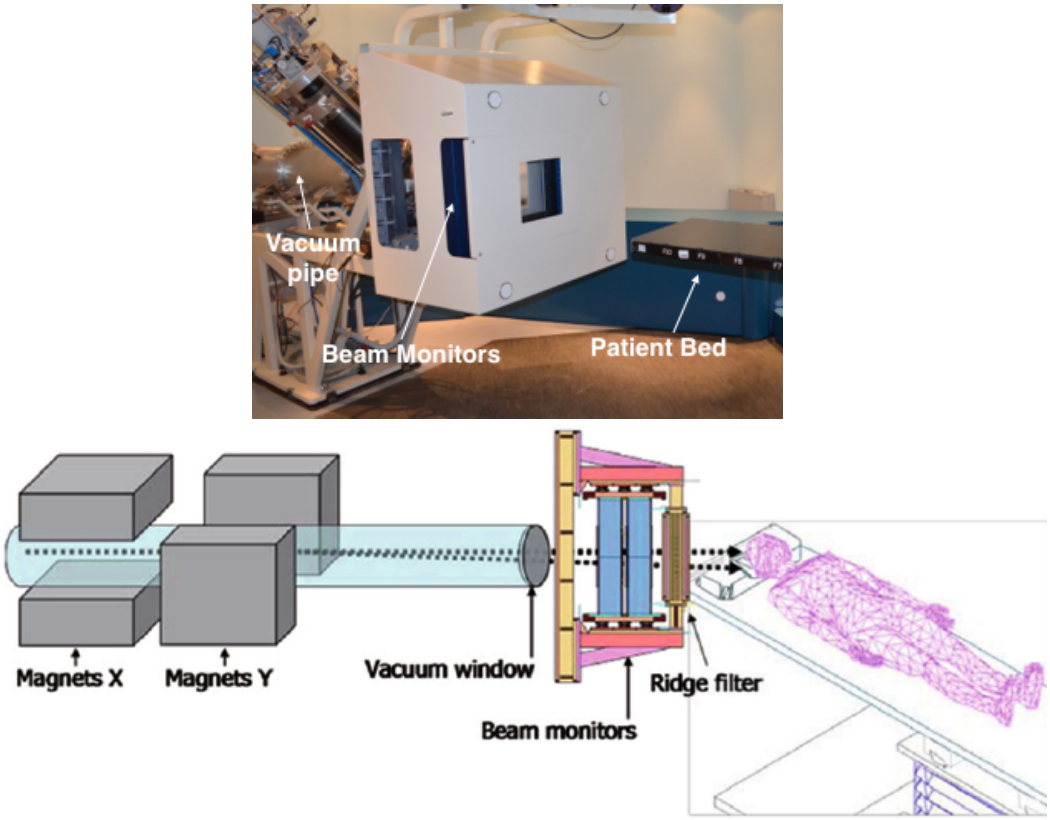

Figure 3.3. The CNAO delivery system can be seen in these figures showing a photograph of the system (top) and a model with description of its components (bottom) (Rossi 2011).

The validation of this DDS geometry generated with FLUKA has been described previously (Molinelli et al. 2013), but for the particularities of the work done in this thesis it needed to be re-evaluated. Initially, MC simulation were validated against experimental results (Figure 3.4), after which the calculated depth dose curves were implemented in the TPS database.

Physical parameters used in the TPS either derive directly from MC or were tested with the simulations. Therefore, the MC-based verification tool was identified as a benchmark for the evaluation of TPS analytical dose calculation accuracy. As discussed by the authors (Molinelli et al. 2013), the main difference between the MC and and the TPS is in respect to the lateral dose distribution modelling (Figure 3.4b). This is mainly due to the oversimplification of physical interaction processes applied in the TPS by the use of double Gaussian in comparison to detailing description of multiple scattering processes used in the

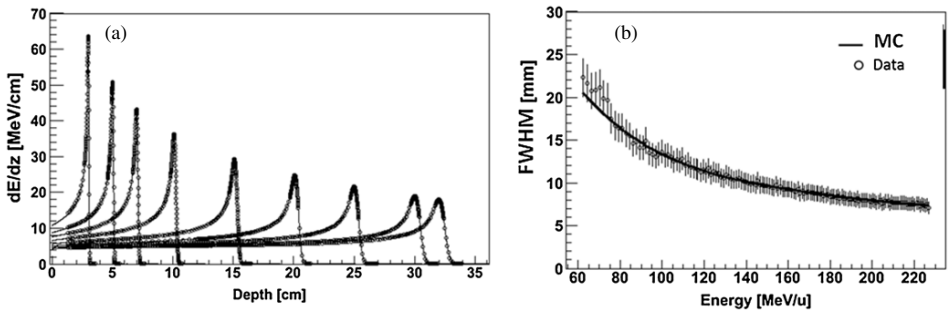

Figure 3.4. (a) MC calculated depth-dose-distributions for nine different beam energies in water (lines) are depicted together with experimental data (points). (b) MC calculated beam resolution at the isocenter of the beam line as a function of the proton beam energy. The solid lines refer to the calculated FWHM LIBC for the focus so far configured. The points with the error bars represent the experimental data. Figure obtained from authors with kind permission (Molinelli et al. 2013).

MC code.

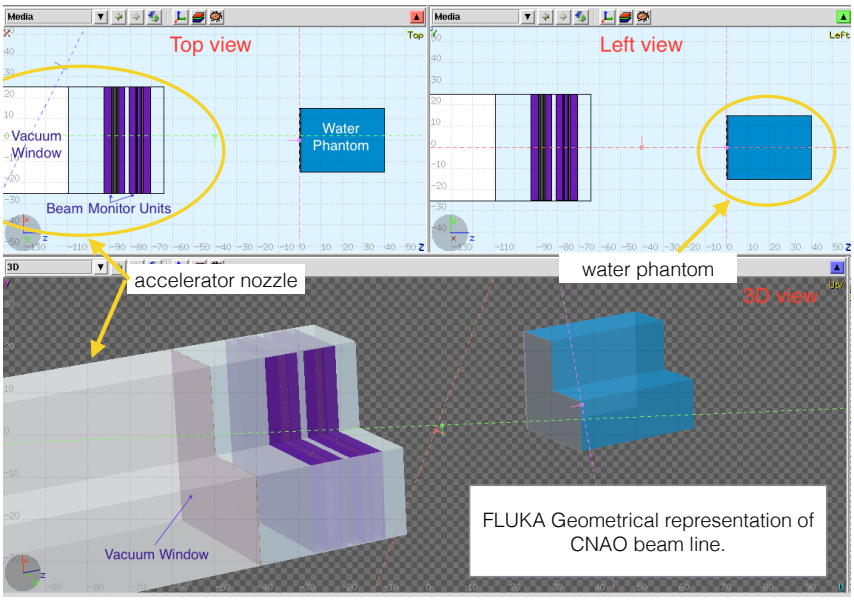

Figure 3.5. The generated FLUKA representation of the CNAO dose delivery system can be seen in this figure. The accelerator nozzle can be seen, which corresponds to the last structures in the DDS and also the water phantom used for quality assurance.

In addition to the DDS description, the FLUKA default user routine (which functions as a series of personalised computation scripts) was adapted in order

to be able to correctly interpret irradiation plan files into the simulations. In FLUKA , a built-in function called "source.f" must be used in order to obtain different irradiation descriptions (orientation, starting location and particle fluence). Users are able to personalise this function for their individual case. At a typical ion beam irradiation plan, the beam is divided into varying, multiple starting locations and particle numbers per location.

The modifications applied to the original source code can be found in Appendix B. The main changes was the interpretation of irradiation plan information into FLUKA variables:

- Location variables: $XFLK$, $YFLK$, $ZFLK$,
- Kinetics energy variable: $TKFLK$, and
- Number of particles to be simulated: *PARTICLESUM*.

The code was initially provided by the Medical Physics team from CNAO, but, due to the clinical use of CNAO simulations, the version of FLUKA and the one used in my simulations were different. In order to make the code work in my FLUKA version I had to update the links and imported variables present in this user routine. Furthermore, I had to correct the simulation reference to match the TPS orientation as the irradiation plan are generated in this reference orientation. At CNAO and other centres, this re-orientation is currently done during the post-processing stages.

3.2.3 Validation of Irradiation Target - Material selection

Polymethyl Methacrylate (PMMA) was the chosen material for the phantom due to its wide use in hadrontherapy (Yajima et al. 2009; Brusasco et al. 2000) and its composition comprising elements with low atomic numbers, homogeneity and cost compared to other water-equivalent materials (Kanematsu et al. 2013).

One possible issue when selecting the material for a phantom is understanding how this choice can affect the proposed experimental set-ups. As previously

stated, the phantom is to be used as a tool for complex dose distribution verification and radiobiological experiments. In both scenarios, the delivered dose distribution is obtained by analytical calculation from the TPS, and the presence of different material densities could impact on the dose distribution due to the introduction range of uncertainties during calculation (Paganetti 2012).

The main contributor to this uncertainty is the difference in stopping powers between materials and how the dose calculation software recognises these differences. Figure 3.6 below shows the difference in stopping powers between these materials. This plot was obtained from the tabulated values produced by SRIM (Ziegler et al. 2010).

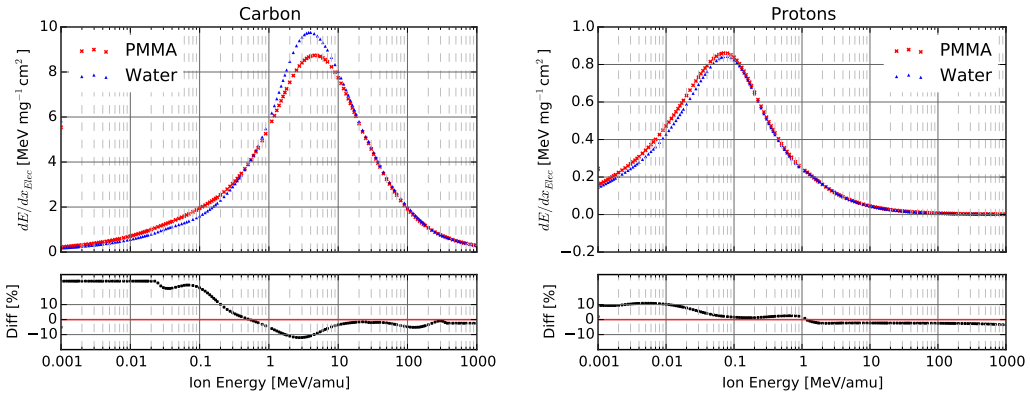

Figure 3.6. The plots at the top display the tabulated data for electronic stopping power at different energies for both water and PMMA and for carbon ions and protons respectively. The plots at the bottom represent the calculated deviation between the two materials. Data obtained from the tabulated values produced by SRIM (Ziegler et al. 2010).

Another possible limitation, as described by Jaekel et al. 2001a, is that although PMMA is measured, it is normally excluded from the clinical fittings for HU/WEPL conversion (compared with Figure 3.1) owing to its non-tissue equivalent composition. Thus, in order to correctly account for the dose distribution with the TPS, the WEPL of the PMMA had to be measured (Kraemer et al. 2000; He et al. 2012; Brusasco et al. 2000) and correctly applied in the dose calculation. In this section, I also evaluated the effect on the correct

material description in the MC simulation.

3.2.4 Influence of Detector Positions in Dose Measurements and Dose Distribution in the Cell Compartment

With respect to the detectors, the uncertainties associated with their dosimetric capabilities and their implication for the final radiobiological experiment results have been covered in the previous chapter, but the implications of the chosen positions for a possible beam disturbance due to the presence of non-homogeneities on the beam path need to be evaluated. The main assumption is that since the distance between each detector and between detector and cell compartment is not inferior to the distances used by current commercial dosimetrical tools, no disturbance will be detected.

While the aforementioned dosimetrical tool was initially design for carbon beams, proton beams are more susceptible to scattering, which could present a issue that has not been previously evaluated.

3.3 Methods

3.3.1 Validation of Phantom Modelling

The benchmarking of the MC simulations was divided into two steps. The first was the evaluation of the mean dose deviation between a uniform dose distribution and ionisation measurements, followed by the same evaluation with different non-uniform dose distributions. Once the beam description was validated, the second step was to evaluate the irradiation target by comparing the measured and calculated depth dose profiles and estimating the WEPL.

Validation of Beam Description

As part of the Quality Assurance (QA) tests in HT facilities, cubes of known dimensions are irradiated. In this thesis irradiation experiments were carried out following the evaluation of a uniformly distributed dose (in the shape of a cube) centred at 9 cm depth in water with dimensions of 6 x 6 x 6 cm. The experimentally obtained ionisation chamber measurements were compared with the calculated dose depositions from the TPS and MC.

For the purpose of benchmarking a non-uniform dose distribution, previously published data were re-analysed (Molinelli et al. 2013). In this, the authors investigated nine patient plans where the warning QA threshold (fixed at 3% mean dose deviation between measurements and TPS) was crossed. The data consisted of ionisation measurements, MC simulation and TPS dose deposition calculations.

The authors originally explored the possibility that these differences found were related to:

- Dose modelling (TPS vs MC),
- Limitations of the dose delivery system, or
- Incorrect positioning of detectors.

Other factors, such as the oversimplification of dose modelling were not ruled out. One reason for analysing their data was the availability of experimental measurements using, the CNAO dose delivering system for benchmarking my MC simulations. Moreover, they had used similar detector distances for their phantom in relation to my proposed phantom. Other reasons included the amount of availability of data (both experimental and dose calculations), and the fact that, instead of using the full 24 positions available in the ionisation-chamber holder (see Figure 3.7), they had only used 12. (see Section 3.3.2 for further details).

The current CNAO quality assurance procedure (Ciocca et al. 2012; Molinelli et al. 2013) specifies that a verification will be performed for each patient plan

(Karger et al. 1999). In order to do so, a water tank with a 3D detector block controlled by a motorised arm (PTW-Freiburg GmbH) is used. This allows the dose deposited at different known depths and positions to be measured. This detector block is a holder for the ionisation chambers (PTW pin point chamber which have a 0.03 cm^3 sensitive volume), in a such way that the ionisation chambers do not obstruct the direct path of the beam. According to the QA procedures, PTW-Freiburg GmbH pinpoint ionisation chambers were used. (Figure 3.7). The measurement values for each ionisation chamber is then compared with those values calculated by the TPS (Equation 4.2). For data set analysis, the mean deviation is calculated as the difference between the measured ($d_{meas,i}$) and the calculated dose ($d_{calc,i}$), normalized to the maximum beam dose (d_{max}) and averaged over N IC positions i:

$$\frac{1}{N}\sum_{i}^{N}\frac{|d_{meas,i}-d_{calc,i}|}{d_{max}}\% \tag{3.3}$$

The number of points N included in the calculation can be equal to or lower than 12, depending on the dataset. The TPS provides a 3D-averaged dose gradient for each IC position. Points with a calculated gradient higher than 0.04 $Gy\ mm^{-1}$ are excluded from the analysis, since they can not be measured accurately enough owing to the finite size of the detector sensitive volume and experimental set-up uncertainties. For QA measurements in reference conditions, as recommended by the International Commission on Radiological Units (ICRU), the applied acceptance threshold is 5% for both mean deviation and standard deviation over a data set. This approach is taken in order to guarantee that delivery of the dose to the planning target volume in the patient is within an uncertainty of less than 5% at the 2ρ level (ICRU Report 24 1976).

Current MC patient plan verifications, as per the TPS, use a simpler approach to geometrically represent the ionisation chambers when calculating the dose deposition. None of the detectors' structures and holders are included in the geometrical description, and the detector dose is sampled from the dose distribution in a water tank. By so doing, the structure and materials of the

ionisation chambers are not taken in consideration for the simulation. But differently from the TPS which uses only one voxel value, MC obtains the deposited dose in the chambers by calculating the average dose to water over several voxels, corresponding to the active volume of the detector, situated in the positions where the chambers would be located.

$$\sum_{i}^{N} \frac{\left(d_{calc,i} - d_{meas,i}\right)^2}{\Delta d_i} \tag{3.4}$$

where Δd_i is the 3D dose gradient in the IC position i over the N IC positions in the data set.

The aforementioned approach, with its geometric approximations and simplifications, was found to obtain the correct results for the majority of studied cases. But, for the example of the nine cases where the agreement between the MC simulations and measurements was found to be unsatisfactory, we decided to investigate the impact using detailed geometry in order to account for the dose disturbances, mainly from scattered particles produced in the wall of the ionisation chambers and detector holder.

In the new detailed geometry, all of the geometry described above is kept, including the PTW3D block and ionisation chamber description (with respect to all structures, dimensions, and material compositions). Detailed technical drawings were obtained from the manufacturer (PTW Freiburg). The FLAIR geometry editor was instrumental and extremely helpful in dealing with drawing and 3D visualisation (Figure 3.7). As for the original MC approach, the final deposited dose is the contribution of the different voxels present on the active volume of the detector (Equation 3.4).

For the purpose of this part of the work, the ionisation chamber measurements were compared with the MC simulation results for the current set-up with 12 chambers. These results were used to benchmark our simulations and we were then able to compare the effect of introducing the remaining 12 ionisation chambers (Section 3.4.1).

Validation of Irradiation Target

The depth-dose profile of a 270 MeV/u ^{12}C beam was measured with a water absorber. The tool used was the Peakfinder, by PTW-Freiburg GmbH, a water column system for peak detection in protons and ion therapy. It is a closed water column which is able to measure BP positions with a relative spatial resolution of 10μm up to 35 cm depth. It contains a built-in thin window ion chamber and it is read out by a electrometer. The software package included allows precise measurements and a detailed Bragg peak analysis. The measurement of the BP is made with and without the material in which the WEPL (Equation 3.5) needs to be calculated. In my case a PMMA slab from the phantom was placed along the beam path, with 20mm thickness.

$$WEPL_i = \frac{(r_{wo} - r_w)}{t_i} \tag{3.5}$$

where WEPL for a material i is obtained by the subtraction of the r_{wo}, range in water without the presence of the material, by the r_w , the new range with the introduction of the material in the beam path, divided by the thickness of the material, t_i. The range is the position of the measured bragg peak in water.

For the purpose of benchmarking our calculated WEPL results and simulations, the phantom was tested for both protons and carbon ions at CNAO and the effect of correctly accounting for the WEPL was analysed by comparing the different dose depositions.

Additionally, the material description used by FLUKA simulation is evaluated. During the simulation the material description was done by the "MATERIAL" and "COMPOUND" cards (as it is called in FLUKA). The different entries present in the initialisation file. As definition, these cards describe a single-element material or a compound. Steps were taken to evaluate whether the default description was able to correctly describe the dose deposition and range. For the PMMA material, the default description (composition, atomic number, etc.) was evaluated by estimating the effect of the default density of

1.20 g/cm^3 in the dose deposition.

3.3.2 Design Evaluation

Once the beam description had been validated the phantom design was evaluated.

Detector Positions - The Chamber-Chamber Effect

To study the chamber-chamber effect, the available data (ionisation dose measurement points) obtained with the phantom developed by GSI (Karger et al. 1999) and commercialised by PTW-Freiburg GmbH were used (Figure 3.7). The primary reason for this choice was that the distances adopted by our phantom design were similar to those used by this commercial phantom. Another reason for using this phantom was the amount of available experimental data, for both protons and carbon beams, as this is the phantom of choice in both hadrontherapy facilities using different ions in Europe (HIT and CNAO).

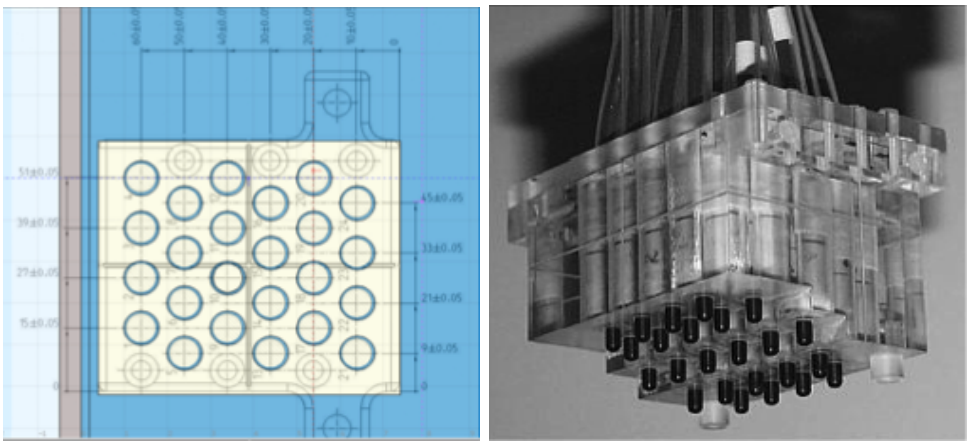

Figure 3.7. Graphic representation from MC simulation and real pin point ionisation holder array from PTW-Freiburg GmbH.

To study the chamber-chamber effect the same approach as was used to benchmark the simulation was selected. At CNAO, the measurements were made with half of the proposed number of the detectors (24), so data from MC simulations were compared with two different set-ups, one with all 24 ionisation

chambers versus the same set-up with 12. The difference between the two simulations was then evaluated. A comparison was subsequently made on the dose difference between these 12 (or 11) measurements per patient for a total of 10 patient treatment plans.

Dose Distribution Disturbance in the Cell Region

Once we had decided to proceed with the proposed design and the detector positions, the worst possible disturbance that the detectors could introduce to the dose distribution in the central region was studied.

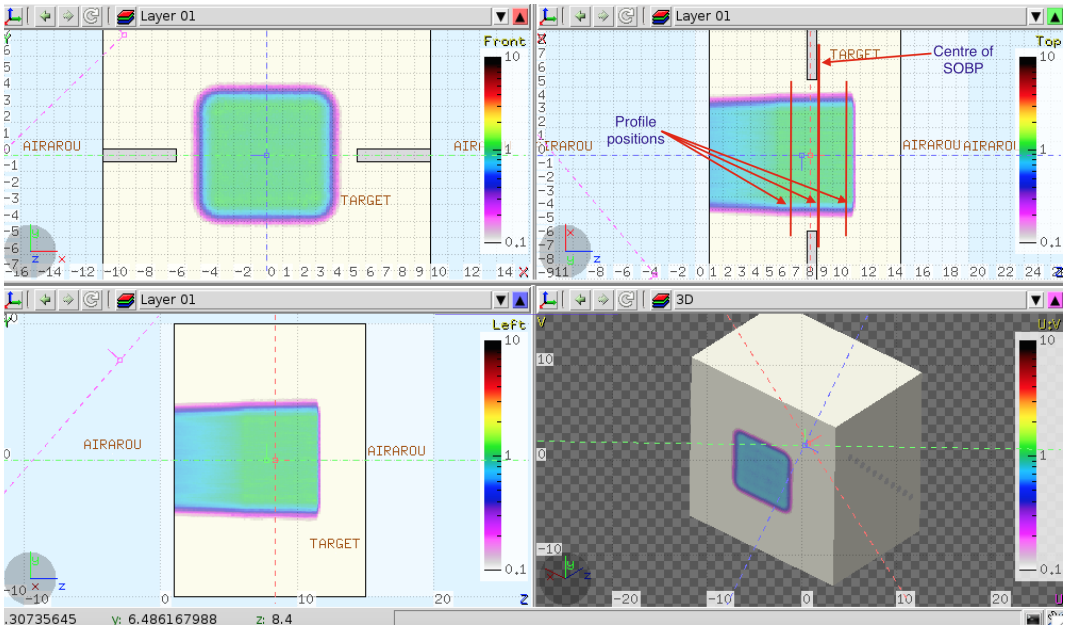

Figure 3.8. Graphic representation from MC simulation of the phantom and uniformity study for dose disturbance evaluation. It includes a frontal view (top left), from above (top right), lateral view (bottom left) and a 3 dimensional view, all of them showing the 1Gy uniform dose deposited in a cube centred at 9 cm depth with 6x6x6 cm dimensions. On the top right image can also be seen the location of the SOBP centre and position of the calculated profiles.

As previously discussed, the phantom is able to accommodate different types of detectors, so I decided to replace the ionisation chambers in our simulations by tungsten cylinders in order to increase the effect of beam disruption due to the presence of a high value Z and high density material in the beam path. All other specifications including materials and dimensions were kept the same. We

simulated a uniform SOBP centred at 9cm deep, corresponding to the centre of the phantom, with dimension of 6x6x6 cm as shown on Figure 3.8. From the recorded dose grid, profiles were taken perpendicular to the central axis at different depths (at the centre of the SOBP $\pm 2cm$) for simulation both with and without detectors. The doses differences were then calculated.

3.4 Results

3.4.1 Validation of Phantom Modelling

Benchmarking of Beam Description

Firstly, in order to benchmark our simulation, the MC simulations were compared with the measurements for a simpler irradiation geometry with less dependence on the detector positioning. As previously explained, the dose deposition obtained by a uniform cube was evaluated. Figure 3.9 below shows the isodoses calculated by the TPS and the calculated dose values at each ionisation chamber position.

Figure 3.10 shows the comparison between the measured values and simulated results and the obtained deviations. On the top plot, blue points represent the ionisation chamber measurements and associated errors (set at 3% as previously described), and red points represent the introduced simulation, with its obtained uncertainties. On the lower plot, I calculated the deviation between MC and measurements and the shaded area represents the error associated with the ionisation chambers.

A mean deviation of -0.142% was obtained with a maximum of 2.8%, minimum of -1.8% and standard deviation of 1.7%. This shows how much my simulation agrees with the measurement. These mean deviations and maximum deviations are within the detector uncertainties therefore it may be possible to accept the simulated geometry of the dose delivery system for the continuation of the thesis. Although before continuing, since these values are within the uncertainties of the MC simulation, it was necessary to further investigate the

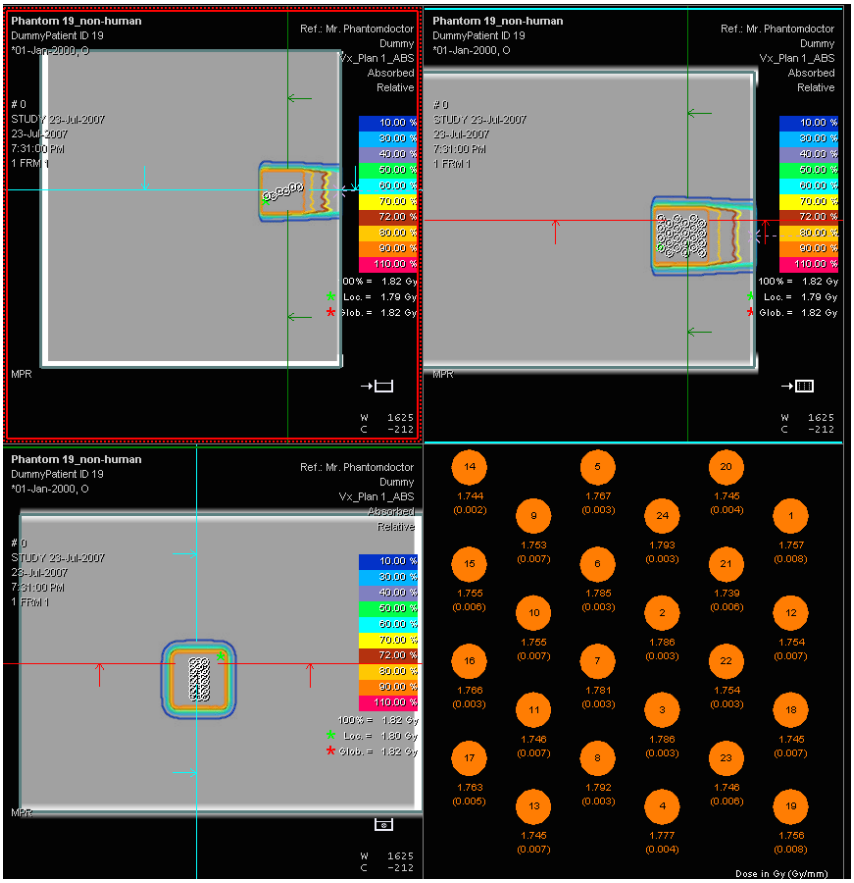

Figure 3.9. TPS representation of the isodose and ionisation chamber dose from the uniform cube irradiation. Image obtained from CNAO, with thanks to the medical physics team.

capabilities of MC dose calculation for less uniform irradiation fields.

Furthermore, as previously discussed, the mean deviation from nine different patient plans were evaluated and compared with respect to my simulations. Measurement points were obtained during the plan verification in addition to the calculated doses from the TPS. The plot below (Figure 3.11) represents the obtained results.

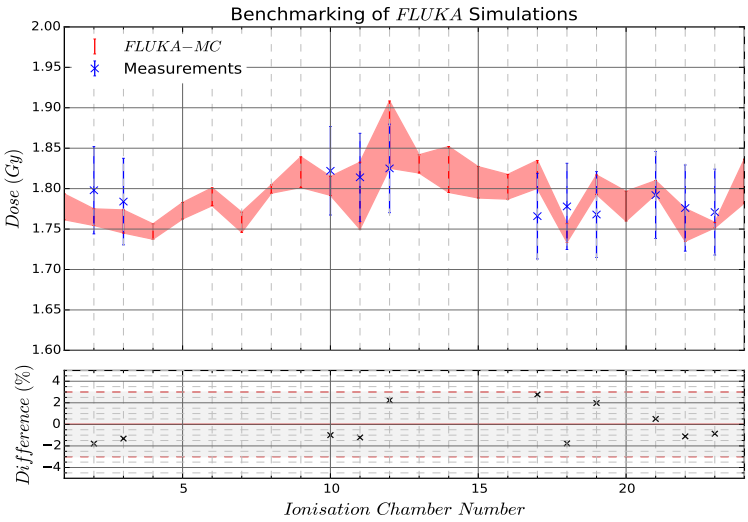

Figure 3.10. Calculated Dose Deposition and Deviations between Measurement and MC. On the top plot, blue points represent the ionisation chamber measurements and associated errors (set at 3% as previously described), and red points represent the introduced simulation, with its obtained uncertainties. On the lower plot, the calculated deviation between MC and measurements is shown, the shaded area represents the error associated with the ionisation chambers.

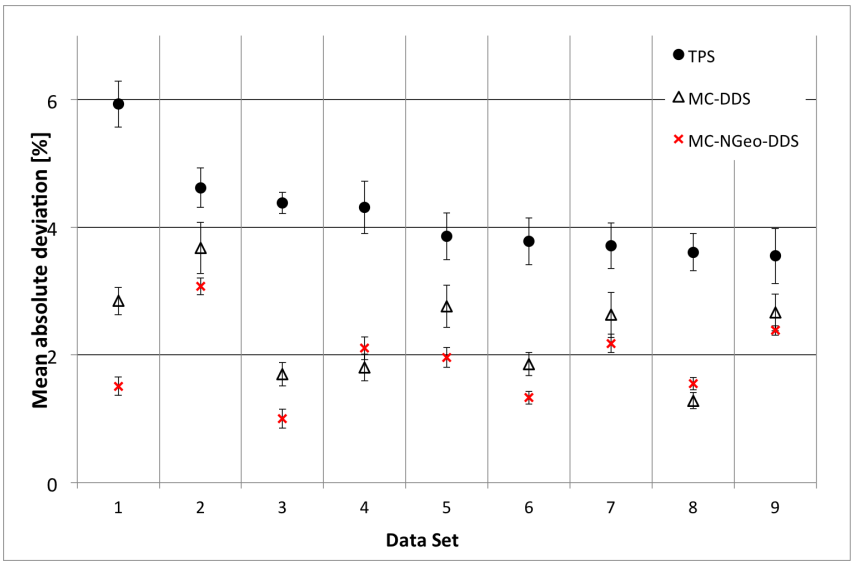

Figure 3.11. Calculated deviations between measurements, TPS (filled circles), original MC (triangles) and introduced MC simulation with improved geometrtic description of ionisation chambers and holder (red crosses).

When comparing deviations from the different dose calculations (TPS or MC) the one produced with the detailed geometry gave the closest agreement with the measurements, obtaining a mean of 1.90% versus 4.19% and 2.36%

from the TPS and other MC simulation, respectively. The other statistics obtained can be found in Table 3.1 below.

Table 3.1. Statistical analysis obtained from the different dose calculation methods.

	Relative Deviation from Measurements			
Values in (%)	Mean	Maximum	Minimum	Standard Deviation
TPS	4.19	5.93	3.55	0.75
Introduced MC	1.90	3.07	1.00	0.63
Original MC	2.36	3.68	1.28	0.75

In order to evaluate whether the differences between the original MC simulation and the MC simulation with detailed geometry are statistically different a student t-test was used. From this test, a sigma value of 0.048 was calculated, confirming the statistical difference of the obtained results.

3.4.2 Validation of Irradiation Target

Initially I measured the WEPL with respect to the selected material. The average ratio of the WEPL to the geometrical thickness of the phantom plates was 1.19 ± 0.02, compared to the value of 1.17 ± 0.011 obtained by Krämer et al. (Kraemer and Scholz 2000), and since the PMMA materials vary in composition and density between different vendors, it is somewhat expected that different results will be obtained for the WEPL. The measurements in Figure 3.12 left were performed using the same sampling. Variations between the curves with and without PMMA are due solely to the difference in edge sharpness.

Table 3.2. Range measurements obtained for WEPL measurements with Peakfinder.

All in mm	90% Proximal	90% Distal	50% Distal	10% Distal	Peak
Pure Peak	150.08	150.84	151.28	151.99	150.54
PMMA	126.21	126.96	127.42	128.48	126.67
Difference	23.87	23.88	23.86	23.51	23.87

Table 3.2 shows the difference obtained between the Bragg peak with

and without the presence of the PMMA. This information is also seen in Figure 3.12 in the left. Once these rages were obtained, the WEPL value was calculated. This WEPL was then introduced to the dose calculation, and for benchmarking purposes the effect of the dose calculation with the correct PMMA conversion was plotted (in this case FLUKA Monte Carlo simulations was used for comparison), and compared with the general PMMA description obtained by the dose calculation software. Regarding the correction with respect to the material, the measured doses corresponded to the calculated dose deposition (Figure 3.12). The results presented in this plot will be further described in the following chapter where the experimental set-up and results will be discussed.

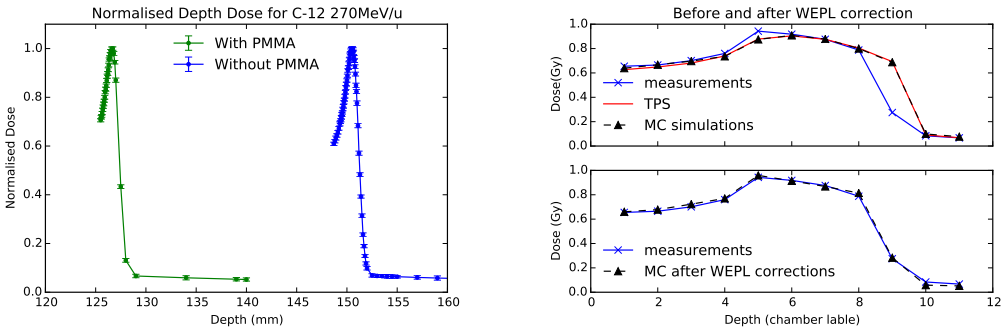

Figure 3.12. Left: Peak position measurements with and without PMMA slab. Right: SOBP before and after WEPL correction compared to experimental results

Moreover, I evaluated the material description of PMMA in respect to its density. Figure 3.12 shows that when using the default values, problems are evident in the beam range. In order to improve this simulation result, modifications were made to the material density. By default PMMA is described by having a density equal to 1.20 g/cm^3 but in literature it is possible to find reported densities between 1.21 to 1.17 g/cm^3. Figure 3.13 shows the variation obtained by these different densities.

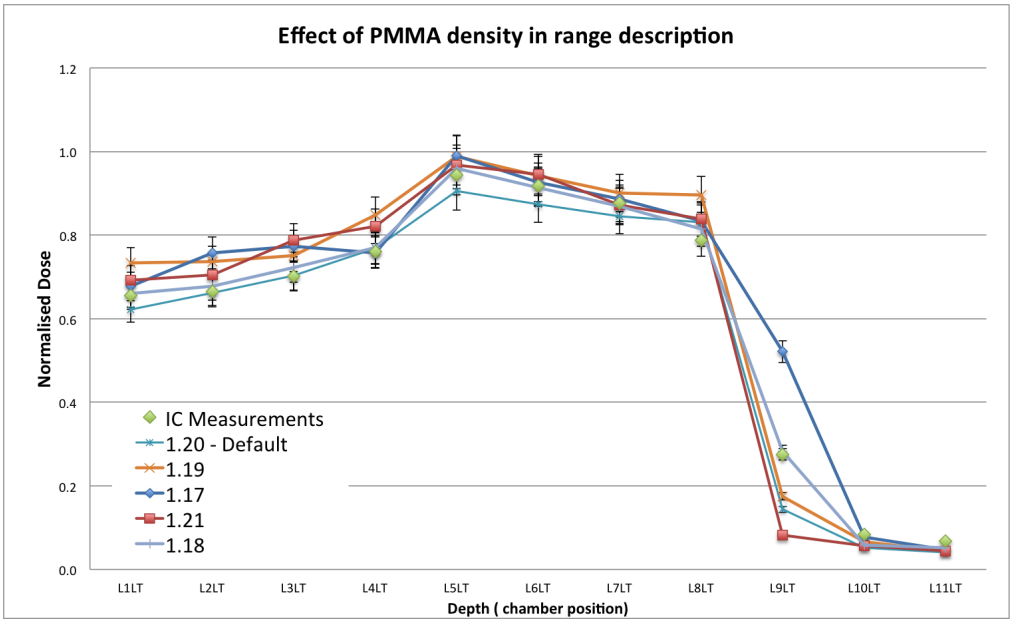

Figure 3.13. The effect of different PMMA densities in the FLUKA simulations in respect to the obtained measurements. The choice was made to use the value of 1.18 g/cm^3 for all simulations of the designed phantom. Y-axis represents the normalised dose and x-axis the detector position. The difference between one detector and the next is $1.00 \pm 0.01 cm$

The x-axis in this plot is the ionisation chamber position. The difference between one detector and the next is $1.00 \pm 0.01 cm$. The difference between the different simulation can be mostly noted in detector position 9, where the range description can be evaluated. It can be seen, that with the chosen value of 1.18 g/cm^3 for the PMMA density, the simulation describes well the measurements. For all simulations of the proposed phantom, this value was used.

3.4.3 Design Evaluation

The effect of the chosen detector position was evaluated. First of all, the Chamber-Chamber effect was evaluated followed by the evaluation of the dose deposition in the cell compartment.

Chamber-Chamber Effect

Table 3.3. Calculated deviations between 24 and 12 chambers with respect to measurements.

	Relative Deviation from Measurements			
Values in (%)	Mean	Maximum	Minimum	Standard Deviation
TPS	4.19	5.93	3.55	0.75
Introduced MC	1.90	3.07	1.00	0.63
24 Detectors	2.00	3.29	1.18	0.70

Since this modified simulation obtained comparable results to the measurements (Table 3.1), a new simulation was then performed with all 24 chambers and the results obtained were compared (as shown in Table 3.3). The comparison was made from the 12 (or 11) ionisation chambers present in both simulations for each of the 10 patient treatment plans. A two-tailed t-test was performed and no significant difference (sig. 0.76) was found between the two simulations with 12 or 24 chambers. Figure 3.14 shows the calculated deviations for each dose point for the different data sets for both MC simulations. This shows that at the used distance, disturbance will not be cause by detector to neighbouring detectors.

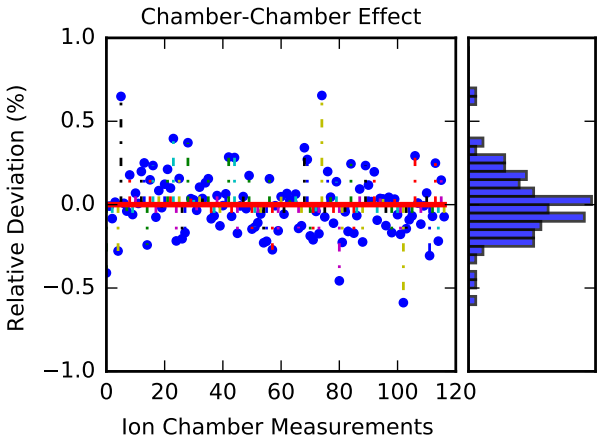

Figure 3.14. Calculated deviations between MC dose calculations with 12 and 24 ionisation chambers. The blue dots represent the calculated relative deviation between different ionisation chambers dose deposition for both configurations with 12 and 24 chambers. The red line represents the mean of these measurements and the right plot represents the histogram of these deviations.

Dose Distribution Disturbance in the Cell Region

Figure 3.15 shows the deviations obtained from the introduction of a high value of Z and high density material in the beam path, mimicking the effect in which the dose distribution would suffer from the presence of non-water equivalent detectors.

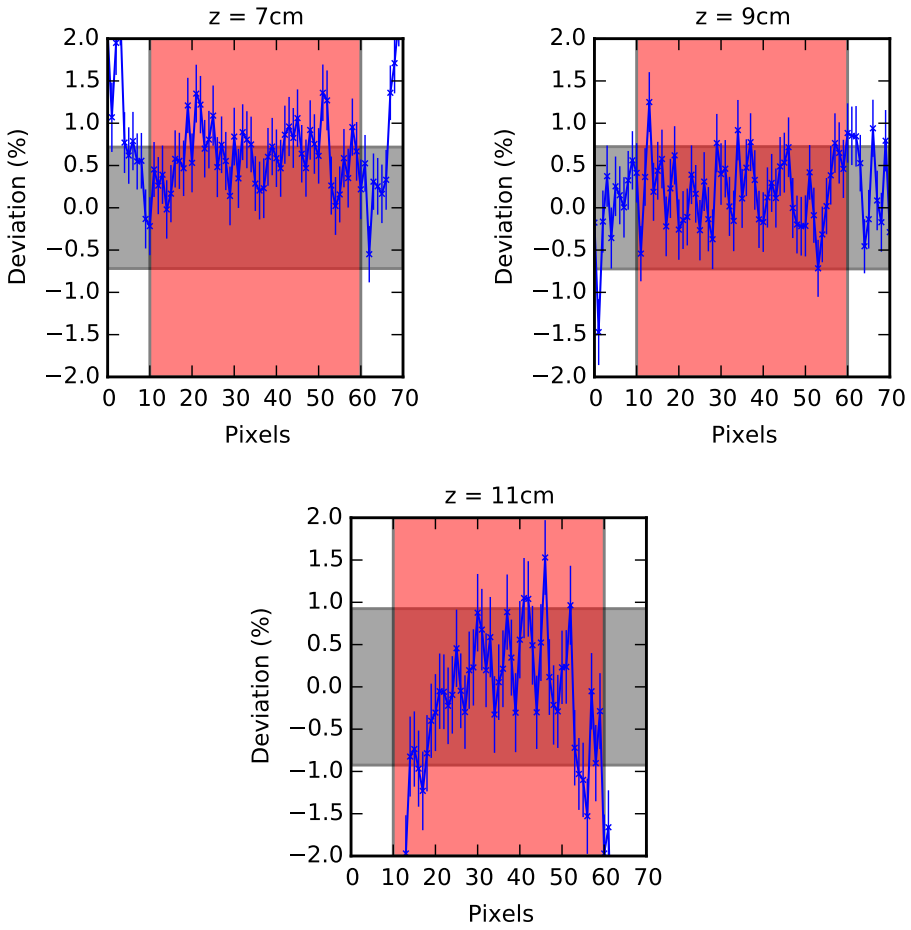

Figure 3.15. The dose difference was obtained from three profiles along the x-axis for different depths the first at the start of the SOBP at z=7cm, the second in the middle of the SOBP at z=9cm and the last at the end with z=11cm. The red area represents the location of the cell compartment and the grey area represents the 95% confidence interval.

The dose difference was obtained from three profiles along the x-axis for different depths the first at the start of the SOBP at z=7cm, the second in the middle of the SOBP at z=9 cm and the last at the end with z=11cm. The red area represents the location of the cell compartment and the grey area represents

the 95% confidence interval. No difference was observed as the deviation for most of the points are within the uncertainties of the measurements. This shows that for the central region where the cell compartment is located the presence of the detector will not introduce any non-uniformities in the dose deposition. This is important for the biological experiments where uncertainties in the dose deposition and range must be reduced or avoided.

3.5 Discussion

In this chapter, the limitations of the chosen phantom design were analysed. Firstly, the MC simulations had to be evaluated since they were used for all the further steps in the design evaluation. With respect to benchmarking of the MC simulations, for the simplistic scenarios where the dose distribution was relatively easy, that is, where there was a uniform dose distribution, it was observed that the calculated deviations were within the MC uncertainties of 2.91 % and within 2.76% (Figure 3.10). Whenever a non-uniform dose distribution occurred, it can be seen from Figure 3.11 that improving the geometrical description of the simulation represents an improved agreement with the measurements in comparison with not only the TPS but also the current MC approach used clinically. Therefore after these modifications to the geometry description, a good agreement was obtained.

Once the MC simulations were validated, I was able to show that no significant difference was observed between the simulations with 12 versus 24 ionisation chambers (Figure 3.14). Since the chosen distance in the proposed phantom was similar to the ones used in this commercial phantom, it was confirmed that these positions would not interfere with the future measurements. This allowed the current design to be tested for possible disturbances in the central region where the cell culture would be placed.

Lastly, I evaluated the dose deposition in the cell compartment. The MC analysis (Figure 3.15) showed that most of the points, in the desired region, were within the confidence interval of 95%, which demonstrated that there was

no significant difference in the delivered dose with the use of the detectors. Few points fell outside of this confidence interval. Those which did can be explained by statistical fluctuation or poor uniformity of the original beam profile. Despite these few points outside the confidence interval, the results could be seen as satisfactory as all points lay within 1.0% of the original, which corresponds well with dosimetry requirements.

The only possible limitation was the chosen phantom material, but, as demonstrated above this limitation can be overcome by accounting for the material WEPL during the calculation of the irradiation plans (Figure 3.12), as has been discussed in the literature (Jaekel et al. 2001a).

In Chapter 2, I introduced the phantom criteria needed to obtain more a reliable radiobiological results. The criteria were divided into:

- Dosimetric uncertainties; and
- Biological uncertainties.

Dosimetric uncertainties refer to the limitations arising from the different set-ups and chosen detectors. Biological uncertainties in this thesis are related to biological limitations that can be overcome. For example, the use of sterilised commercial tools for cell plating and multiple irradiations at same conditions to avoid batch effects. In contrast to errors associated with intrinsic biological limitations cannot be overcome. For example plating efficiency that is both cell and surface type dependent.

3.5.1 Dosimetric Uncertainties

Dosimetric uncertainties will affect the results in two possible ways, either be not being able to correctly evaluate the dose profile or by disturbing the beam which will irradiate the cells. In both cases, wrongly dose reporting diminishes the biological results.

In relation to the different set-ups described in the previous chapter, some groups (Combs et al. 2012; Elsaesser et al. 2010) either do not report their

dosimetric methods or do not perform dosimetry and by doing so rely on the capabilities of the delivery systems. A recent clinical review on patient plan verification (Molinelli et al. 2013) showed that 86% of irradiation plans were within clinical limits of ± 3% mean deviation between calculated and measured doses. For the cases where the results were above these limits a re-calculation of the plans with the dose delivery beam information showed that the mean deviation, in the worst cases reduced from 5% to 2.5%, but in general an average 1.5% reduction in the mean deviation was obtained. This was due to mechanical limitations when delivering the different beam positions that differed by a few *mm* between the irradiation plan and delivered beam which demonstrates a source of limitation with these devices. As for the proposed phantom, these limitations would be noted during irradiation and the correct dose profiles could be calculated, thereby allowing for correct reporting of dose delivered to cell compartment.

Other groups use set-ups that are also capable of evaluating the beam delivery (Bert et al. 2010; Mitaroff et al. 1998; Barazzuol et al. 2012), but different to the proposed design, the implications, by the introduction of these detectors, have not been assessed specially in respect of the inter-detector interference and dose deposition disturbance in the cell compartment.

Clinically each individual ionisation chamber is calibrated by a standard laboratory for absolute dosimetry and the used of multiple, near by, chambers were evaluated. I found that the mean deviation between sets of data containing half of the detectors provided the same results as sets of data with the full set of detectors (mean deviation of 1.90 versus 2.00 % respectively for incomplete and complete set of detectors in the measurements). This demonstrate that the detector measurements with the proposed phantom were free from any disturbance arising from the adjacent detectors (no significant difference was found, calculated two-tailed student t-test sig. 0.76). This gives confidence in the measured values allowing for a, comparison with the MC simulations. These distances are also used by other groups, but had not been previously tested (Bert et al. 2010).

In addition, by aligning the detectors outside the beam path to the cell compartment area, the results of the phantom showed that the cell irradiation region was free from introduced disturbances since I was able to demonstrate that the hypothesis which proposes that there is no variation when introducing chambers found to be valid at a confidence level of 95% for 95.3% of the evaluation points. Other groups (Mitaroff et al. 1998; Barazzuol et al. 2012) use different detectors (films or TLDs) in the beam path of the cell compartment which can influence the dose profile by the presence of different WEPL. No evaluation for these uncertainties in the dose distribution have been performed. In Figure 3.15, the areas outside of the red shaded area show that deviations up to ± 2% can be introduced by the introduction of detectors in the beam path.

3.5.2 Biological Uncertainties

The limitations concerning biological output are directly linked to the reported dose. By the reduction of dosimetric uncertainties the reliability in radiobiological results is improved. In addition to this, as mentioned previously this phantom was built in order to use commercially available cell plating tools which allows for multiple irradiations with cells produced at the same time (this is evaluated in Chapter 5) and reduce uncertainties in sterilisation.

3.6 Conclusion

In this chapter, I evaluated some aspects of the phantom design and the computational tools which are used in the next chapters. The main attribute of the phantom is its superior dosimetry output. As described in previous chapters, the majority of radiobiology experiments either have limited or non-existent dosimetric information.

The results contained in this chapter encourage the use of dose distributions obtained by the MC simulation. This gives the possibility of using the MC calculated dose distribution in the cell compartment region by evaluating indi-

vidual irradiation plans and comparing the obtained ionisation measurements to the MC dose distribution at the detector positions. The possibility of using these dose grids calculated by the MC enables the evaluation of cell survival by multiple physical and biological variables with a uncertainty at the level of the uncertainty of the detector used.

The work in this chapter demonstrates that the chosen detector positions would not disturb the dose distribution in the cell compartment and, therefore, would not introduce uncertainties in the experimental results. Moreover, it proves that it is possible to trust in the translation of the ionisation measurements into the dose information at the cell compartment region since a good agreement was obtained between the dose grid calculation by the MC and the ionisation measurements.

Furthermore, the results presented in this chapter demonstrate the superior dosimetric output that is obtained by this phantom in respect to other set-ups either by correctly describing the dose profile (limitations on dose delivering systems found in 14% of irradiation beams with errors up to 2.5% in the dose delivery) or by not introducing extra uncertainties in the beam path (calculated around 2% deviation by the introduction of detectors in the beam path).

Chapter 4

Dosimetric Measurements of Hadron Beams

4.1 Aim

The aim of this chapter is to verify the irradiation plan at different stages by analysing the dosimetric output of the phantom, and I will demonstrate that with the proposed design the calculated dose distribution can be correlated with the measured dose points within 3% (relative uncertainty of the ionisation chamber). And that the dose calculation for the whole target area of the phantom can be validated in order to correctly report the irradiation dose of the cell compartment. The calculated dose distribution in the whole phantom could be obtained and the cell response in the cell compartment could be correlated to the calculated dose distribution.

4.2 Introduction

The proposed phantom is capable of using commercially available tools for cell culture which enables multiple irradiations to take place and provides for an online response from the delivered irradiation, allowing for higher dosimetric precision, additionally to simulating patient irradiation conditions.

In this chapter, the data from several experiments will be presented and

analysed. As previously described, with the aid of the phantom the user is able to monitor the absorbed dose during radiobiological experiments allowing for an initial verification if the irradiation conditions were met. This allows for, any mispositioning to be identified and corrected prior to proceeding with the cell analysis, which is more labour intensive and time consuming. This assessment of delivered dose also helps to verify different systems' capability of delivering the planned dose.

4.3 Methods

The phantom dosimetry has been determined from four different irradiations, at two different facilities, varying the beam parameters to match different target geometries within the phantom. Before describing each experiment in detail, common features to all of experiments are outlined.

4.3.1 Multi-Centre Evaluations

Dose modelling and detector measurements were compared for the different experiments so as to evaluate the accuracy of dose modelling for each irradiation and facility. For all experiments, the physical dose or absorbed dose to water in Grays [Gy] was measured at different detector positions using ionisation chambers. Irradiations were performed with carbon-ion and proton beams, except the first experiment at HIT where only carbon ion beams were used.

The goal was to benchmark the different dose modelling in respect to the detector measurements in order to validate the dose calculation in the cell compartment region.

4.3.2 Facilities

These irradiations were performed at CNAO and HIT facilities. At that time, they were the only facilities in Europe which were clinically treating patients with both proton and carbon ion beams and were widely recognised for their

expertise in ion beam treatments.

CNAO

The Italian National Center for Oncological Hadron Therapy (CNAO) is a hospital-based hadrontherapy facility equipped with a custom synchrotron and dose delivery system (DDS) which provides actively scanned proton beams with energies of 62–227 MeV/u and carbon ion beams of 115–400 MeV/u, corresponding to ranges in water of 3-32 cm and 3-27 cm for protons and carbon ions, respectively (Rossi 2011).

HIT

The HIT facility is connected to the neighbouring buildings of all clinical departments of the University Hospital on the Campus of Heidelberg. A library of pencil beams variable in energy, focus and intensity and ion species ranging from protons to oxygen are provided by a linac-synchrotron combination with a diameter of 20 m. The maximum energy for clinical applications is 221 MeV for protons and 430 MeV/u for carbon ions. The range resolution in water is 1 mm for proximal depth and 1.5 for distal depth. The beam width ranges from 4-15 mm and the dose homogeneity is in the order of ±5% in over 80% of the treatment field (Combs et al. 2010).

4.3.3 General Specifications

The phantom followed the individual facility procedure for patient irradiation (Molinelli et al. 2013) from imaging, planning and quality assurance. Spot scanning technique was used and a uniform dose (either absorbed [Gy] or RBE-weighted [GyE]) distribution was chosen. These irradiations plans were then used as input for the MC simulations, where RBE-weighted dose is the product of the absorbed dose and the relative biological effectiveness (RBE) factor. In the case of proton plans, a RBE-factor of 1.1 was used and for carbons the factor was calculated with the LEM-I model (Kraemer and Scholz

2000; Kraemer et al. 2000) by the TPS.

In all experiments the phantom was fitted with 22 PMMA mock ionisation chambers placed in the detector holder positions and it was scanned with a typical scan protocol used in clinic for cranial treatments. The position of the phantom in respect to the irradiation isocenter was manually defined during the CT imaging and recorded with fiducial markers, so that the selected set-up could be easily reproduced in the treatment room. The use of treatment motorised tables and laser positioning systems reduced positioning uncertainty between planning stages and irradiations. After the scan the images were transferred to the treatment planning system.

Using the CT images (1 mm^3 voxel size) a 3D model of the phantom and the predefined target volume was defined. The irradiation plan aimed to provide a homogeneous coverage of the target volume with different physical doses by one single horizontal field. The expected physical mean dose for each detector was recorded and the plans were approved and sent to the irradiation room. All treatment planning steps were performed by the CE-marked *syngo*® RT Planning by Siemens AG Healthcare (Erlangen, Germany) version VB10, which is based at the TRiP98 (Kraemer and Scholz 2000; Kraemer et al. 2000).

After the plan calculation, the irradiation took place. The data set in all measurements consisted of the simultaneous use of 24 (when available) ICs (PTW model 31015), connected by two multi-channel precision electrometers (PTW Multidos). A graphical description of the phantom and beam orientation is found in Appendix A.

Since cell survival had also been evaluated (see Chapter 5 for more details) for the experiments performed at HIT, the decision was taken to irradiate the phantom with a uniform absorbed dose instead of the biological dose approach that was used for the CNAO experiment. This was done in order to reduce any possible sources of uncertainties included in the biological dose calculation model as discussed in the literature (Boehlen et al. 2012). One example used from the literature included the method in which the RBE-factor is calculated according to different input parameters, related not only to the

physical properties of the used beam, but also the target cell line. This method would also be applicable for my experiment since the cell line inputs currently available differed from the one used.

At these experiments performed at HIT were also obtained both dosimetric and biologic measurements. The biological output of the phantom including the description of the different experimental set-up for these experiments are described and discussed in the Chapter 5.

Dosimetry

Ionisation chambers (PTW-Freiburg GmbH Pinpoint chamber Type 31015) connected to PTW-Freiburg GmbH Multidos Webline electrometer were calibrated in terms of absorbed dose to water. Each irradiation was measured and converted to physical dose according to TRS-398 (IAEA 2000) and described by the equation 4.1 below:

$$D_{w,Q} = M_Q N_{D,w,Q_0} k_{Q,Q_0}, \tag{4.1}$$

where M_Q is the reading of the dosimeter taking into account the product Πk_i of correction factors for influence quantities (i.e. temperature, pressure and recombination corrections), N_{D,w,Q_0} is the calibration factor in terms of absorbed dose to water at a reference quality Q_0, and k_{Q,Q_0} corrects for the difference between the reference beam quality Q_0 and the actual quality Q being used.

During HIT experiments, 24 ionisation chambers were used in contrast to CNAO experiments where only 12 ionisation chambers were available at the time of testing. These pin-point ionisation chambers have vented sensitive volume of 0.03 cm^3 (which requires air density correction) with inner diameter of 2.9 mm, the wall material is graphite with a build-up cap made of PMMA and aluminium anode.

During some of the irradiations, the phantom was also irradiated with the presence of radiochromic EBT3films (ISP) before the cell compartment to check

the homogeneity of 2D dose distributions for scanning beams. The main focus of the measurement was not an absolute dosimetric evaluation of the profiles, which would demand further extensive studies, but rather an evaluation of the homogeneity of the optical densities.

Monte Carlo Simulations

As previously discussed in Section 3.2.1, FLUKA is the MC code chosen for dose simulations. As result of these simulations, a dose deposition in water is calculated in a 3-D grid of $1mm^3$ voxel size. This voxel size is chosen to be the same dimensions of the CT imaging size.

Data Analysis

Pursuant to the quality assurance procedures of both CNAO and HIT (Molinelli et al. 2013) each ionisation chamber measurement values were compared with those values calculated by the Monte Carlo simulations. For the Monte Carlo simulation results, the 3-D matrix was sampled and I was able to obtain the deposited dose in the chambers by calculating the average dose to water over several voxels, corresponding to the active volume of the detector situated in the positions where the chambers would be located. For each data set analysis, the mean deviation was calculated as the difference between measured ($d_{meas,i}$) and calculated dose ($d_{calc,i}$), normalized to the maximum beam dose (d_{max}) and averaged over N IC positions i:

$$\frac{1}{N}\sum_{i}\frac{|d_{meas,i}-d_{calc,i}|}{d_{max}}\% \tag{4.2}$$

The number of points N included in the calculation can be equal or lower than 24, depending on the data set.

For QA measurements, based on previously reported experiences with actively scanned particles (Molinelli et al. 2013) in reference conditions, the applied acceptance threshold was set to 5% for both mean deviation and standard deviation over a data set. Both the mean and the standard deviation

of the measurements were analysed. The reason for doing so was to benchmark individual irradiation plan to obtained biological data.

In addition to the ionisation measurements and comparison, whenever the film dosimetry was available, horizontal and vertical profiles were measured and variations of the uniformity were assessed across x- and y- axes (perpendicular to the cell compartment and beam). Uniformity was defined as the difference between maximum and minimum values obtained for the optical density divided by the their sum.

$$Uniformity = \frac{v_{max} - v_{min}}{v_{max} + v_{min}}\% \tag{4.3}$$

Although this assessment provides a direct representation of the uniformity of the delivered dose distribution, it is more susceptible to non-uniformities owing to the films used and pixel defects in the reading scanner. Therefore, another more useful assessment of uniformity is to evaluate the coefficient of variance, which represents the spread that describes the amount of variability relative to the mean. The coefficient of variation (CV) is defined as the ratio of the standard deviation σ to the mean μ :

$$CV = \frac{\sigma}{\mu}\% \tag{4.4}$$

4.3.4 Technical Description

In this section the different experimental set-up for each measurement performed will be described including, the Monte Carlo output used and the data analysis performed.

The different irradiation plans are shown in Figure 4.1 and their technical details are described in Table 4.1.

At CNAO, the phantom was irradiated with a uniform dose of 2.0 GyE for protons and 3.0 GyE for the carbon plan, which corresponds to the clinical fraction dose used for protons and carbon ions, respectively. The nominal energy for the carbon plan ranged from 163.4 to 231.4 MeV/u with spot size

ranging form 6.5 to 5.5 mm respectively, in a total of 51 energy steps for a total of $3.0x10^9$ particles. The LEM model was used for obtaining the RBE. For the proton plan, the nominal energy range varied from 84.3 to 119.5 MeV with spot size ranging from 15.4 to 11.5 mm in 49 energy steps for a total of $1.4x10^{11}$ particles. For protons, as mentioned above, the 1.1 RBE factor was used. Since at CNAO only 12 chambers were available, the uniform dose distribution was set to cover half of the phantom (as seen in Figure 4.1). In relation to depth, the SOBP was set to be uniform (biological dose) in a section of 5 cm in the middle of the phantom in order to have both build-up and exit dose areas within the measurements. The decision was taken to use RBE-weighted dose for these plans in order to evaluate the range uncertainty and the WEPL at different conditions (sharp edge and gradient dose profile). In the case of protons the deviation is more evident owing to the sharp edge and less so in the carbon beam owing to the applied gradient along the SOBP.

Table 4.1. Technical description of experimental set-ups.

	CNAO	HIT Experiment 1	Experiment 2	Experiment 3
SOBP	5 cm	10 cm	12 cm	5 cm
Dose Points	2.0 GyE (p) 3.0 GyE (^{12}C)	0.5, 1.0 and 3.0 Gy (^{12}C)	1.0, 2.0 and 4.0 (p, ^{12}C)	1.0, 1.5, 2.0 and 4.0 Gy (p, ^{12}C)
Number of Energies	49 (p) 51 (^{12}C)	74 (^{12}C)	36 (p) 38 (^{12}C)	70 (p) 74 (^{12}C)
Detectors	ion chambers and films	ion chambers	ion chambers and films	ion chambers and films

In this irradiation setting, each measurement data set consists of the simultaneous use of 12 ICs (PTW model 31015), connected by a multi-channel precision electrometer (PTW Multidos). For each irradiation plan, at least two consecutive measurements were performed and the mean values taken. EBT3 radiochromic films were also used to assess the uniformity of delivered dose distribution. The films were placed at the beginning and end of the SOBP.

Three irradiations took place at HIT. In all measurements, the data set

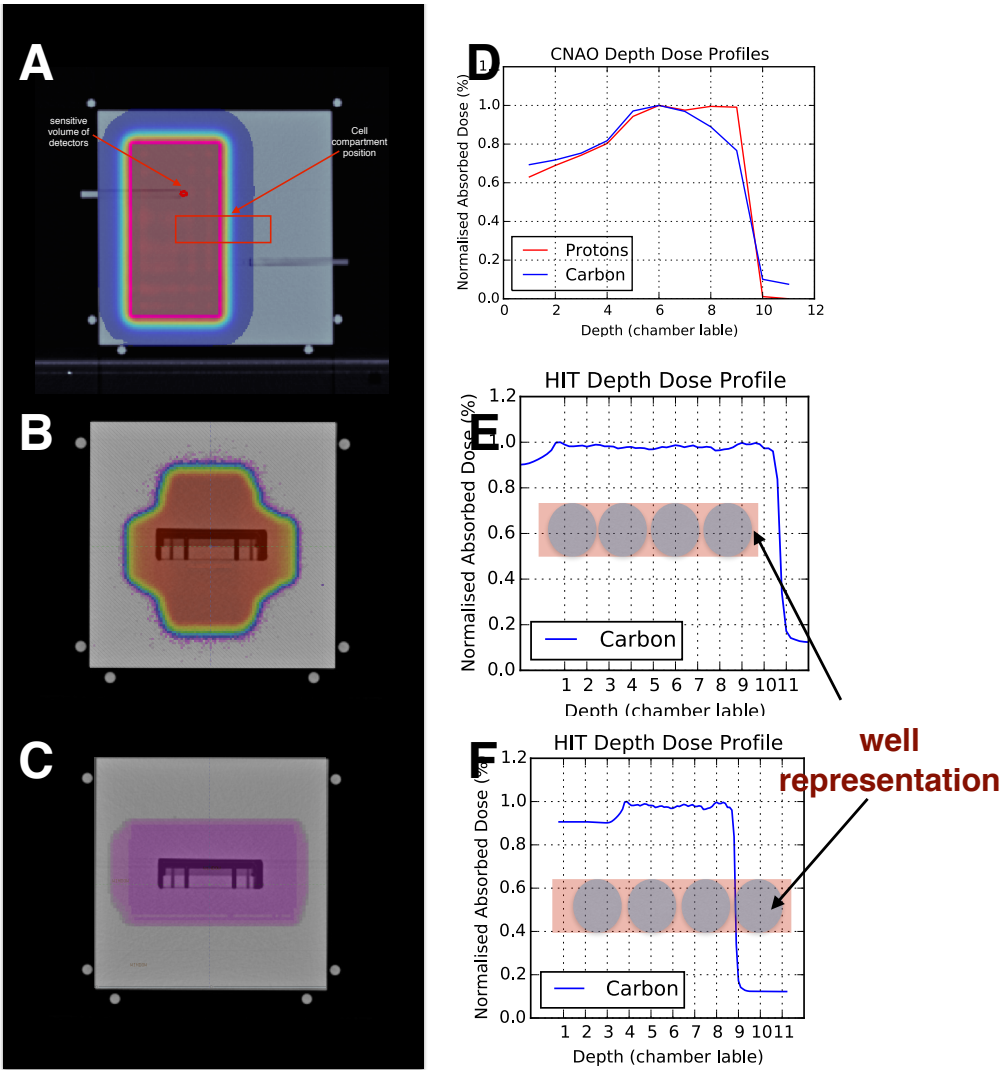

Figure 4.1. Irradiation plan for the different experiments. Beam eye view from experiment at CNAO (A), HIT experiment 1 (B) and HIT experiments 2 and 3 (C). Representation of depth dose profile along detectors. D for the experiment at CNAO where the SOBP covers partially the detector positions; E for the experiments at HIT 1 and 2 where the SOBP covers all detectors: and F for the experiment 3 at HIT where only the central two wells are covered by the SOBP and subsequently the detectors in the middle of the phantom. In both E and F the representation of the well plate is visible. Uniform absorbed physical dose has been used in the irradiation plans at HIT and RBE-weighted dose at CNAO.

consisted of the simultaneous use of 24 ICs, connected by two multi-channel precision electrometer (PTW Multidos).

In the first irradiation, the dose calculations were performed for 0.5, 1.0 and 3 Gy. The nominal energy for the carbon plan ranged from 88.8 to 255.8 MeV/u with spot size ranging form 9.8 to 6.1 mm respectively, in a total of 74 energy steps for a total of approximately $2.0x10^9$ particles for each 0.5Gy delivered. An uniform absorbed dose to cover the cell flask and detector positions was used, as shown in the Figure 4.1.

At the second experiment at HIT the cell response was evaluated for both carbon ion and proton beams in contrast to the previous experiments. The delivered absorbed doses were 1.0, 2.0 and 4.0 Gy. The decision to use different dose points in relation to the previous experiment were based on the fact that different cell lines were being irradiated. The dose points were selected to match those recommended in current literature for the new type of cell lines used(further information can be found in the Chapter 5). The nominal energy for the carbon plan ranged from 88.8 to 255.8 MeV with spot size ranging form 9.8 to 6.1 mm respectively, in a total of 38 energy steps for a total of approximately $2.0x10^9$ particles for each 0.5 Gy delivered. The irradiation plan was adapted in relation to the irradiation volume. In respect to the depth, it continued covering the entire cell compartment (12 cm), but laterally it was reduced to a margin of 2 cm around the cell compartment. An uniform absorbed dose to cover the new irradiation target was used, as shown in Figure 4.1. Radiochromic films EBT3 were also used at two different depths, before and after the cell compartment.

A third irradiation was performed at HIT. The nominal energy for the carbon plan ranged from 88.8 to 255.8 MeV with spot size ranging form 9.8 to 6.1 mm respectively, in a total of 74 energy steps for a total of approximately $2.0x10^9$ particles for each 0.5Gy delivered. In total, 4 irradiations for each particle type was delivered (1, 1.5, 2 and 4 Gy). The irradiation plan was adapted with respect to the SOBP position and length so as to evaluate the cell survival in different positions along the beam path. With the new configuration,

the SOBP was positioned in the centre of the multi-well cell plate covering the two middle rows (5 cm). By doing so, I was still able to study cell survival in relation to the LET variation along the SOBP as well as the entrance dose (at the first row of the cell plate) and the exit dose (at the last row of the cell plate) for different doses.

4.3.5 Specific Aims

In summary, the phantom was irradiated at different experiments. During the different irradiations, different irradiation plans were set in order to evaluate different aims. The aims for each experiment were as follows:

- Experiment performed at CNAO, whose results have been partially described in Figure 3.12: The aim of this experiment was to validate the computational tools and materials corrections applied in the dose modelling.
- Experiment 1 performed at HIT: The aim of this experiment was the evaluation of the phantom's usability in a biological experiment and revalidation of the new irradiation plan for a new facility.
- Experiment 2 performed at HIT: The aim of this experiment was the evaluation of a new irradiation plan with reduced irradiation volume.
- Experiment 3 performed at HIT. The aim of this experiment was the evaluation of a full radiobiological experiment, including clonogenic cell survival, a reduced irradiation target along the SOBP and improved uniformity.

Figure 4.2 gives a overview of the different experiments including aims and beam information. The complete description of each experiment including information on the beam description, performed dosimetry including detector corrections have been described above and the obtained results can be found below.

Figure 4.2. An overview of the characteristics of the different experiments performed with the phantom.

4.4 Results

This results section will describe the outcome for each aim set forth in Section 4.3.5. The overall discussion of the results will be covered in the conclusion.

4.4.1 CNAO Results - MC Simulation Benchmark for the First Irradiation Plan including Verification of WEPL Correction

Film Measurement Firstly, an analysis of the uniformity of the delivered beam at different depths was conducted using the radiochromic films. This procedure was performed for all the depths from 1 to 9cm with 1cm steps. Figure 4.3 shows the obtained results for the first and penultimate films for the ^{12}C ion beam irradiation. These steps were chosen as they represented both the first and last beam within 80% of the SOBP. At each depth, the optical density for each pixel value (top) and the calculated difference (bottom) was obtained. The plot at the top also displays the uniformity and the coefficient of variance that were calculated as per Equations 4.3 and 4.4. This uniformity in then expressed in the bottom plot as dashed lines.

The optical density was obtained by two profiles with sampled normalised values in two orientations represented by the blue (horizontal) and red (vertical) lines. The calculated uniformity for the first film was 1.77% and CV of 0.61%.

The uniformity for the penultimate film was 2.01% with CV equal to 0.63%. As expected, greater variation in the uniformity was observed towards the end of the SOBP, mostly owing to the introduction of the ionisation chambers. The CV was able to represent a general information about the uniformity, which is the reason for a lower variation.

The same analysis was repeated for the proton beam (Figure 4.4).

Greater variation was also observed at greater depths, although in contrast to the ^{12}C, proton uniformity was noticeably poorer. This is the result of the greater scatter and beam spreading which proton beams are more susceptible

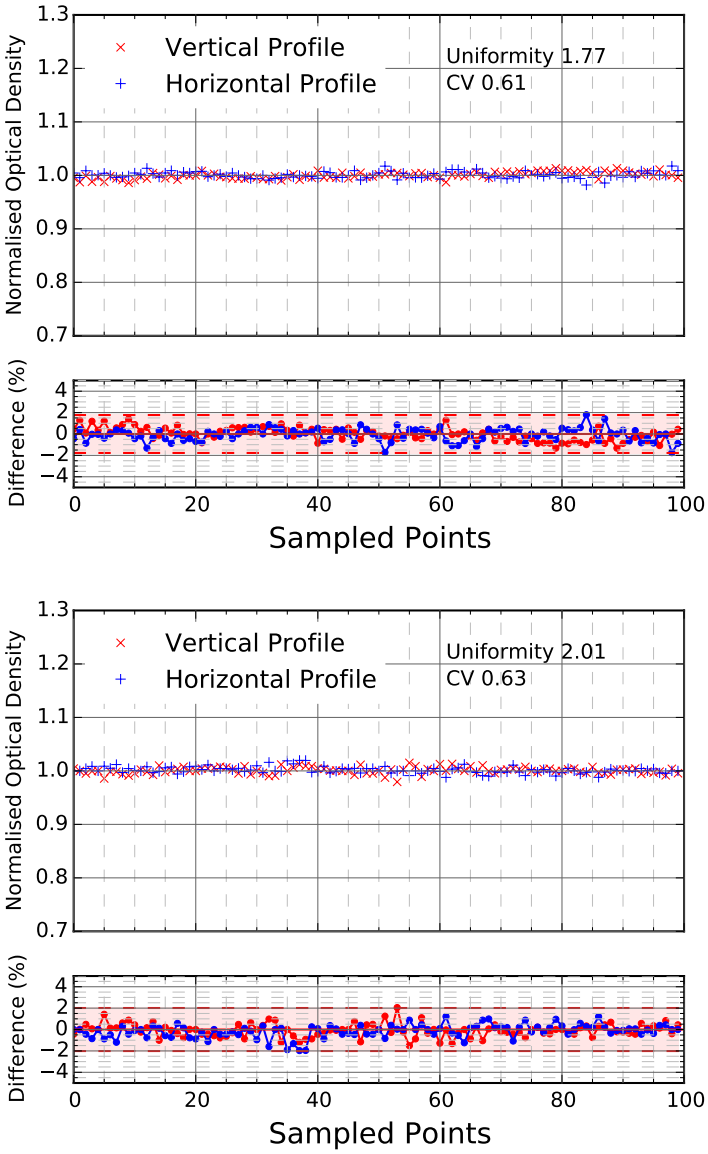

Figure 4.3. Uniformity analysis of the delivered ^{12}C ion beam at first film placed at the beginning (top) and at the end (bottom) of the SOBP. Top - obtained optical density for each pixel value; bottom - calculated deviation. The calculated uniformity has been annotated in the top plot and then expressed as dashed lines in the bottom plot.

to.

The reason for using the films was to assess the uniformity of the delivered dose distribution on the regions where the chambers were not present. Hence a new analysis of the uniformity was performed without the distortion from the ionisation chambers.

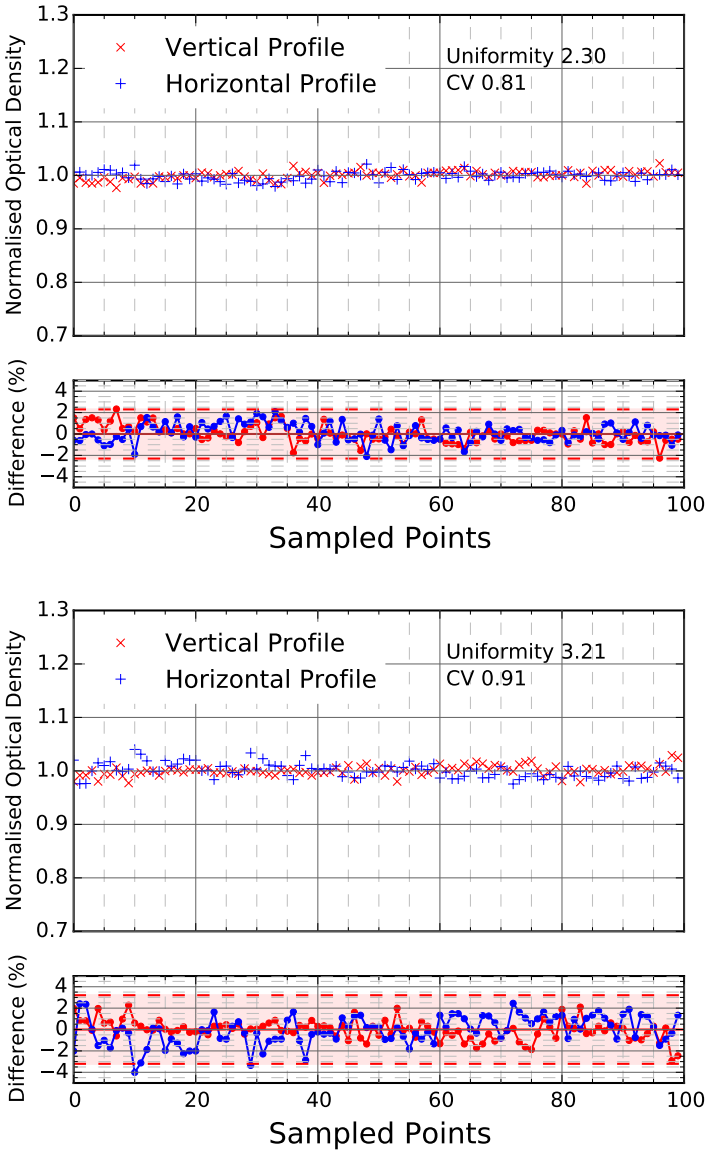

Figure 4.4. Uniformity analysis of the delivered p beam at film placed at the beginning (top) and at the end (bottom) of the SOBP. Top - obtained optical density for each pixel value; bottom - calculated deviation. The calculated uniformity has been annotated in the top plot and then expressed as dashed lines in the bottom plot.

The final calculated uniformity for the proton beam was between 2.30% in the beginning of the SOBP and 3.21% in the end part of the SOBP.

Ionisation Chamber Measurements Figure 4.5 compares each measurement taken with the ionisation chambers in relation to the calculated dose from

the MC simulation and TPS. For both beam qualities, the measured doses are listed in Table 4.2. The results were compared to the expected dose of 2 GyE and 3 GyE for protons and carbon ions respectively. The mean dose differences of 1.74% for protons and 1.37% for carbon ions were within the estimated total uncertainties of ionisation chamber measurements based on uncertainty budgets from TRS-398 recommendations.

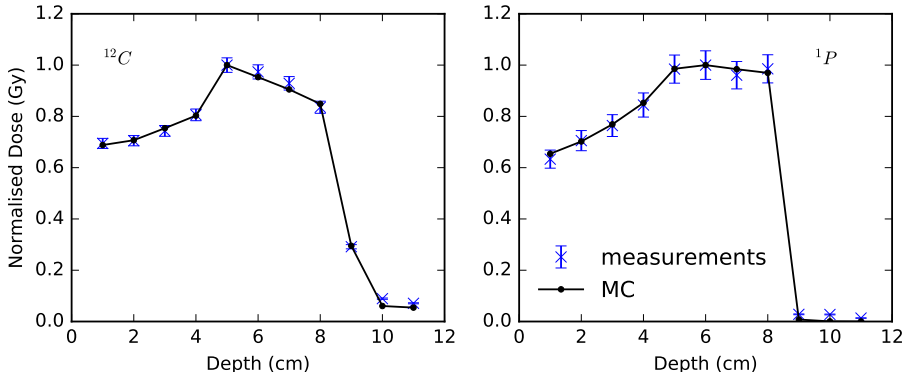

Figure 4.5. Comparison between measurement and MC simulations for ^{12}C ion beams and p, left and right respectively.

These results, together with the data collected from the aforementioned procedures (Section 4.3.3), were used as a means of analysing the average and standard deviation of the measurements. These results also lay well below the local CNAO quality assurance acceptance levels of 5% obtained deviation between physical dose measurements and calculations.

The observed difference between p and ^{12}C results were a result of the worsening broadening of the beam suffered by the protons since the uniformity at that depth was more affected than during irradiation as expected. This caused the increased deviation observed (Table 4.2, Figure 4.3).

Table 4.2. Obtained dose deviations from measurements for each beam type.

	Average(%)	Std. Dev. (%)	Max (%)
Carbon	1.37	0.80	2.60
Protons	1.74	1.04	3.78

4.4.2 Evaluation of biological usability of the phantom and re-validation of irradiation plans Results

Experiment 1 at HIT- Evaluation of Phantom Usability in a Biological Experiment and Re-validation for a New Facility and New Irradiation Plan.

Ionisation Chamber Measurements - As described previously, during this experiment only ionisation chambers were used for measurements. This was owing to the fact that the experiment served as basis for testing the usability and user-friendliness of the phantom as a biological dosimetric tool. The HIT's quality assurance procedures were followed (Karger et al. 1999) and, similarly to the experiments conducted at CNAO, the resulting measurements were compared to the dose calculation using MC simulations (Table 4.3).

Table 4.3. Obtained dose deviations from measurements at HIT.

	Dose (Gy)	Average (%)	Std. Dev. (%)	Max (%)
^{12}C	$0.5Gy$	2.16	1.11	5.51
	$1.0Gy$	1.39	1.15	5.10
	$3.0Gy$	1.86	1.54	4.03

In a similar manner to the aforementioned experiments conducted at CNAO, these results fell well within QA acceptance levels of 5% , which consequently helped to obtain a good agreement with detector measurements and subsequently obtained cell survival. This allowed for a full dosimetric assessment (Desrosiers et al. 2013) and beam characterisation with dose calculating tools to be performed.

Experiment 2 at HIT - Evaluation of New Irradiation Plan with Reduced Irradiation Volume

Film Measurement - An analysis of the uniformity of the delivered beam at different depths was conducted using radiochromic films.

This procedure was performed before and after the cell compartment at two depths, of 0.95 and 13.65 cm, respectively. During this experiment, films could only be placed before and /or after the cell compartment due to the presence of the cell container. As previously described for the other experiments, from each of these films the normalised optical density for each pixel value (top) and the calculated difference (bottom) were calculated and plotted. The top plot also displays the uniformity and the coefficient of variance that were calculated as per equations 4.3 and 4.4. This uniformity is then expressed in the bottom plot as dashed lines.

Figure 4.6 shows the obtained results for both films used for the ^{12}C ion beam irradiation. The optical density was obtained by two profiles sampled normalised values in two orientations represented by the blue (horizontal profile) and red (vertical profile) lines. The calculated uniformity and CV for the first film were 4.83% and 1.69%, respectively.

The uniformity for the last film was 3.42%, while the calculated CV was 1.41%.

Figure 4.7 shows the obtained results for both films used for the protons beam irradiation. The optical density was obtained using two profiles along two orientations represented by the blue (horizontal profile) and red (vertical profile) lines. The calculated uniformity and CV for the first film were 4.44% and 1.60%, respectively.

The uniformity for the film on the end of the protons beam path was 2.34% while the calculated CV was 0.80%. As discussed aforementioned, the uniformity describes deviations associated with pixel values, but it can be incorrect if there are unresponsive pixels during the scanning process of the film. The representation of the CV therefore would be indicative of the uniformity of the film. From these results, a small CV was obtained signalling a small fluctuation in the lateral dose deposition.

Ionisation Chamber Measurements - As described previously, only ionisation chambers were used for measurements during this experiment. This was

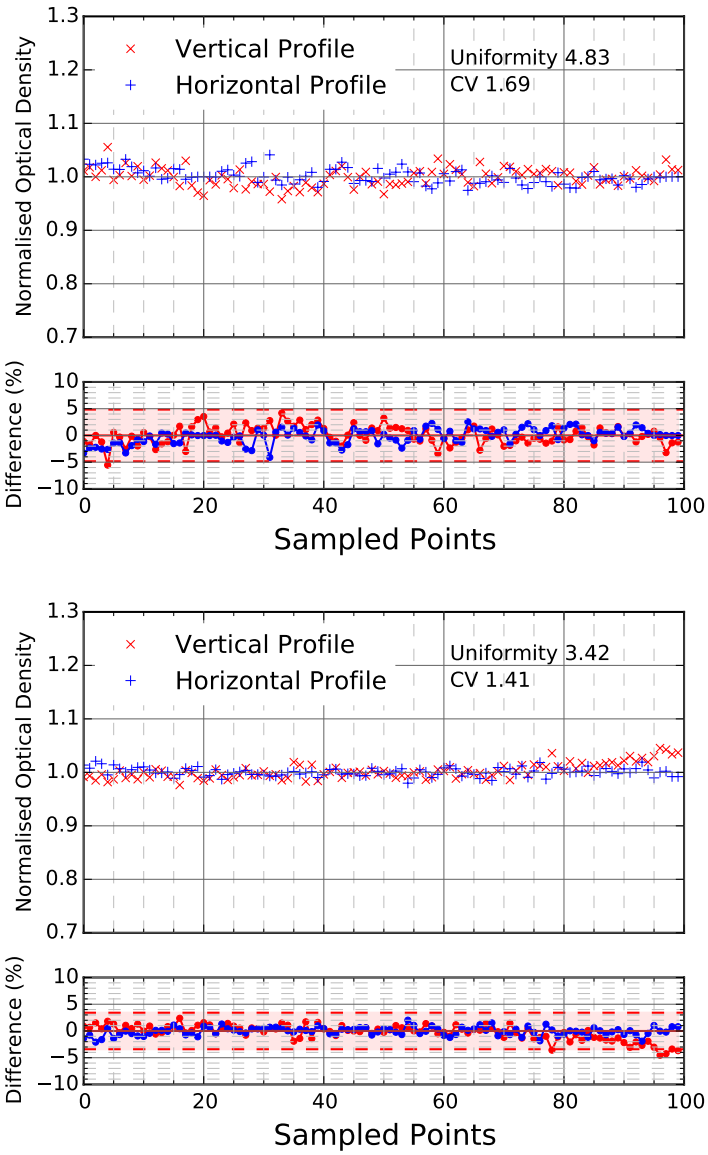

Figure 4.6. Uniformity analysis of the delivered ^{12}C ion beam at a film placed at the beginning (top) and end (bottom) of the beam path. Top - obtained normalised optical density for each pixel value; bottom - calculated deviation. The calculated uniformity has been annotated in the top plot and then expressed as dashed lines in the bottom plot.

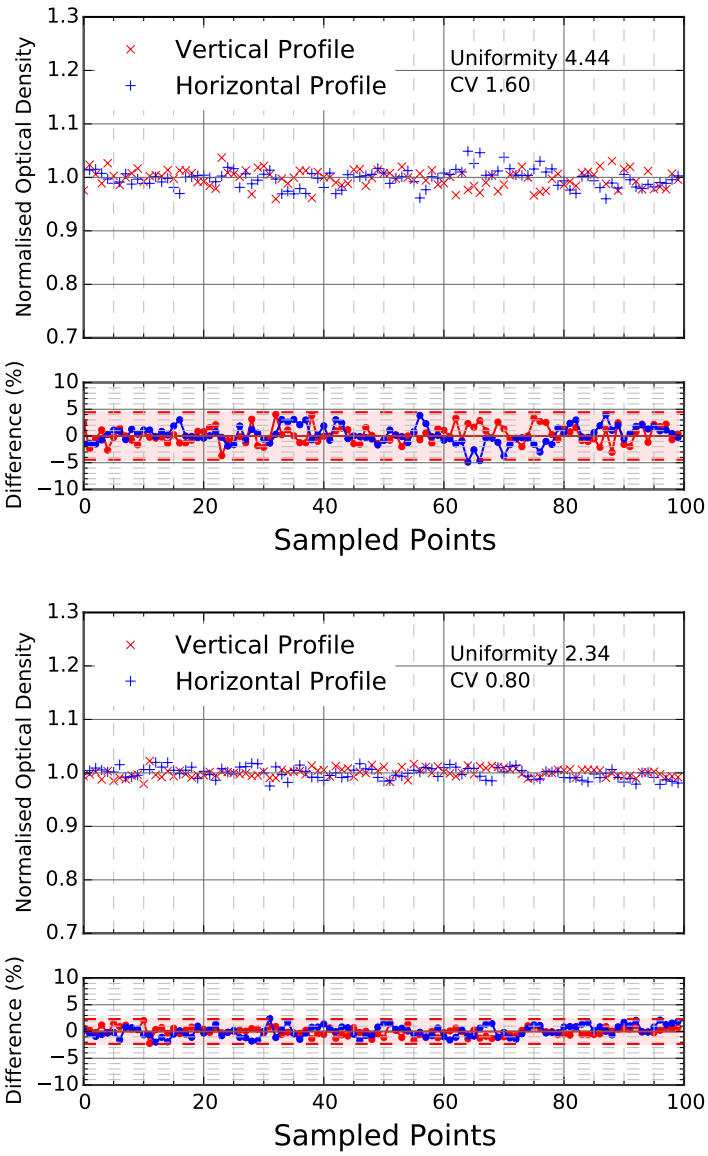

Figure 4.7. Uniformity analysis of the delivered protonbeams at a film placed at the beginning (top) and end (bottom) of the beam path. Top - obtained normalised optical density for each pixel value; bottom - calculated deviation. The calculated uniformity has been annotated in the top plot and then expressed as dashed lines in the bottom plot.

owing to the fact that this experiment served as basis for testing the usability and user-friendliness of the phantom as a biological dosimetric tool. Therefore the HIT's quality assurance procedures were followed (Karger et al. 1999) and, similarly to the experiments conducted at CNAO, the resulting measurements were compared to the dose calculation, in this case MC simulations (Table 4.4).

Table 4.4. Obtained dose deviations from measurements for each beam type.

	Dose (Gy)	Average (%)	Std. Dev. (%)	Max (%)
^{12}C	$1.0Gy$	1.91	1.32	4.4
	$2.0Gy$	1.92	1.25	3.6
	$4.0Gy$	1.97	1.59	4.65
^{1}P	$1.0Gy$	1.16	0.91	2.4
	$2.0Gy$	1.05	0.85	2.35
	$4.0Gy$	1.05	0.76	2.25

In a similar manner to the aforementioned experiments conducted at CNAO, these results fell well within QA acceptance levels of 5%, which consequently helped to obtain a good agreement with detector measurements and ensured cell survival. This allowed for a full dosimetric assessment (Desrosiers et al. 2013) and beam characterisation with dose calculating tools to be performed.

Experiment 3 at HIT - Evaluation of a Full Radiobiological Experiment including Reduced Irradiation Target along the SOBP and Improved Uniformity.

Film Measurement - An analysis of the uniformity of the delivered beam was conducted at only one depth (z = 0.95 cm) using radiochromic films. The choice of analysing only one depth in comparison to the two depth approach used at previous experiments was due to the length of the SOBP. During this experiment, the SOBP covered solely the central part of the cell compartment and a film at the end of the cell compartment would not detect anything. In this experiment, films could only be placed before and/or after cell compartment due to the presence of the cell container. As previously described for the other experiments, the normalised optical density for each pixel value (top) and the calculated difference (bottom) are calculated and plotted from each of these films. The top plot also displays the uniformity and the coefficient of variance that were calculated as per Equations 4.3 and 4.4. This uniformity in then expressed in the bottom plot as dashed lines.

Figure 4.8 shows the obtained results for both the carbon ions (left) and protons (right) irradiations films used. The optical density was obtained by using two profiles along two orientations represented by the blue (horizontal profile) and red (vertical profile) lines. The calculated uniformity and CV was 2.13% and 0.92% and 2.18% and 0.87%, respectively for carbon ions and proton.

Ionisation Chamber Measurements - As described previously, the ionisation measurements were compared to the dose calculation, in this case MC simulations. Table 4.5 shows the obtained dose deviation for each irradiation plan.

Table 4.5. Obtained deviations from measurements for each beam type.

	Dose (Gy)	Average (%)	Std. Dev. (%)	Max (%)
^{12}C	$1.0Gy$	2.33	0.94	4.70
	$1.5Gy$	2.35	0.98	4.47
	$2.0Gy$	2.35	0.96	4.35
	$4.0Gy$	2.39	1.22	4.25
^{1}P	$1.0Gy$	1.54	1.40	4.09
	$1.5Gy$	1.57	1.45	4.27
	$2.0Gy$	1.49	1.46	4.25
	$4.0Gy$	1.57	1.36	3.83

These results for this new plan also fell well within QA acceptance levels of 5%, which consequently helped to obtain a good agreement with detector measurements and ensured cell survival. The average deviation was below 2% for both ion types and all irradiation plans.

4.5 Discussion

The work applied in this thesis describes the importance of improved dosimetry for radiobiological experiments. In this chapter the different contributions and limitations to the physical measurements of the dose were discussed along with the relevant implications in radiobiological experiments. The viability study

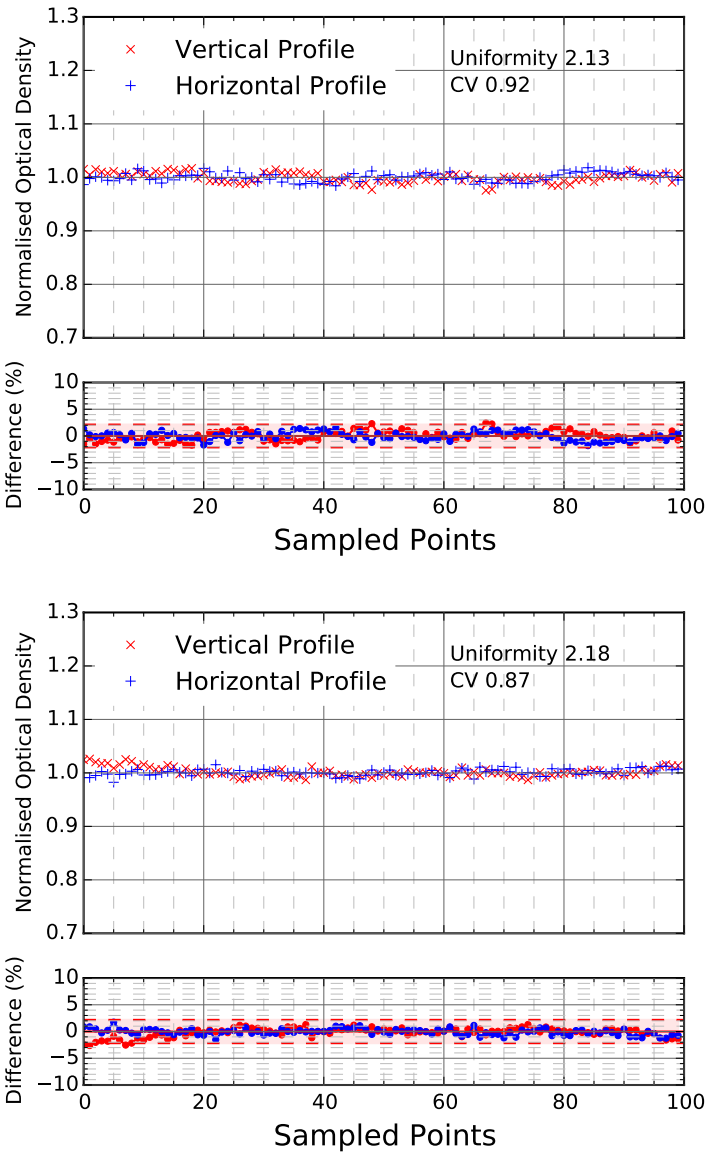

Figure 4.8. Uniformity analysis of the delivered carbon (top) and proton (bottom) ion beams at a film placed at the beginning of the beam path. Top - obtained normalised optical density for each pixel value; bottom - calculated deviation. The calculated uniformity has been annotated in the top plot and then expressed as dashed lines in the bottom plot.

of the phantom for biological assessments is covered in the next chapter. In Chapter 2, the necessity for an improved design was introduced. It was found that in order to reduce uncertainties associated with radiobiological experiments the following steps must be taken:

- Improved dosimetry during cell culture irradiation; and

- Reduced introduction of additional biological uncertainties either by not disturbing the beam path in order to perform these needed dosimetry or by performing in-house sterilisation of tools in contact with cells and uncertainties with batch effect.

The novelty of this phantom is the ability to account for these points in its design conception, in addition to being user-friendly and easily transportable. Concerning the dosimetric limitations of current design, a recent review (Desrosiers et al. 2013) identified dosimetry, or the lack of it, as the main concern for the reliability of radiobiological experiments. The authors were mainly concerned with animal work but the same can be said about cell irradiations. This improvement in dosimetry is even more important in the field of scanned particle beams where uncertainties associated with the physical and biological properties of the ion beam and modern delivery techniques are challenges for the delivery of the correct dose (Carabe et al. 2012; Paganetti 2012).

A weakness of the phantom is the fact that a relative big volume must be irradiated in order to obtain uniform dose along the cell compartment and detectors which results in increased irradiation time.

The experiments at CNAO and HIT showed that a good agreement is obtained between dose calculation and ionisation measurements even when varying the dose distribution by delivering a less uniform irradiation plan, and thereby reducing the irradiation time. This agreement was evaluated at different uniformity levels during the experiments and ranged from 2.30 and 1.70 % for protons and carbon irradiation respectively, during the first experiment in CNAO, to 4.44 and 4.83 and 2.18 and 2.13 % for protons and carbon for the second and third experiment, respectively.

Figure 4.9 describes the aims of the different experiments and highlights some of the obtained results and next steps.

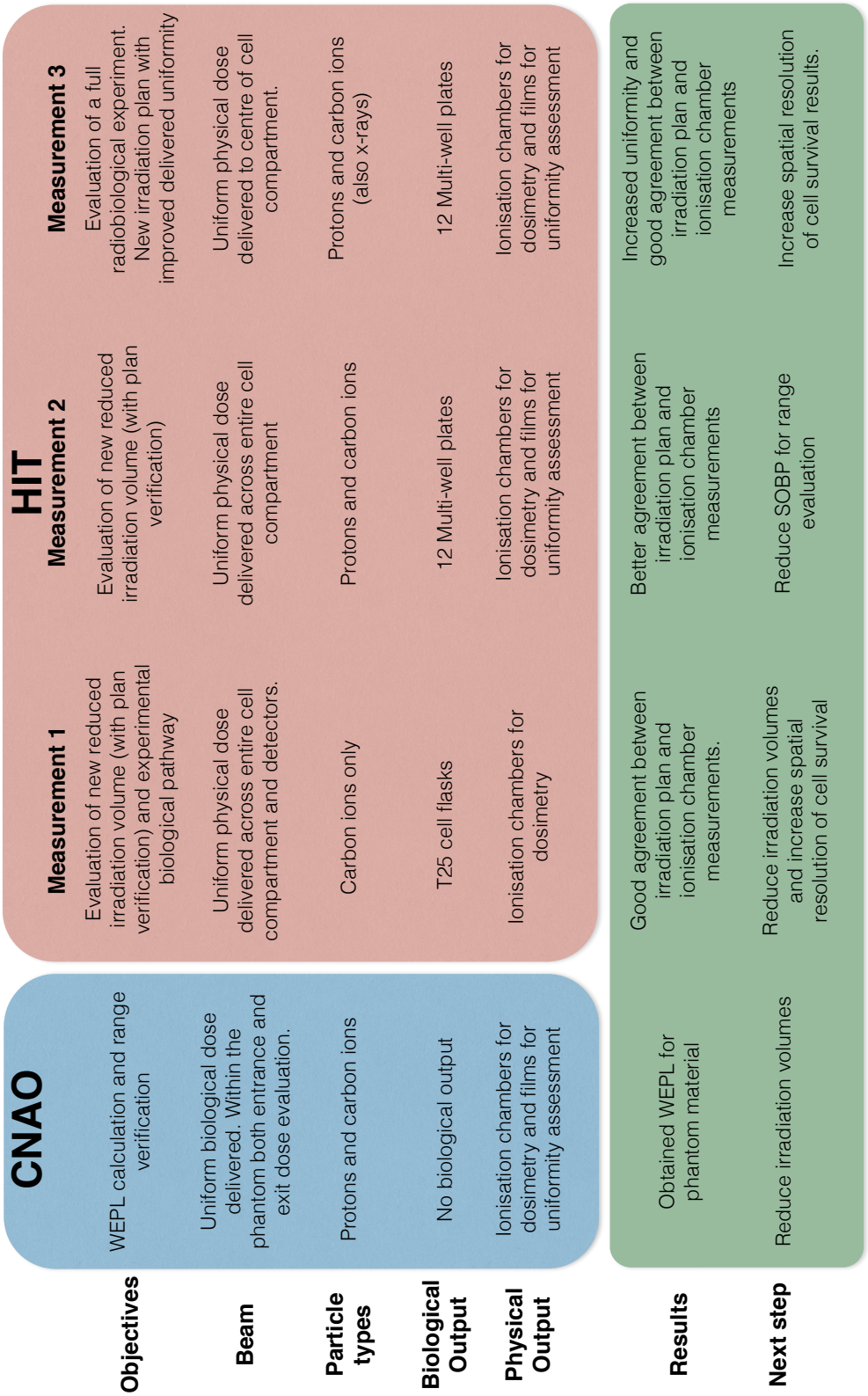

Figure 4.9. An overview of the characteristics of different experiments performed with the phantom including some of the obtained results and next steps.

The aim of the experiment performed at CNAO was to obtain the WEPL so

as to correctly account for the material description in the dose calculations. The results obtained demonstrated that a good agreement was obtained between dose measurements and MC simulations. Each irradiation facility required re-validation of dose calculation tools in order to correctly simulate the dose distribution. Since the phantom material was kept the same, the re-validation was only in respect of the dose delivery system.

During the first experiment at HIT, this re-validation was tackled and a good agreement was obtained with an average deviation in the order of 2.16%. Before the second experiment at HIT, the phantom was modified in order to be able to accommodate extra radiobiological commercial tools for improved spatial resolution in the cell survival results. Initially, T25 cell flasks were used and after the modification the phantom was capable of accommodating multi-well plates. The multi-well plates enable the survival analysis to be conducted at different positions, thereby increasing the spatial resolution of the cell survival results. Due to the increased length of the cell compartment, the irradiation plan was modified. With this new irradiation plan, a good agreement was still obtained at the second experiment at HIT this time with both ion types (the worst mean deviation between ionisation chambers and dose calculations were 1.16 and 1.97 % for protons and carbon ions, respectively). This demonstrates that the irradiation plan was ready to be used in the full radiobiological experiment.

During the last irradiation experiment at HIT, the agreement between measurement and dose distribution modelling was still within acceptable values. As discussed by Ableitinger et al. 2013, for scanned ion beams there are no established criteria for agreement between measurements and calculations and, as the authors suggest, the most reasonable analysis of these criteria was performed by Jaekel et al. 2000. According to these recommendations, the mean value of deviations between measured and calculated doses should be less than 3%, while the maximum deviation should be less than 5% for a target volume in a homogeneous medium.

The mean deviations from the irradiations performed are given in Table

4.2 to Table 4.5, and are in compliance with these proposed criteria. However, since the phantom is not completely homogeneous, nor the irradiation plan completely uniform, the criteria regarding the maximum deviation was not always achieved. During the first irradiation performed at HIT for carbon ion beams one measurement at both 0.5 and 1.0 Gy exceeded this maximum deviation criteria, 5%. During the second and third experiments at HIT, a higher uniformity setting was selected during irradiation plan calculation steps and compliance with this criteria was also achieved. Another weakness of these irradiations are that the irradiation plan calculations were performed with the TPS and these dose calculation algorithms are noticeable limited in calculating dose deposition in non-homogeneous targets. However, the phantom was designed with this limitation in mind and the results showed a good agreement at different positions along the beam path.

Although the influence of dose modelling by MC simulation uncertainties cannot be ignored, the biggest limitations for the irradiation plans used lay with the measurements in addition to the inhomogeneities within the irradiation target. I previously demonstrated that MC simulation is capable of reproducing the reference experimental conditions (Figure 3.4) at a high precision.

During all comparisons of the irradiation experiments in this thesis, the gold standard was considered to be the ionisation chambers results, but this could also be considered a possible limiting factor since these detectors are not capable of correctly measuring dose in high gradient regions due to the lack of charged particle equilibrium conditions in some regions. This would explain deviations between the calculated and measured absorbed dose (Sanchez-Doblado et al. 2007). This was visible, in the exit dose regions for example. Figure 4.5 showed poor agreement is obtained for the last ionisation chamber positions (10 and 11). Overall, as previously discussed, a good agreement between measurement and dose calculation was achieved. The same behaviour of poor agreement at some dose points were also observed for the last two experiments performed at HIT where the maximum deviation was found to be on the detectors in low gradient regions. Another limiting factor was the dose calculation performed

by MC simulations. I was able to show that in most cases, the MC simulation presented precision level beyond the accuracy of the experimental measurements (within ± 3% mean deviation and ± 5% maximum deviation for 90% of the irradiations).

In the previous chapter, I demonstrated that with this phantom design I was able to improve dosimetric recording in comparison to all other set-ups described in Chapter 2, either by not introducing uncertainties in the dose deposition in the cell compartment region, or by correctly evaluating the dose profile which in certain cases could amount to 2.5% (Molinelli et al. 2013). The aim of this chapter was to validate the irradiation plan at different stages by analysing the dosimetric output of the phantom. By doing so, I was able to validate the dose calculation for the whole target area of the phantom so as to correctly report the irradiation dose applied to the cell compartment. This enabled me to study cell survival at the cell compartment with improved dosimetric information on the irradiation beam. By using MC simulations I was able to evaluate different physical and biological outputs such as LET and biological dose.

By using validated MC simulations of the irradiation plan, the phantom was able to report the deposited dose to the cell compartment with a higher confidence level than the ones reported (when reported) in other experiments (Combs et al. 2012; Elsaesser et al. 2010; Bert et al. 2010; Mitaroff et al. 1998; Barazzuol et al. 2012).

The next chapters will go on to discuss the biological evaluation of the phantom, its performance in a radiobioloigcal experiment, including RBE reporting, and the future steps.

4.6 Conclusions

The results presented in this chapter demonstrate that a good agreement between the irradiation plans and measurements is obtained (within ± 3% mean deviation and ± 5% maximum deviation for 90% of the irradiations).

This enabled the MC dose calculation to be benchmarked at these different irradiation plans. With this information, cell survival could be correlated and evaluated with other physical and biological outputs obtained by the MC simulations for the cell compartment.

These results showed that the proposed phantom is able to correlate the calculated dose at specific points calculated by the MC simulation with the measurements and therefore is able to improve dosimetric reporting in the cell compartment, especially for cases where no information is provided or certain uncertainties are not considered. The phantom therefore has been shown to improve dose reporting and reliability in radiobiological experiments. The level of confidence in the reported dose can be thus improved by optimising the beam uniformity.

Chapter 5

Biologic Measurements of Photon and Hadron Beams

5.1 Aim

The aim of this chapter is to evaluate the use of the phantom in assessing the biological response of one cell line for different radiation types. In general owing to the chosen irradiation orientation of the phantom, the radiobiological results were evaluated for the LET and dose parameters in terms of cell survival. In the case of the work contained in this thesis, the contribution of the dose and LET to cell survival is paramount. As well as being able to evaluate multiple parameters by accommodating commercially available cell chambers. This latter feature enables simultaneous irradiation of multiple cell cultures, prepared in the same conditions, thereby reducing the biological variability that would otherwise occur if these experiments were spread over several days.

In the previous chapter, it was shown that thanks to the dosimetric reporting of the phantom, I was able to correlate the dose calculation obtained from MC simulations to the ionisation measurements within 3%. The uncertainty was lower than that of the ionisation chamber for proton and carbon ions. With this information about dosimetry across the phantom alongside the proposed statistical reporting method, cell survival and different parameters of

the phantom could be evaluated in radiobiological experiments.

The main objective of this chapter therefore is to evaluate the behaviour of the cell survival results obtained by the phantom in radiobiological experiments with respect to RBE and LET.

5.2 Introduction

The success or failure of a treatment is characterised by the relationship between the Tumour Control Probability (TCP - the chance of overcoming the disease), and the Normal Tissue Complication Probability (NTCP - the chance of complications arising in normal tissues arising from the amount of side effects the treatment is conferring). Therefore, in order to improve treatment efficacy, either the TCP needs to be increased and / or the NTCP needs to be reduced. This can mainly be achieved by either improving:

- Physical parameters of the treatment, for example by improving the dose delivery conformity (Jones et al. 2009; Durante 2014); or
- Biological parameters (properties) of the tissues, for example by improving oxygenation (Tinganelli et al. 2013) in order to increase radiosensitivity of hypoxic tumours cells.

In a recent publication (Wera et al. 2013), the authors showed that LET variations are present within the tumour volume due to continuous energy loss along the proton track, and therefore, the associated RBE may be higher or lower than the standard 1.10. This constant RBE value is currently used clinically in the TPS and it is supported by international guidelines (ICRU 2007). This problem of evaluating the effectiveness of ions (including protons) is not limited only to quantifying LET, but also to understanding that different radiation qualities may also differ in the type of induced biological damage caused (Niemantsverdriet et al. 2012). All these issues raise the need for further cell irradiation experiments with different cell lines and different end points.

The review described in Chapter 2 showed that, in order to improve our knowledge of enhanced radiobiological effectiveness, which is necessary to support clinical proton and ion beam applications, more dedicated tools need to be developed. The main characteristic pursued for the phantom was the ability to have both physical and biological measurements in a device which is transportable and has lower complexity for usage and analysis of results. The phantom aims to facilitate high-throughput data acquisition from biological samples prepared in the desired experimental setting. This ability to perform multiple irradiations in the smallest amount of time is important biologically (to reduce possible biological differences (Leek et al. 2010)), but also logistically as indicated by a recent review (Abler 2012) which showed that there is a significant lack of beam time availability for radiobiological research with ion beams including protons.

The following section aims to show that the phantom is capable of evaluating biological response in relation to both dose and LET in a manner relevant to clinical treatments, as suggested by Paganetti 2014; Jones 2015a; Jones 2015b. Such a phantom also allows for evaluation of different biological end points in simpler radiobiological experiments.

5.3 Methods

Cells were irradiated with ions (protons and carbon ions) at HIT and with 6MV X-rays (photons) at the German Cancer Research Centre or Deutsches Krebsforschungszentrum (DKFZ) (experiment 2 and 3 at HIT described in previous chapter). DKFZ is a national research centre located in Heidelberg with research focused on cell biology and tumour biology; structural and functional genomics; cancer risk factors and prevention; tumour immunology; imaging and radiobiology; infection and cancer, and translational cancer research. HIT is a hospital-based ion beam therapy facility which is connected to the neighbouring clinical departments of the Heidelberg University Hospital.

I carried out the work for all the experiments (during all stages from imaging,

planning and irradiation) and analysis of the dosimetry. For the biological steps (seeding, plating and counting) assistance and equipment(incubator, flasks, pipette and cell medium) excluding the multi-well plates were provided by the Dr. Dokic. Once the cell survival was obtained, I perform all curve fittings and data analysis of the different biological assays.

In this thesis, the cell line A549, a human Non-Small-Cell-Lung-Carcinoma (NSCLC) cell line, was irradiated at different experiments. Despite the improvements in conventional radiotherapy, overall survival for advanced stages of lung cancer is still small (in the region of 15%). Wink 2014 has suggested that the limiting factor to dose escalation, and therefore better tumour control probability, is the proximity for healthy tissues at risk (lung, heart, mediastinal structures, spinal cord) and that the improved conformity achieved with particle therapy (protons, carbon, etc.) makes these techniques an option worthy of investigating. In addition, the treatment of more challenging tumours like lung carcinomas, which can prove difficult to target owing to movement, is seen as the next step in obtaining recognition for modalities of high precision delivery such as particle therapy (Bert et al. 2010; Riboldi et al. 2012). These factors influenced the availability of this cell line in the radiobiological laboratory used for the cell preparation and analysis in my thesis.

The dosimetric information of each experiment has been previously described in detail in the previous chapter (Chapter 4). The main differences between irradiations were the shortened SOBP during the second experiment in respect to the first (12 vs 5 cm). This was done by reducing the energy range between experiments (energy range from 88.8 to 272.8 MeV per nucleon for the first experiment for carbon ions and 88.8 to 216.0 MeV/u for the second experiment). At both experiments, dose deposition was obtained with ionisation chambers and compared with Monte Carlo simulations. Cells were prepared and irradiated at two independent experiments. The first experiment served as preparation for the second experiment in terms of optimising cell seeding (Section 5.3.1), where the same preparation and analysis were used. In addition, at both ion irradiations a target volume as described in Section 4.3.4 was irradiated with

a uniform physical dose. During a second experiment, in addition to the ions irradiations at HIT, X-ray irradiation was performed at DKFZ as a baseline for subsequent RBE calculations. The experimental pathway is described in Figure 5.1 below.

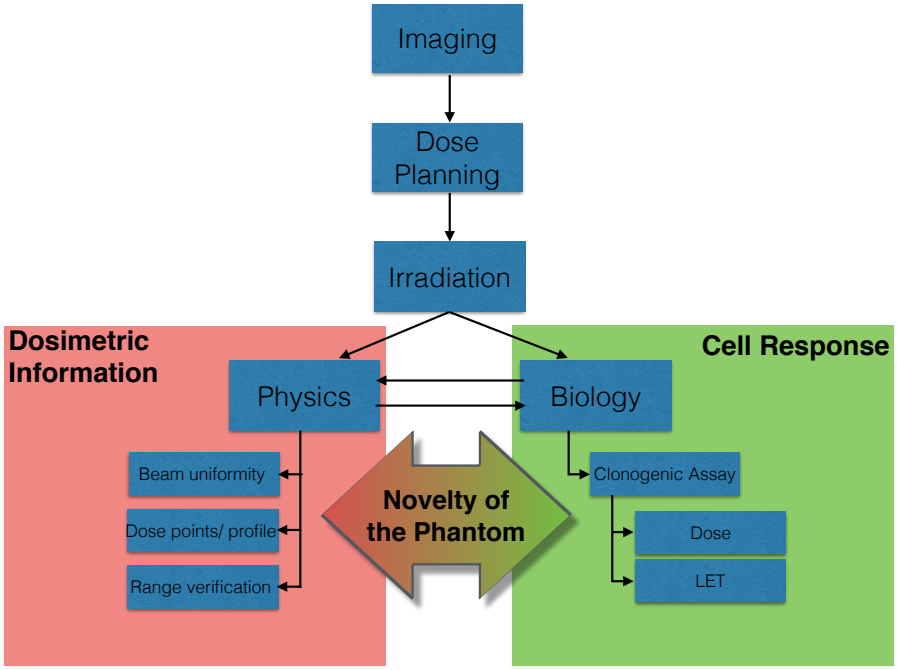

Figure 5.1. Schematic Representation of Experimental Pathway. The novelty of the phantom is the possibility to correlate different physical attributes to biological responses in simpler set-ups.

As previously discussed in Section 4.3.3 the phantom followed the patient protocol of both locations. Firstly, it was imaged (CT) and had external surrogates placed for reference localisation when irradiating. The images with localisers were than transferred to the TPS where different irradiation plans were calculated for the different dose points and particle type. The calculated irradiation profiles were transferred to the respective accelerators and irradiation was conducted. Irradiation plans for all ion experiments were carried out by the CE-marked *syngo*® RT Planning by Siemens AG Healthcare (Erlangen, Germany) and the CE-marked *RayStation*® 4.5 system by RaySearch Laboratories AB (Stockholm, Sweden) at DKFZ.

For each irradiation, dose deposition information was acquired for the different detector positions and cell survival analysis was performed. The novelty

of this phantom design is its ability to obtain both dosimetric (beam uniformity, dose points or profile and range verification) and biological (clonogenic assay and multivariate correlations for example RBE-LET-Cell survival) information during the irradiation and, by doing so, it is able to facilitate radiobiological experiments.

5.3.1 Cell Preparation

Human A549 cells were grown in complete growth medium (cDMEM) containing 10% Foetal Bovine Serum (FBS). For these experiments, commercially available multi-well plates were labelled in preparation for setting up each plate with a known number of cells depending on the radiation dose given. Seeding densities for different delivered dose points are presented in Table 5.1.

The different cell seeding was chosen so that after irradiation a reasonable number of surviving colonies could be observed, on the understanding that if a standard deviation should be in the order of 10%, the number of surviving colonies minus 10% would be greater than zero. It was chosen empirically as it has shown that those numbers will give sufficient countable number of colonies (enough to be seen by eye, also to decrease the deviations, and not to have them too many since they would start fusing one with another and we could not distinguish them) where the goal is to have similar number for counting for each sample (dose). The numbers are also dish-dependent (smaller wells less cells to avoid fusion, but to have still enough cells for counting also at high dose where we kill a lot). It was noted that the cell seeding between experiments was reduced. This was due to the number of large clustered colonies found in the first experiment. A balance was therefore struck on the second experiment between having enough cells to produce a reasonable number of colonies and having too many cells to avoid clustering of colonies which introduce uncertainties in colony counting. A threshold of 50 cells per colonies was used in this thesis and colonies containing below that number of cells were not counted.

Before irradiation, the cell medium was removed, and the cells were briefly rinsed with 0.25% (w/v) Trypsin- 0.53 mM EDTA solution to remove all traces of serum that contains trypsin inhibitor, and this solution was extracted. New Trypsin-EDTA solution was added to the flask in order to detach and disperse the cell layer. Once this was verified by visual inspection on a microscope, complete growth medium was added and cells were aspirated by gently pipetting. Cells were counted with a Neubauer chamber and appropriate aliquots of the cell suspension were transferred to multi-well plates. Once the correct seeding ration was obtained, the different cell densities were placed in their respective plate. The plates were then placed in a 37°C incubator set at 5% carbon dioxide (CO_2) to allow the cells to settle and attach as a mono-layer prior to irradiation.

Table 5.1. Cell seeding - Number of cells used in irradiation experiments.

	Carbon Ions Exp 1 - Exp2	Proton Ions Exp 1 - Exp 2	X-rays Exp 1 - Exp 2
0 Gy (Control)	100 - 100	*	n/a - *
1.0 Gy	400 - 200	400 - 100	n/a - 100
1.5 Gy	n/a - 200	n/a - 100	n/a - n/a
2.0 Gy	400 - 200	400 - 200	n/a - 100
3.0 Gy	n/a - n/a	n/a - n/a	n/a - 100
4.0 Gy	1000 - 400	1000 - 200	n/a - 200
6.0 Gy	n/a - n/a	n/a - n/a	n/a - 400
8.0 Gy	n/a - n/a	n/a - n/a	n/a - 400

* - same control was used for all cell irradiation in the same experiment.
n/a - not applicable, or not used.

5.3.2 Cell Analysis

Cells were seeded in 10% FBS/cDMEM in 12-well plates and irradiated 24 hours later, followed by a 7-10 days' incubation. Clonogenic assay (Franken et al. 2006) was performed to assess the biological response from the irradiated dose. The number of visible colonies was manually counted after being fixed with 75% methanol and 25% acetic acid for 10 minutes at room temperature and stained with 0.1% crystal violet for 15 minutes.

The plating efficiency (PE) was obtained from the control (uniniradiated) sample (Equation 5.1), and surviving fractions (SF) calculated using this information from the number of surviving colonies in irradiated samples and the PE (Equation 5.2).

$$PE = \frac{N_c}{N_p} \text{ x } 100\ \% \tag{5.1}$$

$$SF = \frac{N_c}{N_p \text{ x PE}} \% \tag{5.2}$$

Where N_c and N_p correspond to number of counted colonies and number of plated cells respectively.

The survival curve was obtained from three different wells, which corresponds to three survival values per dose as shown in Figure 5.2 below. Errors were evaluated as standard deviations. Mock irradiated cells were used as a control.

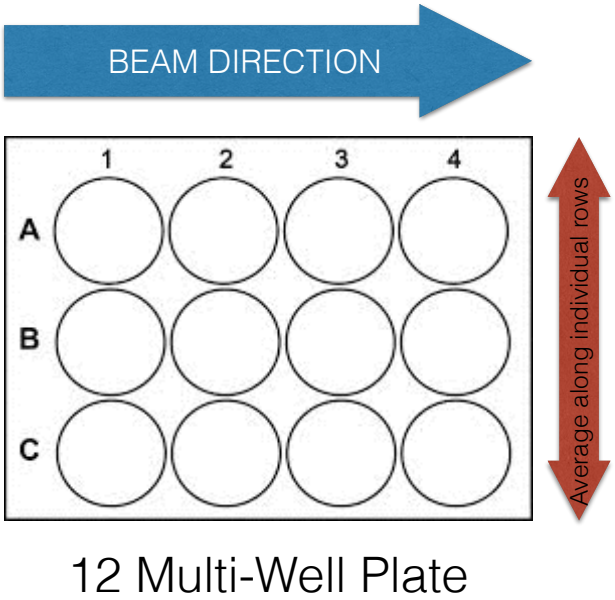

Figure 5.2. Multi Well Plate Irradiation Diagram. Each row (1,2,3 and 4) represents one dose point and cell survival was obtained from three different wells (A, B and C). Errors were evaluated as standard deviations.

5.3.3 Irradiations

The previous prepared multi-well plates (Section 5.3.1) were placed in front of the beam-eye view inside of the phantom. The irradiation field is centred at the isocenter. The full details of the dosimetry used in the ion irradiations are described in the previous chapter (Section 4.3.4). The relevant information for this chapter has been included below. In addition to the ion irradiations, during the second experiment at HIT, some cells were separately irradiated with X-rays. The details of this irradiation are described in the following sections and Figure 5.3 summarises the outline of these experiments. A graphical description of the phantom and beam orientation is found in Appendix A.

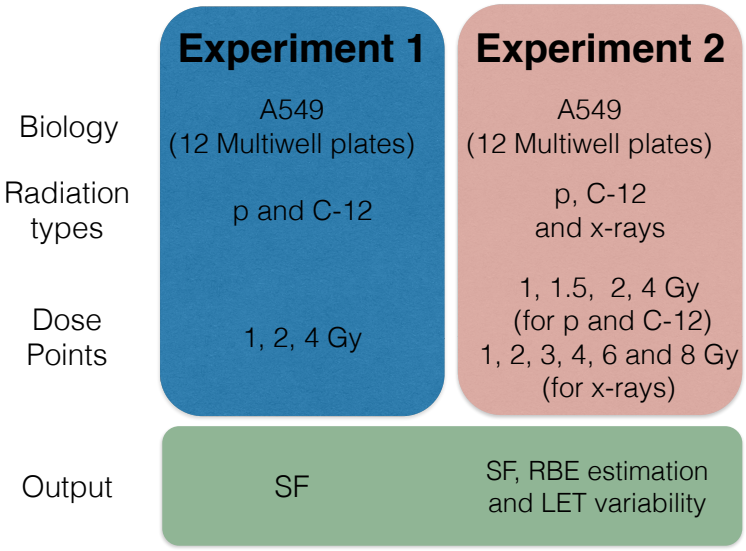

Figure 5.3. Outline of biological experiments. The main difference between the experiments is that during the second experiment as X-ray survival was also obtained, RBE and possible correlations between RBE-SF-LET were evaluated.

Experiment 1 - Evaluation of Biological Set-up.

As aforementioned, an initial experiment was conducted at HIT so as to evaluate the experimental set-up. During this experiment the cell response was evaluated for both carbon and proton ions. A uniform physical dose along the SOBP with delivered doses of 1.0, 2.0 and 4.0 Gy was used. During this experiment the whole multi-well plate was irradiated with the same dose. The complete

irradiation plan and dosimetry information are described at Section 4.3.4.

Experiment 2 - Viability Study of the Phantom for Radiobiological Experiments.

Experiment 2 was performed at two different centres: DKFZ due to its availability to a clinical X-ray linear accelerator and HIT where ion beam irradiation take place.

DKFZ At the DKFZ, a Siemens medical linear accelerator (or Linac) was used. One irradiation plan was created for a selected dose and the subsequent plans for the different doses were obtained by scaling the delivered monitor units to the reference point. For the X-ray measurements, a 6 MV photon beam was used. In total 6 dose points were performed (1.0, 2.0, 3.0, 4.0, 6.0 and 8.0 Gy) for a field of 10 cm by 10 cm. The reference point was placed in one of the multi-well rows, and the surviving fraction were used from the results of this specific row. The irradiation beam was oriented horizontally to the cell culture plate as shown in Figure 5.4. The 97%-105% dose was positioned along the second row of the multi-well plate.

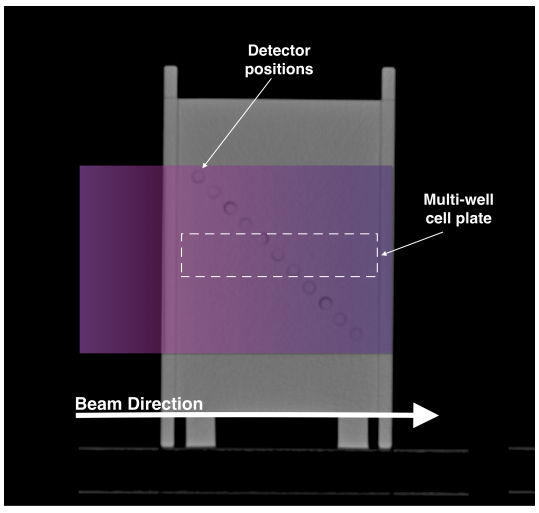

Figure 5.4. Beam orientation by the irradiation plans at DKFZ measurements. Proposed orientation used by ion irradiations where the cell plate is positioned horizontally to the beam direction.

Two different dosimeters have been used in the phantom during this experiment: films and an ionisation chamber. GafChromic films were placed before and after the cell plate and the ionisation chambers were located at the mid point of the plate in relation to the depth, which corresponds to the reference point used by the TPS for the preparation of the irradiation plan. PMMA inserts were also used to avoid inhomogeneities along the beam path.

HIT During this second irradiation at HIT, similar to the previous experiments, different dose points for both carbon and proton ions were used to evaluate the cell response. During this experiment, a uniform physical dose along the selected section of the SOBP with delivered doses of 1.0, 1.5, 2.0 and 4.0 Gy was used. An extra dose point (1.5 Gy) was selected, in addition to the doses used during previous experiment, since the results obtained previously showed a possible curvature of the fitted survival curve that was could not be fully measured in the region between 1.0 and 2.0 Gy. This extra dose point further reduced uncertainties in the fitting.

As shown in Table 5.1, the seeding was reduced in order to compensate for the cell growth owing to the waiting time for cell counting. In addition, the two middle rows of the multi-well plate were irradiated with the same dose. The first and last row received the entrance dose and the exit dose respectively. The complete irradiation plan and dosimetry information are described at Section 4.3.4. The reason for choosing this reduced SOBP was to evaluate if the procedure of the irradiation plan and dose delivery was able to correct correlate different cell survival at different delivered doses per cell plate.

5.3.4 Dosimetry and Beam Characterisation

The evaluation of the dosimetry and beam characterisation in the cell compartment was carried out after the irradiation using either MC simulations or TPS as previously described (see Section 3.2.1). FLUKA is capable of simulating both ions and X-rays, but for the purpose of this thesis only ions have been simulated. For X-rays, the dose calculation done by the TPS was used. Ioni-

sation chambers, or other chosen detectors, allow for verification of the dose distribution (in relation to beam range and dose deposition) and subsequently assist with MC simulation benchmarking. The obtained correlation between dose modelling (via MC) and measurement were within the limitations of the detector (below 3%).

5.3.5 Data Fitting and RBE Calculation

Calculation of LET-RBE Variability

The statistical approach set forth in Section 2.4.1 was used in order to obtain the new optimised α and β parameters and RBE confidence interval.

In addition to the calculation of the clonogenic cell survival subsequently for the viability study, the LET-RBE variability was also investigated. The method previously described by Jones et al. 2006was used.

RBEs were calculated by comparing the single doses in order to obtain an isoeffect:

$$\alpha_L d_L + \beta_L d_L^2 = \alpha_H d_H + \beta_H d_H^2 \tag{5.3}$$

where, L and H are related to low or high LET respectively. Then it is just needed to divide the equation by the d_H. The α and β were obtained by the optimisation of the fitting survival fraction curves.

5.4 Results

5.4.1 Assessment of Cell Survival

Experiment 1 - Evaluation Study

The measured cell survival for carbon ion irradiation in the first experiment is shown in Table 5.2. The survival was obtained from each well for all multi-well plates. From each row, a mean cell count was obtained. Once the plating efficiency was calculated the mean cell survival (μ) and one standard deviation

(σ) were calculated for each row at each delivered dose, with row 1 located at the beginning of the SOBP and row 4 at the end of the SOBP. A reduced survival along the SOBP could be observed.

Table 5.2. Cell survival at HIT measurement for carbon ion beam. Beam direction from row 1 to row 4.

Dose *(results in %)*	1 Gy μ (1 σ)	2 Gy μ (1 σ)	4 Gy μ (1 σ)
Row 1	73.3 (9.1)	45.3 (10.5)	14.4 (6.6)
Row 2	75.6 (16.2)	47.1 (12.6)	10.0 (1.6)
Row 3	72.1 (8.9)	55.2 (14.1)	6.9 (1.4)
Row 4	56.9 (7.1)	46.5 (10.5)	4.7 (2.6)

The same process was repeated for the cells irradiated with proton beams. The results can be found below (Table 5.3). One might notice that for protons a reduced survival is obtained along the SOBP.

Table 5.3. Survival at HIT measurement for proton beam. Beam direction from row 1 to row 4.

Dose *(results in %)*	1 Gy μ (1 σ)	2 Gy μ (1 σ)	4Gy μ (1 σ)
Row 1	108.1 (4.9)	83.1 (14.1)	38.9 (7.4)
Row 2	104.6 (4.9)	69.8 (9.2)	45.5 (0.4)
Row 3	111.6 (6.3)	71.5 (23.4)	41.8 (7.2)
Row 4	98.2 (21.6)	68.0 (6.9)	34.6 (2.6)

By optimising (as described by Equation 2.3) with respect to the cell survival data in Tables 5.2 and 5.3, survival curves for both ion types at different row positions were obtained (Figure 5.5).

Since the absorbed dose in all rows are the same, the observed differences are due to the difference in LET along the beam path. This explains why the cell survival obtained at row 4 is significantly lower than the other rows. The difference between row 3 and row 4 with proton beam is smaller than for the carbon beam because the variation of LET is smaller compared with carbon beam.

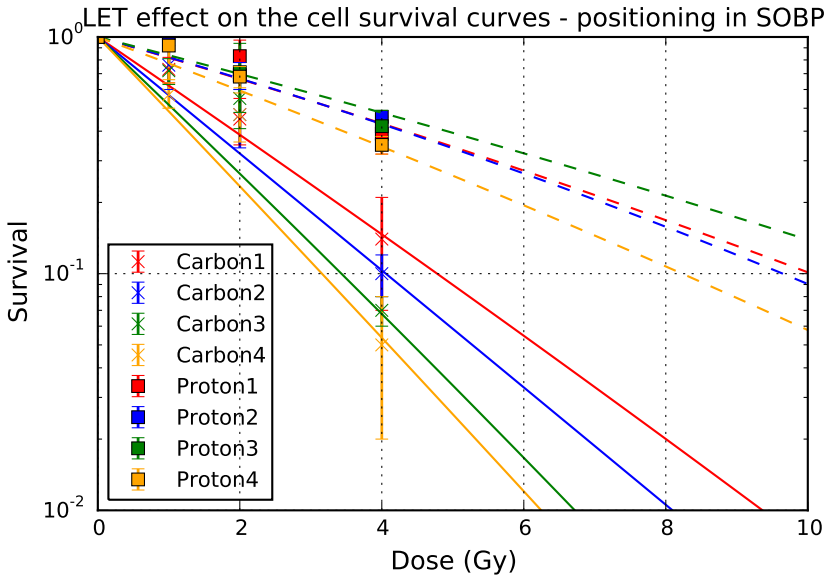

Figure 5.5. Clonogenic cell survival curves at different row positions which are indicated by the number shown in the legend after each particle type. The experiment results are represented (x - carbon cell survival; ■ - protons cell survival).

Experiment 2 - Viability Study of the Phantom for Radiobiological Studies

The procedure of the first experiment was repeated for the second experiment. The carbon cell survival is shown in Table 5.4 and (Table 5.5). Reduced survival can be noted along the SOBP (two central rows).

Table 5.4. Cell survival obtained from measurements for carbon ions beam during second biological experiment at HIT. Beam direction from row 1 to row 4.

Dose *(results in %)*	1.0 Gy μ (1 σ)	1.5 Gy μ (1 σ)	2.0 Gy μ (1 σ)	4.0 Gy μ (1 σ)
Row 1	63.9 (4.2)	58.7 (3.2)	47.9 (5.2)	12.0 (1.6)
Row 2	59.4 (2.8)	50.7 (7.9)	38.2 (3.3)	6.4 (1.8)
Row 3	55.9 (1.2)	48.3 (4.3)	35.1 (1.6)	5.0 (1.6)
Row 4	62.8 (6.3)	59.4 (11.7)	45.1 (2.6)	11.8 (3.3)

Both Tables 5.4 and 5.5 show the mean (μ) survival, taking into account the obtained survival in the control sample by calculating the plating efficiency and one standard deviation (σ). Similar to previous experiment, the cell survival

in row 3 (which in this experiment is the last row fully inside the SOBP) is significantly lower than the other rows. As expected, this effect is more evident in the carbon beam data due to the higher LET variation.

Table 5.5. Cell survival obtained from measurements for protons beam during second biological experiment at HIT. Beam direction from row 1 to row 4.

Dose *(results in %)*	1.0 Gy μ (1 σ)	1.5 Gy μ (1 σ)	2.0 Gy μ (1 σ)	4.0 Gy μ (1 σ)
Row 1	63.2 (1.2)	61.8 (7.9)	50.3 (1.0)	25.7 (3.7)
Row 2	56.3 (6.3)	50.0 (2.1)	40.6 (5.4)	21.9 (2.8)
Row 3	46.5 (4.3)	46.5 (4.3)	38.5 (2.8)	19.4 (1.6)
Row 4	72.2 (3.2)	68.1 (10.5)	51.0 (5.2)	28.5 (1.0)

In addition to the ion irradiations, X-ray survival was also obtained during this experiment(Table 5.6) and this data was used to obtain the fitted curves (Figure 5.6).

For X-rays, radiosensitivity parameters of 0.25 ± 0.06 for α and 0.02 ± 0.01 for β were obtained. For carbon ions only the α parameter was used and the following parameters were obtained: 0.41 ± 0.03, 0.51 ± 0.03, 0.67 ± 0.03 and $0.44 \pm 0.03\ Gy^{-1}$, for row 1, 2, 3 and 4 respectively. And for protons, 0.38 ± 0.03, 0.40 ± 0.09, 0.47 ± 0.05 and $0.32 \pm 0.003\ Gy^{-1}$.

So as to better evaluate the results, the two middle rows of multi-well plates were re-plotted (Figures 5.8 and 5.7). Those rows were chosen owing to the fact they had the largest difference in survival and therefore, if there was evidence

Table 5.6. Cell survival obtained from the irradiation at DKFZ measurements for X-Rays beam.

Dose	Mean Survival (1 Stdev)
1.0 Gy	82.5 (9.1)
2.0 Gy	45.8 (4.0)
3.0 Gy	37.8 (6.9)
4.0 Gy	33.2 (2.0)
6.0 Gy	10.6 (4.7)
8.0 Gy	3.7 (1.3)

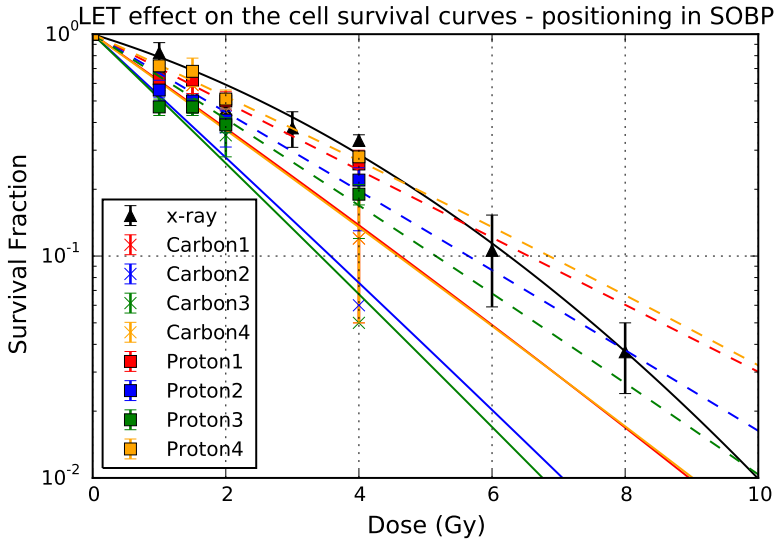

Figure 5.6. Fit of cell survival curves for different radiation types and different row positions. The experiment results have also been plotted (x - carbon cell survival; ■ - protons cell survival; ▲ for X-rays) - Each colour represents a different row. Beam direction from row 1 to row 4.

of the effect of the LET contribution, this is where it would be most evidently noticeable. The calculated fitting with its uncertainties are plotted below.

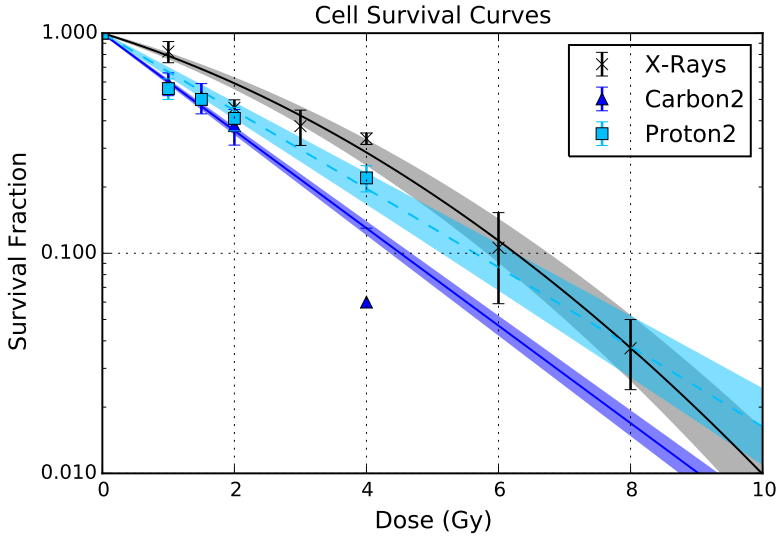

Figure 5.7. Cell survival curves plus survival data for different ion types for row 2. (▲ - carbon cell survival; ■ - protons cell survival; x for X-rays). The blue coloured bands representthe uncertainty of the fitted parameters. Light-blue for protons, dark for carbon and grey for X-rays.

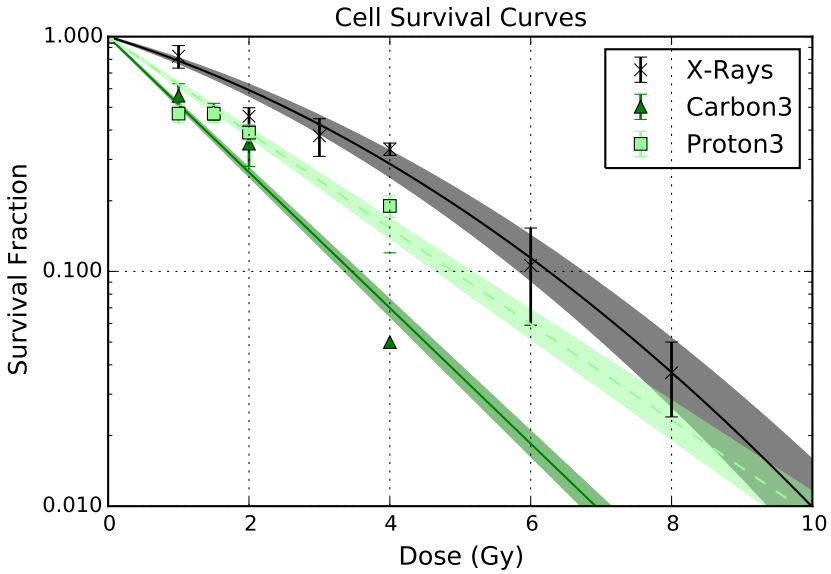

Figure 5.8. Cell survival curves and survival data for different ion types for row 3. (▲ - carbon cell survival; ■ - protons cell survival; x for X-rays). The green coloured bands representthe uncertainty of the fitted parameters. Light-green for protons, dark for carbon and grey for X-rays.

5.4.2 RBE Estimation

The RBE_{20} (RBE at 20% cell survival) for each well was calculated from the fitted parameters.

Figure 5.9 shows the calculated RBE_{20} with its 95 % CI (Equation 2.4) for the complete radiobiological experiment. The obtained RBE_{20} and RBE_{10} are presented in Table 5.7.

Table 5.7. Calculated RBE at Different Survival Fractions.

Dose	RBE_{20} $[95\%CI]$	RBE_{10} $[95\%CI]$
Row 1 12C	1.48 [1.35; 1.63]	1.35 [1.27; 1.45]
Row 2 12C	1.93 [1.66; 2.29]	1.75 [1.57; 1.97]
Row 3 12C	2.02 [1.71; 2.45]	1.83 [1.62; 2.09]
Row 4 12C	1.50 [1.38; 1.63]	1.36 [1.28; 1.45]
Row 1 1H	1.05 [1.01; 1.11]	0.95 [0.92; 0.99]
Row 2 1H	1.22 [1.15; 1.30]	1.11 [1.05; 1.15]
Row 3 1H	1.33 [1.22; 1.46]	1.21 [1.14; 1.29]
Row 4 1H	0.99 [0.95; 1.04]	0.91 [0.88; 0.94]

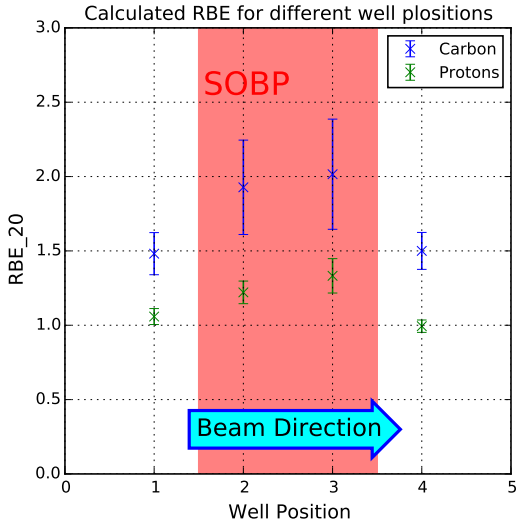

Figure 5.9. Calculated RBE_{20} for the viability study for both protons and carbon ions. The error bars represent the 95% confidence interval and were calculated taking into account biological and dosimetrical uncertainties. The red area represents the positioning of the SOBP along the multi-well plate.

5.4.3 LET-RBE Variability

From the obtained cell survival, the LET-RBE variation was evaluated. The optimised fitted survival curve and its parameters were obtained from the cell survival data. A correlation between RBE and dose was obtained from Equation 5.3. This process was repeated for different LET values.

Figures 5.10 and 5.11 show the obtained LET-RBE-Dose variability for carbon and proton ions respectively.

The RBE must reduce with increasing dose. As expected at near-zero doses, the quadratic dose terms can be neglected and Equation 5.3 becomes:

$$\alpha_L d_L = \alpha_H d_H \tag{5.4}$$

leading to:

$$RBE \rightarrow RBE_{max} = \frac{d_L}{d_H} = \frac{\alpha_H}{\alpha_L} \tag{5.5}$$

Similarly, at exceeding high doses, the quadratic terms dominates:

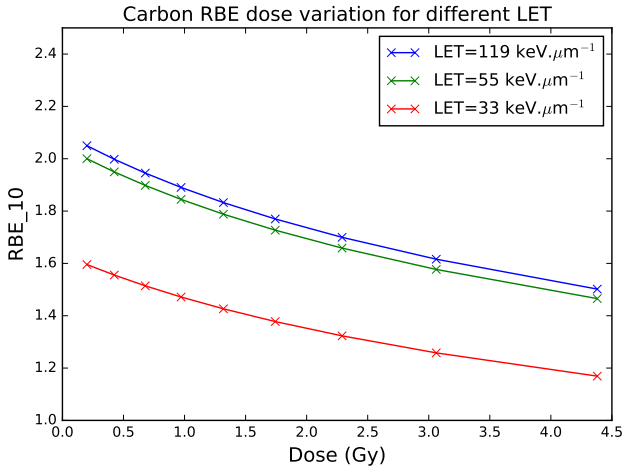

Figure 5.10. Calculated RBE-LET-Dose variability for carbon ions in the phantom viability study.

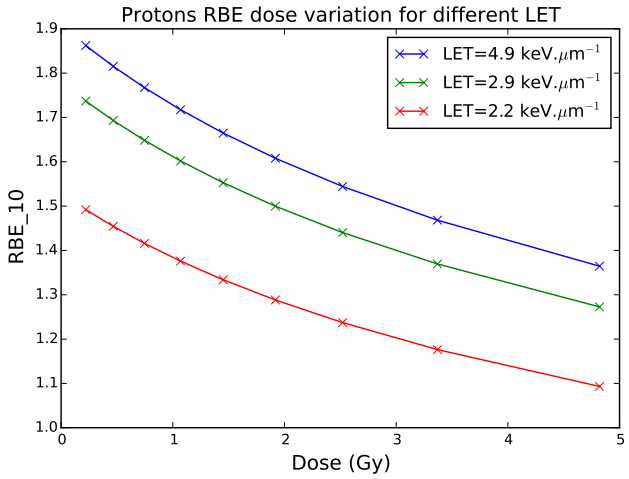

Figure 5.11. Calculated RBE-LET-Dose variability for protons in the phantom viability study.

$$\beta_L d_L^2 = \beta_H d_H^2 \tag{5.6}$$

and:

$$RBE \rightarrow RBE_{min} = \frac{d_L}{d_H} = \sqrt{\frac{\beta_H}{\beta_L}} \tag{5.7}$$

The observed effect is increased with the increase of the LET. Similar behaviour has been discussed in the literature (Jones 2015a; Jones et al. 2009).

5.4.4 Correlation between Physics and Biology

By being able to assess the dose deposition along the phantom (Chapter 4) and the cell survival presented in this chapter, I was able to evaluate the true capability of the phantom. Figure 5.12 correlates the different cell survival obtained in relation to well position and dose deposition.

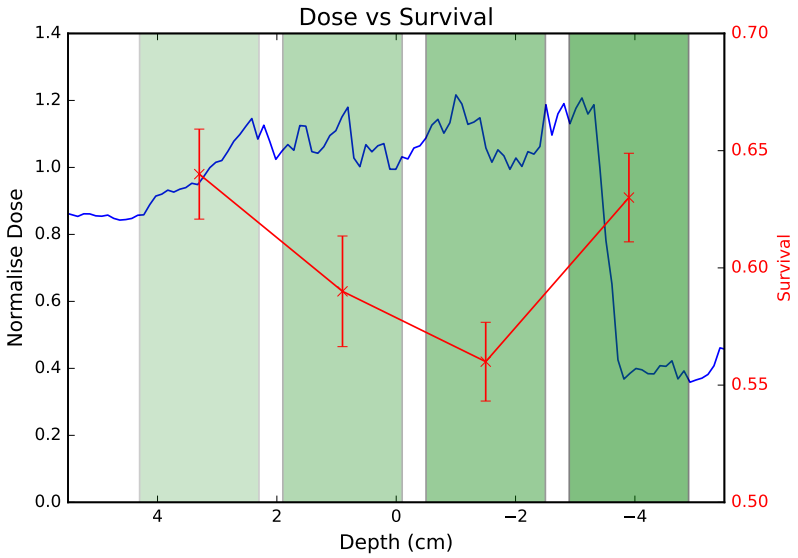

Figure 5.12. Correlation of dose profile and cell survival. Cell survival is placed alongside well position and depth dose profile. Higher dose deposition yields lower survival. The difference in cell survival between position 2 and 3 is due to LET contributions as described before. The different shaded areas represent a different well position.

Cell survival is placed alongside well position and depth dose profile, and, as expected, I found that higher deposited doses yielded lower cell survival. In this figure, it is also possible to note the effect of LET variation, even if not statistically significant, in cell survival between well positions 2 and 3. In the previous section, I compared the effect of the different LET averaging. An overforeseen problem which occurred during these measurements was that, by reducing the SBOP to cover only the second and third wells, no constraint was set for the fourth well leading to the dose not as low as expected. The variation of this dose deposition can also be explained by the statistic set at the MC simulations.

5.5 Discussion

The enhanced biological effects of ion beam therapy using carbon or proton ions has been discussed extensively (Barazzuol et al. 2013; Britten et al. 2013; Combs et al. 2012; Niemantsverdriet et al. 2012; Demizu et al. 2014; Elsaesser et al. 2010; Goodhead 1999; Mitaroff et al. 1998; Paganetti 2014; Scholz 2000; Schulz-Ertner et al. 2007; Tinganelli et al. 2013), but in order for optimal benefits to be achieved, it is imperative to correctly understand the biological effects of irradiation on the treatment outcome and compare it with conventionally used X-rays. This chapter investigated the effects of different radiation types (carbon ions, protons and X-rays) for a specific human cell line (NSCLC A549) through the evaluation of clonogenic cell survivals. The proposed set-up used in this work is different from the ones found in the literature since, in this instance, a more clinical approach was adopted. By the phrase a more clinical approach, I am referring to the cell orientation in respect to the beam, as described in the Methods Section. As discussed by Paganetti 2014, there is increased interest in evaluating the relationship between LET and RBE in clinical type conditions.

The survival results were transformed into RBE estimations. The Particle Irradiation Data Ensemble (PIDE) database (Friedrich et al. 2013) contains results of in-vitro cell survival experiments gathered in a literature survey, which were performed pairwise after irradiation with photons and some ion species. The dose response curves are expressed by the linear-quadratic parameters. Initially, I compared my results with the ones obtained for all lung cancer cells since the low number of available results with the same cell line used in this thesis. The results can be seen in Figure 5.13. No experimental result is available for protons for these chosen cell lines in the PIDE database.

Subsequently, I separated the results in respect to the different ion types used during the experiments, but this time plotting all available cell line results, Figures 5.14 and 5.15 compare the calculated RBE in my experiments to all available cell lines in the PIDE database.

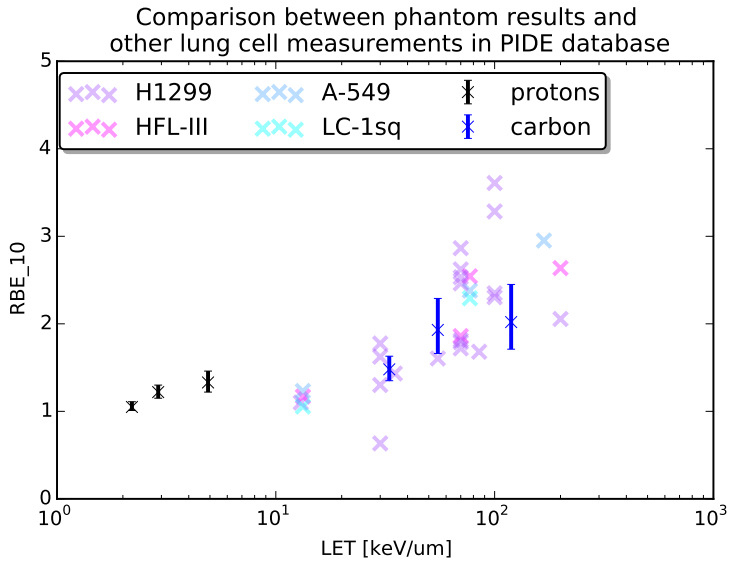

Figure 5.13. Obtained RBE_{10} versus LET for the cell line used and other different lung cell lines over different experimental results from PIDE database (Friedrich et al. 2013) with protons and carbon ion beams. No experimental results are available for protons for these chosen cell lines in the PIDE database.

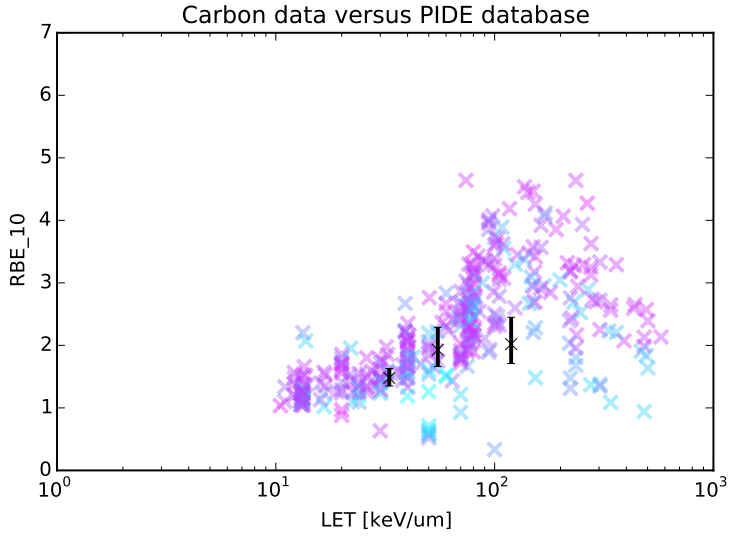

Figure 5.14. Obtained RBE_{10} versus LET for different cell lines over different experimental results with carbon ion beams from the PIDE database (Friedrich et al. 2013).

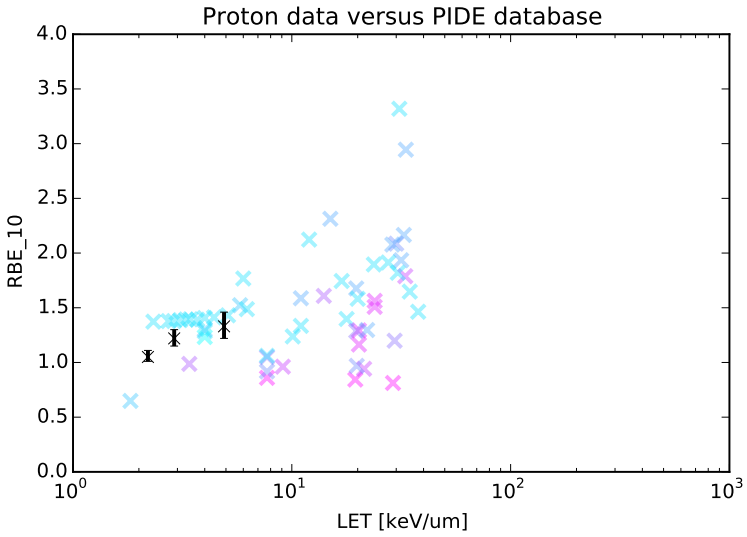

Figure 5.15. Obtained RBE_{10} versus LET for different cell lines over different experimental results with proton beams from the PIDE database (Friedrich et al. 2013).

The comparison with the PIDE database shows that carbon and proton beams were found to be more effective in killing cells in culture than photons (i.e. RBE $>$ 1.0), which is consistent with my results. Although the calculated effectiveness of my experiments are within these literature results, when compared to the cell line used (all lung cancer cells were plotted in Figure 5.13), the killing efficiency obtained by my phantom were lower in respect to the LET in comparison to the literature for the cell line used, for example nearly 3 times the efficiency was reported for carbon beams (Ghosh et al. 2011) and 2 for protons (Wera et al. 2013), while my results shows a 2 and 1.2 times more effectiveness respectively for carbon and protons.

In order to evaluate the reasons behind the differences from my experimental result and the ones found in the literature with similar cell line, the contribution of the LET to effectiveness had to be studied. Evaluation of the variation of the LET along the beam path was necessary to evaluate the contribution of the LET to cell survival. Figure 5.16 shows the calculated dose averaged LET for both carbon ions (right) and protons (left). These LET values were calculated by the MC simulations using built in functions.

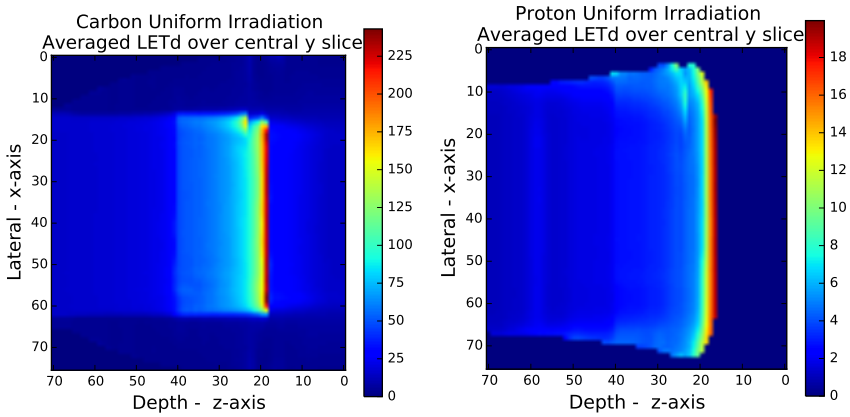

Figure 5.16. Calculated LET_d map for carbon ions (left) and proton beams (right). The image represents a slice through the central position in the phantom/ irradiation field. The dose averaged LET are in keV/um.

Figure 5.9 shows the difference between the calculated RBE_{20} at different positions along the SOBP. An increase in RBE is observed which corresponds to an increase in average LET as previously described in the literature (Paganetti 2014; Ghosh et al. 2011; Yoshimoto et al. 2015).

From the results it is possible to observe an increase of RBE between the two central wells (Figure 5.9). Although this increase of RBE along the wells is not statistically significant: 1.92 $[1.66; 2.29]$, 2.02 $[1.71; 2.45]$ for carbon ions and 1.22 $[1.15; 1.30]$, 1.33 $[1.22; 1.46]$ for protons. However by looking at Figure 5.9 and the LET distribution (Figure 5.16), a larger LET effect is demonstrated. The reason for the reduced effect, or contribution of the LET variation, is related to the size of the different wells. The effect shown by the cells depends on the average of the LET along each well. If a profile is taken as in Figure 5.16, and the average LET is calculated according to the different well size, it can be noted that there is a small variation in the LET for the currently well plate used (Figure 5.17).

Figures 5.17 to 5.21 show the effect of the spatial resolution of the multi-well plate in the variation of the average LETd.

It is important to mention that changing the bin size or the length of the SOBP has the same effect, i.e. by increasing the size of the bin (or the diameter of the well in the multi-well plate), the average LETd per bin decreases

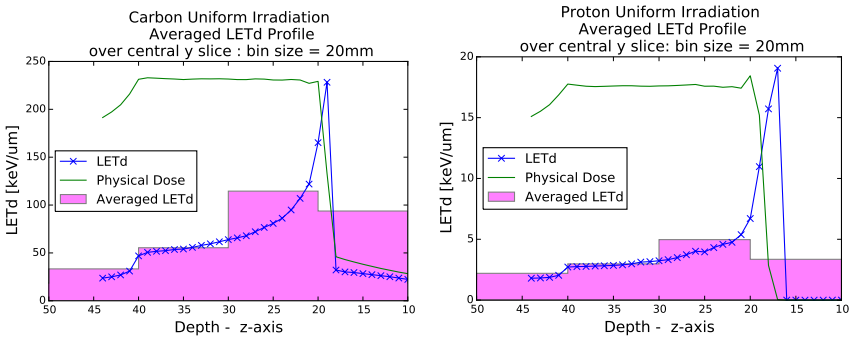

Figure 5.17. Calculated LET_d map for carbon ions (left) and proton beams (right). The image represents a slice through the central position in the phantom/ irradiation field. The averaged LETs were calculated for the 20mm well diameter. The dose averaged LET are in keV/um.

and the variation between the different depths is reduced. The same effect is noted by reducing the size of the SOBP. This explains why the data from the first experiment. In the first and last row in the SOBP the RBE obtained are statistically different in contrast to the result obtained in the second experiment.

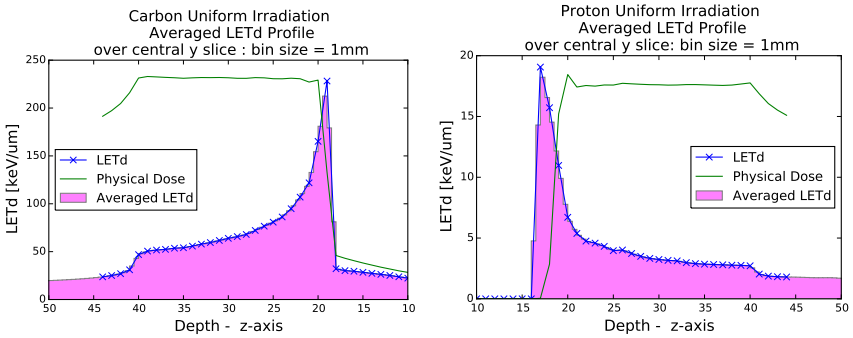

Figure 5.18. Calculated LET_d map for carbon ions (left) and proton beams (right). The image represents a slice through the central position in the phantom/ irradiation field. The averaged LETs were calculated for the 1 mm well diameter. The dose averaged LET are in keV/um.

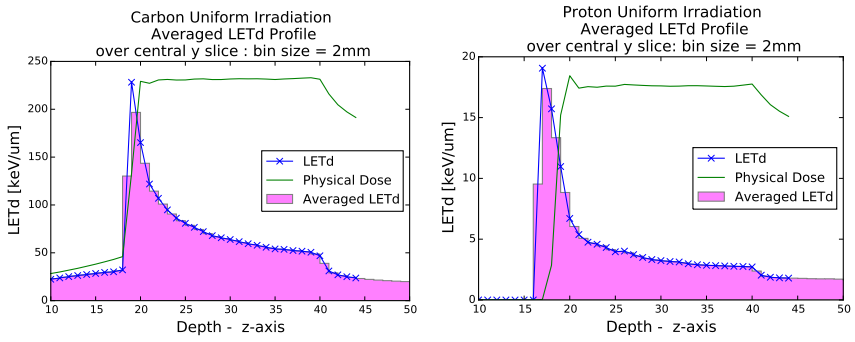

Figure 5.19. Calculated LET_d map for the carbon ions (left) and proton beams (right). The image represents a slice through the central position in the phantom/ irradiation field. The averaged LETs were calculated for the 2 mm well diameter. The dose averaged LET are in keV/um.

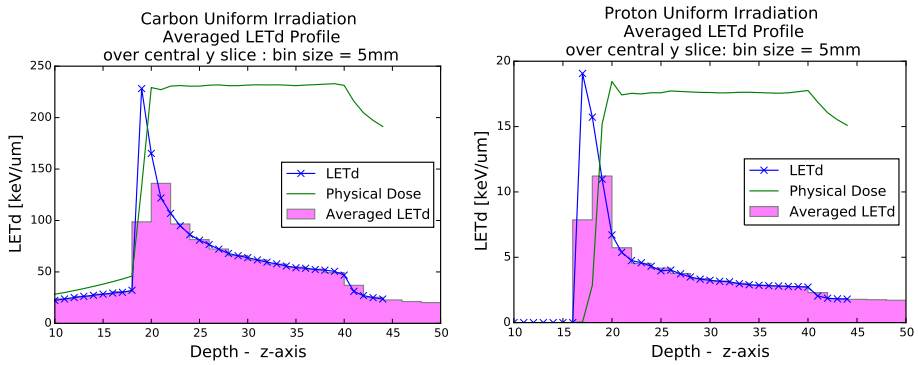

Figure 5.20. Calculated LET_d map for the carbon ions (left) and proton beams (right). The image represents a slice through the central position in the phantom/ irradiation field. The averaged LETs were calculated for the 5 mm well diameter. The dose averaged LET are in keV/um.

As discussed in previous chapters, dosimetric uncertainties affect the results by either not being able to correctly evaluate the dose profile, or by disturbing the beam which will irradiate the cells. This leads the absorbed dose in the cell compartment being wrongly reported which weakens the biological results.

In respect to the correlation of cell survival and dose profile represented in Figure 5.12, the phantom is able to reproduce cell survival in respect to the dose deposition. This reproducibility is also seen for the different doses in Figure 5.22.

As mentioned, other groups use set-ups that are also capable of evaluating

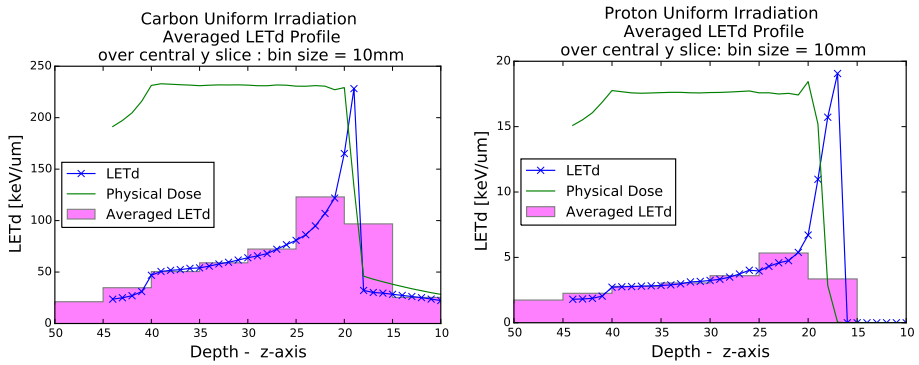

Figure 5.21. Calculated LET_d map for the carbon ions (left) and proton beams (right). The image represents a slice through the central position in the phantom/ irradiation field. The averaged LETs were calculated for the 10 mm well diameter. The dose averaged LET are in keV/um

the beam delivery. The closest to this capability present in the literature is the work of Mitaroff et al. 1998 and Bert et al. 2010. Figure 5.23 present the results obtained by such phantoms. The set-up presented by Barazzuol et al. 2012 would correctly describe the dose profile in passive scattering systems which is not the case for the work presented in this thesis.

The main drawback of these designs, as described previously in Table 2.2, is the inability to perform multiple irradiations in the same cell preparation batch (which could potentially remove the huge variability in cell survival), or to obtain the dosimetric information without disturbing the beam path, as presented in the work by Mitaroff et al. and Bert et al. The work by Bert et al. set forth the benefits of using commercial tools for biological irradiations, such as the reduced reported uncertainties, but failed to provide the in-beam dosimetry which can be obtained by my design. The work of Mitaroff et al., in addition to not using commercially available tools for cell plating, uses detectors with a higher uncertainty for ion beams (protons and carbon).

The main novelty of my design is that these two limitations in the final dosimetric evaluation of the phantom and cell compartment were accounted for during the phantom development (Chapter 3). My phantom is also able to accommodate different detectors for in-beam dosimetry.

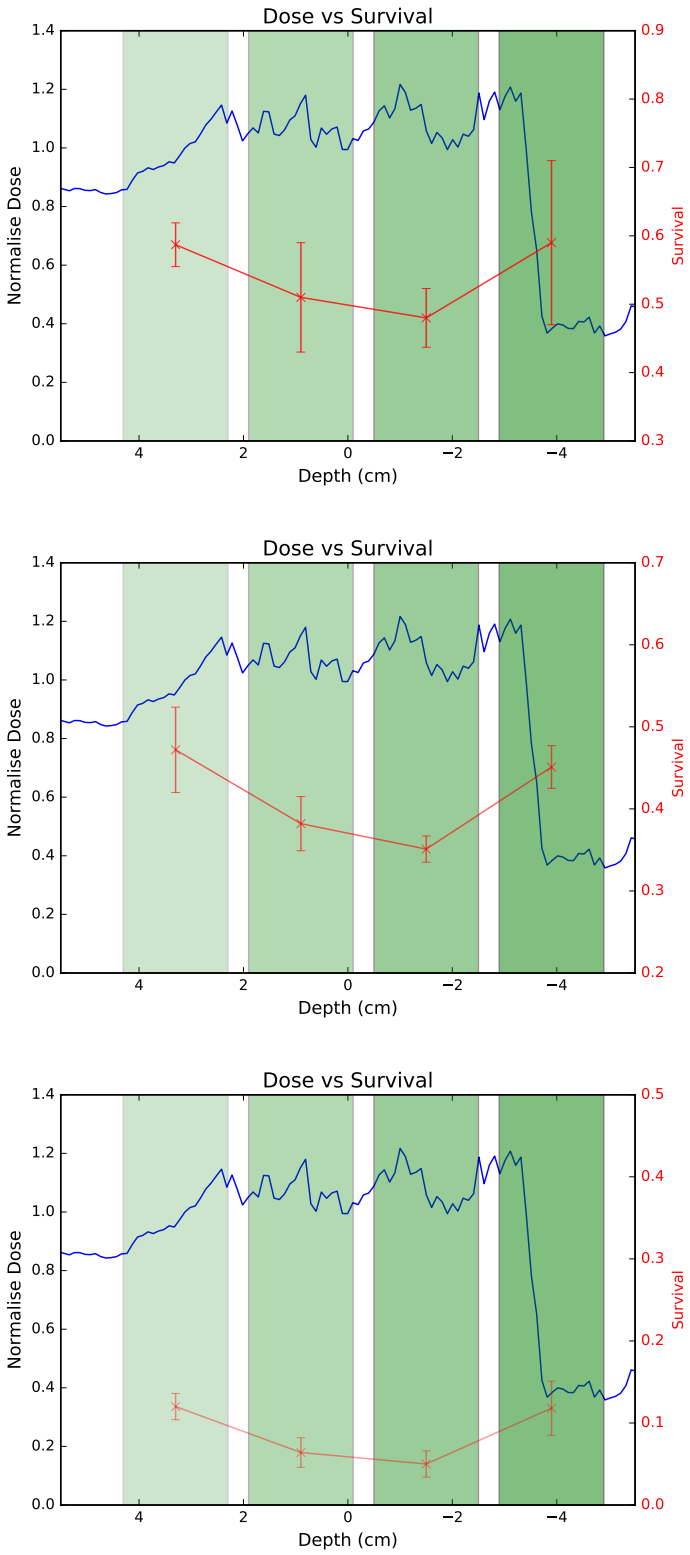

Figure 5.22. Correlation of dose profile and cell survival for different irradiation doses. Similar to Figure 5.12, these plots show the reproducibility of the phantom in correlating cell survival and dose deposition. Plots for different doses at the SOBP, from 1.5, 2.0 and 4.0 Gy respectively, top to bottom.

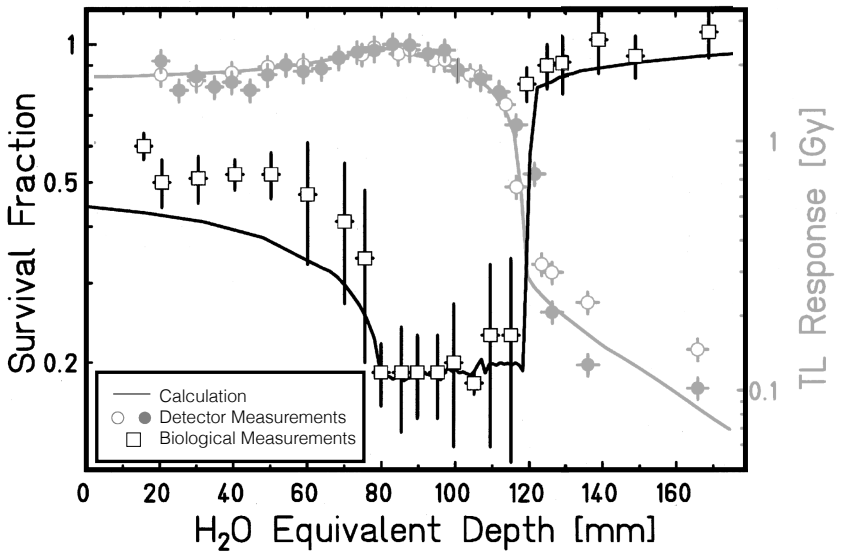

Figure 5.23. Correlation of dose profile and cell survival found in the literature. Similar to the result obtained by my proposed design higher dose deposition yields lower survival. The different dose at entrance, target area and exit dose can be clearly seen. Modified figure from Mitaroff et al. 1998. TL response represent the thermo-luminescence detectors

5.6 Conclusion

The use of ion beams (protons included) is initially motivated by the selective depth-dose profile, which is primarily advantageous for treating targets close to organs of risk. In addition to this superior dose delivery conformity, the biological effectiveness of ions is also known to be superior in comparison to photon irradiation, either represented by the supported constant 1.1 RBE value, for protons, or by the variable increased RBE as obtained by different biological experiments and used clinically by mathematical models. A recent review (Tommasino and Durante 2015) summarises that the complexity contained in the RBE parameter might be drastically underestimated by the use of a constant value of RBE. This therefore demonstrates the need for multiple cell irradiation experiments to correlate the responses from different radiation types.

The aim of this chapter was to study the viability of the phantom to perform these much needed radiobiological experiments. This was done by evaluating

both the biological effectiveness (RBE estimation) for different radiation types (protons and carbon ions) and the contribution of the LET to this effectiveness, and more importantly, by evaluating the correlation of cell survival response and deposited dose.

During the RBE estimation, similar behaviour as contained in the literature was obtained. I was able to show that using the phantom I could obtain a higher biological effectiveness for both protons and carbon ions in comparison to photons. As expected, the final effectiveness was lower, due to the LET distributions, averaging a large range of LET along the well area which is not the case for current radiobiological experiments. The initial assessment of the LET-RBE-Dose demonstrated that it is possible to use the cell survival data obtained with the phantom and perform further investigations within the same irradiation set-ups. This allows for multivariate analysis of the cell survival with fewer irradiations. Furthermore, the use of commercially available cell culture tools used as inserts in the phantom allow for multiple irradiations within the same period, thereby reducing the number of irradiations and the introduction of biological uncertainties.

In conclusion, the design showed that it was capable of benefiting from the use of commercial tools for performing multiple cell irradiation. It is also able to accommodate the most accurate clinically available dosimeters, and by doing so, it is able to accurately correlate cell survival and deposited dose.

Chapter 6

Overall Conclusion and Outlook

In complex techniques such as protons or ion beam therapy, the success or failure of the treatment is determined by several factors relating to physical properties, understanding of biological properties and limitations arising from the delivery of the treatment. In this context, a precise and consistent set of dosimetric tools for radiobiological experiments has a clear impact on the efficiency of protons and ion beam therapy, as it reduces uncertainties in further biological and clinical studies. This thesis provides an insight into the research and development towards the construction and testing of a biological dosimetric phantom for radiobiological experiments.

A literature review was performed in order to evaluate the need for such a device and its relevance. It was possible to conclude that in order to improve our knowledge of enhanced biological effectiveness, which is necessary to support clinical proton and ion beam applications, more dedicated tools needed to be developed. This is particularly true in cases where there are observed disadvantages with some experimental set-ups that can be reduced, such as associated dosimetric and biological limitations with the chosen detector or biological compartment. A phantom with dosimetric information about the delivered beam would allow radiobiological experiments to achieve the necessary reliability and reproducibility (Desrosiers et al. 2013). The main advantage of such devices is the precision in which dose and cell survival can be correlated. To my knowledge, my phantom is the only radiobiological phantom that has

had both its physical (dosimetric) and biological capabilities as well as possible limitations evaluated during the design stages. All that in a device which is easy to use and transportable.

A comprehensive overview of the limitations present in the current radiobiological set-ups was developed during the initial design stages, focusing on the improvements that could be achieved by the proposed device.

I determined the effect that detectors and manufacturing limitations would have on the obtained dose distributions. The MC analysis showed that 95.3% (98.2%, 91.2, 96.5% at the centre of the SOBP and 2 cm before and after respectively) of the points in the desired region are within the confidence interval of 95%. A few points fell out of this confidence interval, which could be explained by statistical fluctuations and poor uniformity of the original beam profile. Despite these rare anomalies, the results can be seen as satisfactory since all points lie within 1.0% of the nominal value, which corresponds well with dosimetry requirements. The only introduced limitation was the chosen material, PMMA, but I was able to show that this limitation could be overcome (Figure 3.8) by accounting for the correct WEPL (Jaekel et al. 2001a). Confidence in the phantom is clearly enhanced after studying its limitations. Even with different irradiations at different facilities, the results agree remarkably well within the uncertainties of the detector used. It may be that some systematic uncertainties were not accurately estimated or some of them were not considered, but there are no indications that this may have had a significant impact. Moreover, it was demonstrated that the variation between irradiation fields did not present a issue in this agreement. The only parameter that required further considerations is the beam uniformity during the irradiation plan calculations.

The multivariate cell study (RBE and LET versus survival) is also noteworthy. Different authors have previously discussed the importance of evaluating and correlating LET, RBE and cell survival (Sørensen et al. 2011; Jones 2015b; Tommasino and Durante 2015; Durante 2014; Paganetti 2014). To my knowledge, this is the very first study to address both biological and dosimetrical capabilities and limitations during development of a biological phantom. By

using the designed phantom I was able to obtain good agreement between the obtained dose deposition measurements by ionisation chambers and TPS/MC calculations in relation to local QA procedures at different centres (Tables 4.2 to 4.5). The desired accuracy for the dosimetric uncertaintity of the phantom was determined to be close to 3%, limited by the relative uncertainty of the ionisation chamber with respect to ions (Karger et al. 2010). For all performed experiments, the average dose deviation between ionisation measurements and dose calculations are well within this requirement, ranging from 1.05% to 2.39%. This shows that appropriate steps had been taking to account for the different limitations of the phantom.

In addition to its proven dosimetrical capabilities, the phantom was evaluated in a radiobiological viability study. RBEs were evaluated as part of the biological response. A superior effectiveness was obtained for both protons and carbon ions compared to the literature (Wera et al. 2013; Ghosh et al. 2011). This phantom can be used in radiobiological experiments for survival dose measurements and possibly to correlate irradiation dose to RBE and LET. Improved spatial resolution by the use of smaller well sizes would be needed in order to average the LET between smaller ranges. The performance of the phantom was similar to other methods used, i.e. improved sensitivity was observed for ion beams in relation to photon, but in order to compare whether the level of this efficiency is the same, future irradiations would need to take into account the LET at well positions.

In order to benefit fully from the capabilities described above the main sought after feature of the phantom is its ability to correlate the physical and biological processes. This feature was demonstrated in Figure 5.12. (Desrosiers et al. 2013) Since the phantom was able to correctly correlate the calculated dose distribution and therefore obtain a grid dosimetry at the cell compartment.

6.1 Outlook

Herein an extensive, comprehensive, and systematic work was performed concerning the biological dosimetric capabilities of the designed phantom. The overall errors associated with the phantom are due to its dosimetric and radiobiological uncertainties.

The dosimetric errors are either associated with the dose delivery, dose calculation or measurement. Dose delivery errors can be introduced by limitations in the delivery system by uncertainties in delivering the required number of ions, and the beam position and characteristics (for example beam width and energy). Intrinsically dose calculations are thought to be accurate, but it is possible that systematic deviations between the model used in treatment planning and the delivered beams are present. These systematic errors originated from uncertainties in the description of the Bragg curves or the lateral profiles, uncertainties in the modelling of the multiple Coulomb scattering or the limited knowledge of the fragmentation processes. Lastly, dose measurement errors are associated with uncertainties resulting from the stability and reproducibility of the ionisation chamber, the electrometer and setting up the phantom and positioning the ionisation chambers within the phantom correctly.

In regard to radiobiological uncertainties, the systematic errors can contribute to increased errors in the cell survival results. These uncertainties are generally associated with handling and counting of the cell cultures and can occur during and after irradiation. An extra limitation of the measurements presented in this thesis is that repetition of survival per dose was taken from the same irradiation, from different wells at the same depth. A future step is to perform more survival measurements and evaluate whether using the same irradiation at different wells are sufficient or if this would introduce further errors.

In this thesis, I was able to shown that this design can be used to aid radiobiology experiments at different centres. Dosimetric consistence is a key requirement by guidelines from major health agencies (e.g. the National Cancer

Institute - NCI) in order to participate at clinical trials, which are the foundation of the much-needed evidence-based medicine. Consistency of treatments at different sites also facilitates the transfer of results and patients between facilities aids future research developments and possibly patient mobility with these not so widely spread techniques. The work shown in this thesis shows the superior dosimetrical capability of the phantom in respect to other solutions found in the literature. The present study can contribute to the development of radiobiological solutions and their translation into further radiobiological experiments and clinical use. The developed phantom design can be used to further evaluate not only the physical dose and the different treatments, but also the varying conceptions of similar treatments used by different centres in calculating the biological dose to the patient. Although the proposed design is fully functional, improvements to experimental set-up can be made by:

- Increasing beam uniformity of delivered field: In order to reduce uncertainties introduced by non-uniformities in the dose distribution the irradiation plan can be recalculated. However, this would increase the irradiation time and therefore more beam time would be required. An alternative would be to offset these effects with different delivery techniques, such as passive scanning.

- The radiobiological output can be improved by using higher spatial resolution in cell survival sampling. At present the phantom survival results are not directly comparable with results found in literature due to the larger than average LET range used. In an effort to improve this weakness while still maintaining the ability to evaluate the survival effect in a mixed radiation field, the phantom has been adapted to hold different commercially available multi-well cell plates which provides the extra diminution required in the survival analysis. This allows multiple cell survival assessment for different dose deposition reducing the averaging effect of the LET variation.

Appendices

Appendix A

Phantom Description and Beam Orientation

A.1 Phantom Description

The phantom, shown in Figure A.1, consists of a PMMA block with dimensions of 240.0 ± 0.1 (H) x 240.0 ± 0.1 (W) x 146.0 ± 0.1 (L) mm^3, machined to accommodate a standard multi-well cell holder for cell irradiations and ionisation chambers pinpoint detectors at different positions.

Two sets of eleven holes of 10.5-mm diameter have been drilled to different depths in the phantom. The two sets of holes have been drilled symmetrically to the left and the right of the beam entrance. They have been conceptually conceived to host pinpoint ionisation chambers. The positions of the holes are such that they populate uniformly a Spread-Out-Bragg-Peak (SOBP) of up to 12 cm long. In cases where centres did not have all the pinpoint chambers, the empty cylindrical cavities were filled with mock chambers of the same PMMA material. The phantom was machined to host the PTW PinPoint Model n31014, 0.015 cc volume. The shape of the deep end of each hole matches the tip of the detector to avoid air-gap, which could affect the dose deposition. The design enables on-line information about the requested SOBP to be obtained from the available detector positions at the same time as cell cultures are irradiated. The

phantom offers two options: the first concentrates on the physical properties of the delivered beam and the second delivers biological response information. By using the described methods, multiple irradiations can be performed at the same beam time and on the same day. This will facilitate high-throughput data acquisition from biological samples prepared in the desired experimental setting.

Figure A.1. Photography of the phantom and multi-well plates.

Figure A.2 represents a three-dimensional model of the phantom with the detector and cell compartment positions shown.

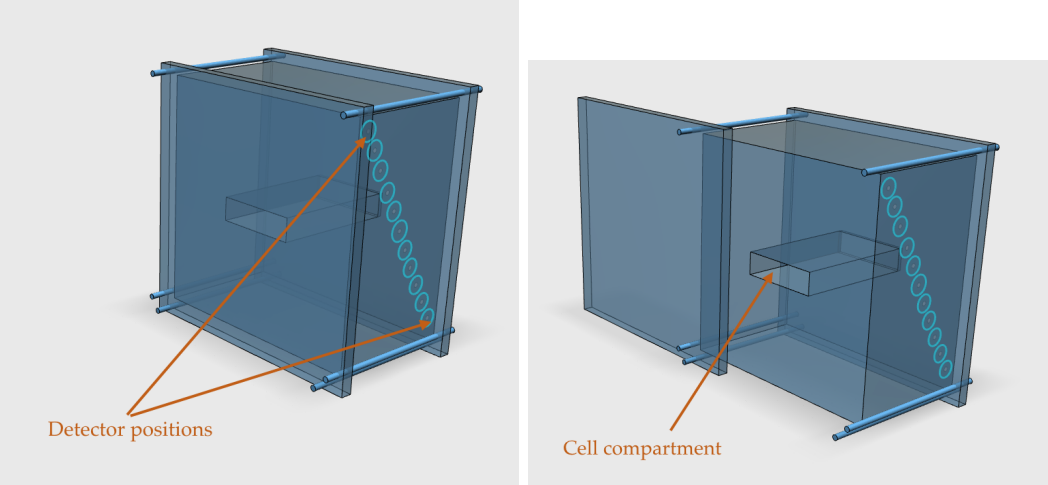

Figure A.2. 3 dimensional model of the phantom with labelled detector and cell compartment locations.

A.2 Beam Orientation

As described previously, one of the phantom's uniqueness is the orientation of the beam in relation to the cell plate. As shown in Figure A.3, the beam is parallel to the cell plate and therefore the radiobiological output is obtained at variable beam positions along the beam.

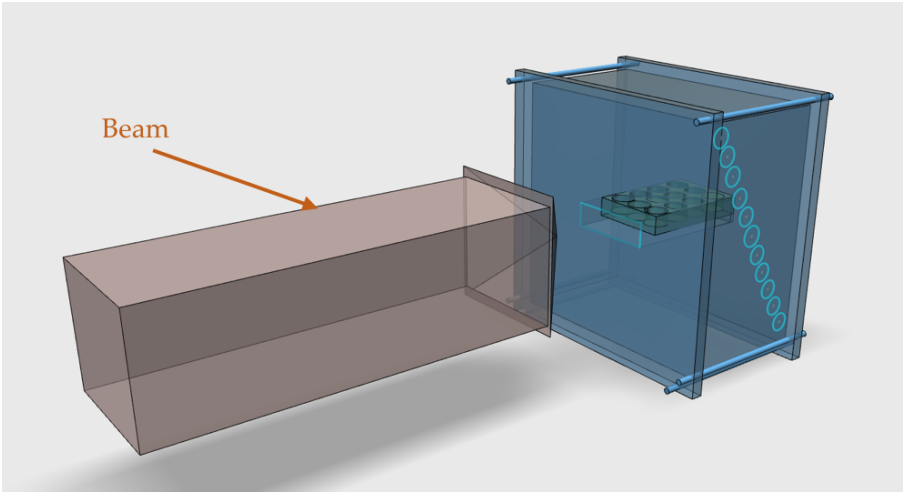

Figure A.3. Beam representation in respect to the phantom and cell plate.

Appendix B

FLUKA User Routines

B.1 Modified User Routine

In addition to the DDS description, FLUKA default user routine (which work as personalised computation scripts) was adapted in order to be able to correctly interpret irradiation plan files into the simulations. In FLUKA, in order to have different irradiation descriptions (orientation, starting location and particle fluence), a built-in function called source must be used. Users are able to personalise this function for their individual case. At a typical ion beam irradiation plan, the beam is divided into varying multiple starting locations and particle number per location.

This appendix describes the FLUKA user-routine that was modified in order to simulate irradiation plans in FLUKA. The initial part of the code was not modified.

The information contained in the irradiation plan was read as follows:

```
READ(RSTLUN, *) CDUMMY1, PATIENT_ID
READ(RSTLUN, *) CDUMMY1, CDUMMY2
READ(RSTLUN, *) CDUMMY1, PROJECTILE
WRITE(LOGLUN,*) 'projectile: ',CDUMMY1, PROJECTILE
```

```
      READ(RSTLUN, *) CDUMMY1, CHARGE
      WRITE(LOGLUN,*) 'CHARGE: ',CDUMMY1,CHARGE
      IF (CHARGE .EQ. 1) THEN
         RATIO_U=1.00727647D0
         WRITE(LOGLUN,*) 'CONVERSION FACTOR MEV/U -> MEV',
     &        RATIO_U
      ELSE IF (CHARGE .EQ. 6) THEN
         RATIO_U=ONEONE
         WRITE(LOGLUN,*) 'CONVERSION FACTOR MEV/U -> MEV',
     &        RATIO_U
      ELSE
         STOP 'NOT YET IMPLEMENTED FOR IONS DIFFERENT
     &        FROM P,12C'
      END IF

      READ(RSTLUN, *) CDUMMY1, MASS
      WRITE(LOGLUN,*) 'READ mass: ',CDUMMY1,MASS

      READ(RSTLUN, *) CDUMMY1, DUMMY1
      WRITE(LOGLUN,*) 'bolus', CDUMMY1, DUMMY1
      READ(RSTLUN, *) CDUMMY1, INTDUMMY1
      WRITE(LOGLUN,*) 'ripplefilter', CDUMMY1, INTDUMMY1
      READ(RSTLUN, *) CDUMMY1, SUBMACHINES
      WRITE(LOGLUN,*) 'LAST READ submachines: ',CDUMMY1,
     &     SUBMACHINES
      READ(RSTLUN, *) CDUMMY1, PARTICLE_MIN_ABS,
     &     PARTICLE_MAX_ABS, PARTICLE_TOTAL_ABS
      WRITE(LOGLUN,*) 'LAST READ particles: ',CDUMMY1,
     & PARTICLE_MIN_ABS, PARTICLE_MAX_ABS,
     &  PARTICLE_TOTAL_ABS
```

Each beam energy which is represented as a individual submachine was read.

```
      POINTS_TOTAL = 0

      DO I=1, SUBMACHINES
         READ(RSTLUN, *) CDUMMY1, INTDUMMY1, POINT_ENERGY,
     &    INTDUMMY2, POINT_FOCUS
         READ(RSTLUN, *) CDUMMY1, PARTICLE_MIN, PARTICLE_MAX,
     &    PARTICLE_TOTAL
         READ(RSTLUN, *) CDUMMY1, DUMMY1, DUMMY2
         READ(RSTLUN, *) CDUMMY1, POINTS

* loop over actual submachine starts here
        DO J=1, POINTS
         POINTS_TOTAL = POINTS_TOTAL + 1
         READ(RSTLUN, *) POINT_XY(1), POINT_XY(2),
         &      RST_PARTICLES
```

Positions are converted from *mm* to *cm* as used by the FLUKA code. The beam direction is then calculated then the orientation of FLUKA simulation was modified to be consistent with the orientation used by the TPS.

```
*Situation @ ISOCENTER
        POINT_XY(1) = POINT_XY(1)/TENTEN
        POINT_XY(2) = POINT_XY(2)/TENTEN
        POINT_XY(3) = ZERZER

        # energy GeV/c
        RST_ARRAY(1,POINTS_TOTAL) = POINT_ENERGY/1.D03*
          &  MASS*RATIO_U
```

```
      # x coordinate of RST point in FLUKA coordinates
      RST_ARRAY(2,POINTS_TOTAL) = ZERZER
      # y coordinate of RST point in FLUKA coordinates
      RST_ARRAY(3,POINTS_TOTAL) = ZERZER
      # z coordinate of RST point in FLUKA coordinates
      RST_ARRAY(4,POINTS_TOTAL) = RST_ORIGIN(3)

*     calculate the direction cosines here
*     SWAPPED X AND Y for consistency with
*     the TPS-VX PLAN
      TARGET_VECTOR(1) = POINT_XY(2) - RST_ORIGIN(2)
      TARGET_VECTOR(2) = POINT_XY(1) - RST_ORIGIN(1)
      TARGET_VECTOR(3) = POINT_XY(3) - RST_ORIGIN(3)

      R = SQRT(TARGET_VECTOR(1)**2 + TARGET_VECTOR(2)**2
     & + TARGET_VECTOR(3)**2 )

      # x direction cosine in FLUKA coordinates
      RST_ARRAY(5,POINTS_TOTAL) = TARGET_VECTOR(1)/R
      # y direction cosine in FLUKA coordinates
      RST_ARRAY(6,POINTS_TOTAL) = TARGET_VECTOR(2)/R
      # z direction cosine in FLUKA coordinates
      RST_ARRAY(7,POINTS_TOTAL) = TARGET_VECTOR(3)/R

* focus is converted from mm to cm and stored

      RST_ARRAY(8,POINTS_TOTAL) = POINT_FOCUS/TENTEN
      # number of particles to simulate
      RST_ARRAY(9,POINTS_TOTAL) = RST_PARTICLES
```

Lastly, is this information (beam energy, direction and position) is linked

to FLUKA variables for the simulation.

```
# Now linking into FLUKA variables:

* choose randomly which point will be simulated,
* it takes into account that each point has a
* different number of particles

  RAND3 = FLRNDM(DOUBLEDUMMY)
  PARTICLE_RAND = PARTICLE_TOTAL_ABS * RAND3
    PARTICLE_SUM  = ZERZER

  DO I=1, POINTS_TOTAL
    PARTICLE_SUM = PARTICLE_SUM + RST_ARRAY(9,I)
  IF (PARTICLE_SUM .GT. PARTICLE_RAND) THEN
        ACTUAL_POINT = I
      EXIT
  END IF
    END DO

* Kinetic energy of the particle (GeV)
  TKEFLK (NPFLKA) = RST_ARRAY(1,ACTUAL_POINT)
* Particle momentum
  PMOFLK (NPFLKA) = SQRT ( TKEFLK (NPFLKA) *
    & ( TKEFLK (NPFLKA) + TWOTWO * AM (IONID) ) )
  CALL FLNRRN (RGAUS0)
  PMOFLK(NPFLKA)=PMOFLK(NPFLKA)+WHASOU(1)*
    & PMOFLK(NPFLKA)*RGAUS0/S2FWHM

* Cosines (tx,ty,tz)
  TXFLK  (NPFLKA) = RST_ARRAY(5,ACTUAL_POINT)
```

```
      TYFLK    (NPFLKA) = RST_ARRAY(6,ACTUAL_POINT)
      TZFLK    (NPFLKA) = RST_ARRAY(7,ACTUAL_POINT)

*     Particle coordinates
      CALL FLNRR2 (RAND1,RAND2)
      XFLK     (NPFLKA) = RST_ARRAY(3,ACTUAL_POINT)+
     &           WHASOU(2)*RAND1/S2FWHM
      YFLK     (NPFLKA) = RST_ARRAY(2,ACTUAL_POINT)+
     &           WHASOU(2)*RAND2/S2FWHM
      ZFLK     (NPFLKA) = RST_ARRAY(4,ACTUAL_POINT)
```

The main modifications to the available code focused on the interpretation of irradiation plan information into FLUKA:

- location variables: $XFLK$, $YFLK$, $ZFLK$,
- kinetics energy variable: $TKFLK$, and
- number of particles to be simulated: *PARTICLESUM*.

The code was initially provided by the Medical Physics team from CNAO, but owing to the clinical use of CNAO simulations, their version of FLUKA and the one used in my simulations are different. In order to make it work in my FLUKA version, I had to update the links to the imported variable present in this user routine. Additionally, I had to correct the simulation reference, done with Flair, to match the TPS to orientation as the irradiation plan are generated in this reference orientation. At CNAO and other centres, this re-orientation is currently done during the post-processing stages.

Bibliography

Ableitinger, Alexander et al. (2013). "Dosimetry auditing procedure with alanine dosimeters for light ion beam therapy". In: *Radiotherapy and Oncology* 108.1, pp. 99–106 (cit. on p. 105).

Abler, D (2012). "Extending LEIR to provide ion beams for Bio-Medical Experiments". In: *Radiotherapy and Oncology* 102, S91–S92 (cit. on p. 111).

Arjomandy, B et al. (2010). "Verification of patient-specific dose distributions in proton therapy using a commercial two-dimensional ion chamber array". English. In: *Medical Physics* 37.11, p. 5831. DOI: 10.1118/1.3505011 (cit. on pp. 32, 36).

Barazzuol, L. et al. (2012). "In Vitro Evaluation of Combined Temozolomide and Radiotherapy Using X-Rays and High-Linear Energy Transfer Radiation for Glioblastoma". In: *Radiation Research* 177.5, pp. 651–662 (cit. on pp. 30, 35, 36, 77, 78, 107, 135).

Barazzuol, L. et al. (2013). "Evaluation of poly (ADP-ribose) polymerase inhibitor ABT-888 combined with radiotherapy and temozolomide in glioblastoma". In: *Radiation Oncology* 8.1, pp. 1–1 (cit. on p. 129).

Bert, C. et al. (2010). "Dosimetric precision of an ion beam tracking system". In: *Radiation Oncology* 5.61, pp. 1–9 (cit. on pp. 31, 32, 35, 36, 77, 107, 112, 135).

Bin, Jianhui et al. (2012). "A laser-driven nanosecond proton source for radiobiological studies". In: *Applied Physics Letters* 101.24, pp. 243701–5 (cit. on p. 26).

Boehlen, T T et al. (2012). "Investigating the robustness of ion beam therapy treatment plans to uncertainties in biological treatment parameters". In:

Physics in Medicine and Biology 57.23, pp. 7983–8004 (cit. on pp. 11, 24–26, 47, 83).

Boehlen, T T et al. (2014). "The FLUKA Code: Developments and Challenges for High Energy and Medical Applications". In: *Nuclear Data Sheets* 120.C, pp. 211–214 (cit. on p. 52).

Brenner, D J, L R Hlatky, P J Hahnfeldt, Y Huang, and R K Sachs (1998). "The linear-quadratic model and most other common radiobiological models result in similar predictions of time-dose relationships." In: *Radiation research* 150.1, pp. 83–91 (cit. on p. 20).

Britten, Richard A et al. (2013). "Variations in the RBE for Cell Killing Along the Depth-Dose Profile of a Modulated Proton Therapy Beam". In: *Radiation Research* 179.1, pp. 21–28 (cit. on pp. 25, 129).

Brusasco, C, B Voss, D Schardt, M Kraemer, and G Kraft (2000). "A dosimetry system for fast measurement of 3D depth-dose profiles in charged-particle tumor therapy with scanning techniques". In: *Nuclear Instruments and Methods in Physics Research Section B-Beam Interactions with Materials and Atoms* 168.4, pp. 578–592 (cit. on pp. 43, 58, 59).

Carabe, A., M. Moteabbed, N. Depauw, J. Schuemann, and H. Paganetti (2012). "Range uncertainty in proton therapy due to variable biological effectiveness". In: *Physics in Medicine and Biology* 57.5, pp. 1159–1172 (cit. on pp. 11, 28, 47, 103).

Carabe, Alejandro, Samuel Espana, Clemens Grassberger, and Harald Paganetti (2013). "Clinical consequences of relative biological effectiveness variations in proton radiotherapy of the prostate, brain and liver". In: *Physics in Medicine and Biology* 58.7, pp. 2103–2117 (cit. on pp. 24, 25, 47).

Churchill-Davidson, I (1966). "The Oxygen Effect in Radiotherapy". In: *Oncology* 20.Suppl. 1, pp. 18–29 (cit. on p. 11).

Ciocca, M et al. (2012). "OC-0057 Commissioning and quality assurance of scanned proton beams produced by a synchrotron for particle radiotherapy." In: *Radiotherapy and Oncology* 103, S22–S23 (cit. on p. 61).

Combs, E., N. Laperriere, and M. Brada (2013). "Proton radiation therapy for brain and skull base tumors". In: *Seminars Radiation Oncology* 23.2, pp. 120–126 (cit. on p. 24).

Combs, S., O. Jaekel, T. Haberer, and J. Debus (2010). "Particle therapy at the Heidelberg Ion Therapy Center (HIT) – Integrated research-driven university-hospital-based radiation oncology service in Heidelberg, Germany". In: *Radiotherapy and Oncology* 95.1, pp. 41–44 (cit. on p. 82).

Combs, S E et al. (2012). "In vitro evaluation of photon and carbon ion radiotherapy in combination with chemotherapy in glioblastoma cells". In: *Radiation Oncology* 7.1, p. 9. DOI: 10.1186/1748-717X-7-9 (cit. on pp. 30, 35, 36, 76, 107, 129).

Dale, Roger (2004). "Use of the Linear-Quadratic Radiobiological Model for Quantifying Kidney Response in Targeted Radiotherapy". In: *Cancer Biotherapy and Radiopharmaceuticals* 19.3, pp. 363–370 (cit. on pp. 20, 21).

Demizu, Yusuke, Osamu Fujii, Hiromitsu Iwata, and Nobukazu Fuwa (2014). "Carbon ion therapy for early-stage non-small-cell lung cancer." In: *BioMed Research International* 2014.2, pp. 727962–9 (cit. on p. 129).

Desrosiers, Marc et al. (2013). "The Importance of Dosimetry Standardization in Radiobiology". In: *Journal of Research of the National Institute of Standards and Technology* 118, p. 403 (cit. on pp. 16, 28, 30, 47, 96, 100, 103, 139, 141).

Dorfman, D D and E Alf Jr (1969). "Maximum-likelihood estimation of parameters of signal-detection theory and determination of confidence intervals rating-method data". In: *Journal of Mathematical Psychology* 6.3, pp. 487–496 (cit. on p. 39).

Dosanjh, Manjit, Manuela Cirilli, and Sparsh Navin (2015). "Introduction to the ECs Marie Curie Initial Training Network Project: The European Training Network in Digital Medical Imaging for Radiotherapy (ENTERVISION)." In: *Frontiers in Oncology* 5, p. 265 (cit. on p. 26).

Durante, M (2014). "New challenges in high-energy particle radiobiology". In: *The British Journal of Radiology* 87.1035, p. 20130626 (cit. on pp. 110, 140).

Elsaesser, T. et al. (2010). "Quantification of the Relative Biological Effectiveness for Ion Beam Radiotherapy: Direct Experimental Comparison of Proton and Carbon Ion Beams and a Novel Approach for Treatment Planning". In: *International Journal of Radiation Oncology*Biology*Physics* 78.4, pp. 1177–1183 (cit. on pp. 31, 33, 35, 36, 76, 107, 129).

Emmett, M B (1975). *The MORSE Monte Carlo radiation transport code system.* Tech. rep. ORNL-4972 (cit. on p. 52).

Ferrari, A, P R Sala, A Fasso, and J Ranft (2005). *FLUKA: A multi-particle transport code (program version 2005).* Geneva: CERN (cit. on p. 52).

Fix, Michael K et al. (2013). "Macro Monte Carlo for dose calculation of proton beams". In: *Physics in Medicine and Biology* 58.7, pp. 2027–2044 (cit. on p. 50).

Fossati, P et al. (2012). "Dose prescription in carbon ion radiotherapy: a planning study to compare NIRS and LEM approaches with a clinically-oriented strategy". In: *Physics in Medicine and Biology* 57.22, pp. 7543–7554. DOI: 10.1088/0031-9155/57/22/7543 (cit. on pp. 23, 25).

Franken, N A P, H M Rodermond, J Stap, J Haveman, and C van Bree (2006). "Clonogenic assay of cells in vitro". In: *Nature Protocols* 1.5, pp. 2315–2319. DOI: 10.1038/nprot.2006.339 (cit. on p. 115).

Friedrich, T, U Scholz, T Elsaesser, M Durante, and M Scholz (2013). "Systematic analysis of RBE and related quantities using a database of cell survival experiments with ion beam irradiation". In: *Journal of Radiation Research* 54.3, pp. 494–514 (cit. on pp. 32, 129–131).

Ghosh, Somnath, Himanshi Narang, Asitikantha Sarma, and Malini Krishna (2011). "DNA damage response signaling in lung adenocarcinoma A549 cells following gamma and carbon beam irradiation". In: *Mutation Research - Fundamental and Molecular Mechanisms of Mutagenesis* 716.1-2, pp. 10–19 (cit. on pp. 131, 132, 141).

Giantsoudi, Drosoula et al. (2015). "Validation of a GPU-based Monte Carlo code (gPMC) for proton radiation therapy: clinical cases study". In: *Physics in Medicine and Biology*, pp. 2257–2269 (cit. on p. 50).

Goodhead, D. (1999). "Mechanisms for the Biological Effectiveness of High-LET Radiations". In: *Journal of Radiation Research* 40.SUPPL, S1–S13. DOI: 10.1269/jrr.40.S1 (cit. on pp. 14, 129).

Guebitz, C.S., W. Kraft-Weyrather, and C. H. von Neubeck (2007, Sep 20.). *Irradiation verification apparatus for radiation therapy equipment and procedures for handling the same.* Gesellschaft fur Schwerionenforschung. (cit. on p. 33).

Gupta, N, K Lamborn, and D F Deen (1996). "A statistical approach for analyzing clonogenic survival data". In: *Radiation Research* 145.5, p. 636 (cit. on pp. 37, 38).

He, P B, Q Li, X G Liu, F Ye, and Z Y Dai (2012). "Experimental measurement of the correlation between CT number and heavy ion range". In: *Chinese Physics C* 36.10, pp. 954–957. DOI: 10.1088/1674-1137/36/10/006 (cit. on pp. 51, 59).

Herrmann, R, O Jaekel, H Palmans, P Sharpe, and N Bassler (2011). "Dose response of alanine detectors irradiated with carbon ion beams". English. In: *Medical Physics* 38.4, p. 1859. DOI: 10.1118/1.3560459 (cit. on p. 44).

Hoffmann, W, J Bienen, D Filges, and T Schmitz (1999). "TLD-300 dosimetry in a 175 MeV proton beam". In: *Radiation Protection Dosimetry* 85.1-4, pp. 341–343 (cit. on p. 35).

IAEA (2000). *Absorbed dose determination in external beam radiotherapy: An international code of practice for dosimetry based on standards of absorbed dose to water.* Tech. rep. Vienna (cit. on pp. 14, 44, 84).

— (2010). *Radiation Biology: A Handbook for Teachers and Students.* Tech. rep. Vienna (cit. on pp. 13, 15, 17, 20).

ICRU (2007). "Prescribing, recording, and reporting proton-beam therapy: contents." In: *Journal of the ICRU* 7.2, NP (cit. on p. 110).

Jaekel, O, G H Hartmann, C P Karger, P Heeg, and J Rassow (2000). "Quality assurance for a treatment planning system in scanned ion beam therapy". In: *Medical Physics* 27.7, pp. 1588–14 (cit. on p. 105).

Jaekel, O, C Jacob, D Schardt, C P Karger, and G H Hartmann (2001a). "Relation between carbon ion ranges and x-ray CT numbers". English. In: *Medical Physics* 28.4, p. 701 (cit. on pp. 51, 59, 76, 140).

Jaekel, O, M Kraemer, C P Karger, and J Debus (2001b). "Treatment planning for heavy ion radiotherapy: clinical implementation and application." In: *Physics in Medicine and Biology* 46.4, pp. 1101–1116 (cit. on p. 29).

Jaekel, Oliver, Alfred R Smith, and Colin G Orton (2013). "The more important heavy charged particle radiotherapy of the future is more likely to be with heavy ions rather than protons". In: *Medical Physics* 40.9, pp. 090601–5 (cit. on p. 46).

Jones, B and R D Errington (2000). "Proton beam radiotherapy." In: *The British journal of radiology*, pp. 802–805 (cit. on p. 24).

Jones, B, A Carabe-Fernandez, and R G Dale (2006). "Calculation of high-LET radiotherapy dose required for compensation of overall treatment time extensions". In: *The British Journal of Radiology* 79.939, pp. 254–257 (cit. on p. 120).

Jones, Bleddyn (2015a). "A Simpler Energy Transfer Efficiency Model to Predict Relative Biological Effect for Protons and Heavier Ions". In: *Frontiers in Oncology* 5, pp. 1–9 (cit. on pp. 25, 111, 127).

— (2015b). "Towards Achieving the Full Clinical Potential of Proton Therapy by Inclusion of LET and RBE Models". In: *Cancers* 7.1, pp. 460–480 (cit. on pp. 111, 140).

Jones, Bleddyn, Roger G Dale, and Alejandro Carabe-Fernandez (2009). "Charged particle therapy for cancer: The inheritance of the Cavendish scientists?" In: *Applied Radiation and Isotopes* 67.3, pp. 371–377 (cit. on pp. 110, 127).

Jones, Eric, Travis Oliphant, Pearu Peterson, et al. (2001). *SciPy: Open source scientific tools for Python*. [Online; accessed 2014-06-03]. URL: `http://www.scipy.org/` (cit. on p. 39).

Kanematsu, N, Y Koba, and R Ogata (2013). "Evaluation of plastic materials for range shifting, range compensation, and solid-phantom dosimetry in carbon-ion radiotherapy". In: *Medical Physics* 40.4, pp. – (cit. on pp. 43, 58).

Karger, C P, O Jaekel, and G H Hartmann (1999). "A system for three-dimensional dosimetric verification of treatment plans in intensity-modulated radiotherapy with heavy ions." English. In: *Medical Physics* 26.10, pp. 2125–2132 (cit. on pp. 44, 62, 65, 96, 99).

Karger, C P, O Jaekel, H Palmans, and T Kanai (2010). "Dosimetry for ion beam radiotherapy". In: *Physics in Medicine and Biology* 55.21, R193–R234 (cit. on pp. 24, 35, 45, 46, 141).

Kogel, Albert Van Der and Michael Joiner (2010). *Basic Clinical Radiobiology*. Edward Arnold, pp. 20–25 (cit. on pp. 22, 23).

Kraemer, M and M Scholz (2000). "Treatment planning for heavy-ion radiotherapy: calculation and optimization of biologically effective dose." English. In: *Physics in Medicine and Biology* 45.11, pp. 3319–3330 (cit. on pp. 25, 70, 82, 83).

Kraemer, M et al. (2000). "Treatment planning for heavy-ion radiotherapy: physical beam model and dose optimization." English. In: *Physics in Medicine and Biology* 45.11, pp. 3299–3317 (cit. on pp. 50, 59, 83).

Kraft, G. (2000). "Tumor therapy with heavy charged particles". In: *Progress in Particle and Nuclear Physics* 45, S473–S544 (cit. on pp. 11–13).

Kraft, G., M. Kraemer, and M. Scholz (1992). "LET, track structure and models." In: *Radiat. Environ. Biophys* 31, pp. 161–180 (cit. on pp. 14, 17).

Lauber, K, A Ernst, M Orth, M Herrmann, and C Belka (2012). "Dying cell clearance and its impact on the outcome of tumor radiotherapy." In: *Frontiers in Oncology* 116.2. DOI: doi:10.3389/fonc.2012.00116 (cit. on pp. 17, 19).

Leek, Jeffrey T et al. (2010). "Tackling the widespread and critical impact of batch effects in high-throughput data". In: *Nature Publishing Group* 11.10, pp. 733–739 (cit. on pp. 29, 34, 111).

Lima, T. V. M. et al. (2016). "Monte Carlo calculations supporting patient plan verification in proton therapy". In: *Frontiers in Oncology* 6:62. DOI: 10.3389/fonc.2016.00062 (cit. on p. 53).

Lomax, A. et al. (2004). "Treatment planning and verification of proton therapy using spot scanning: Initial experiences". English. In: *Medical Physics* 31.11, p. 3150 (cit. on p. 25).

Mairani, A et al. (2010). "The FLUKA Monte Carlo code coupled with the local effect model for biological calculations in carbon ion therapy". In: *Physics in Medicine and Biology* 55.15, pp. 4273–4289 (cit. on pp. 52, 53).

Mairani, A et al. (2013). "A Monte Carlo-based treatment planning tool for proton therapy". In: *Physics in Medicine and Biology* 58.8, pp. 2471–2490 (cit. on pp. 52, 53).

Martišíková, Mária and Oliver Jäkel (2010). "Dosimetric properties of Gafchromic® EBT films in monoenergetic medical ion beams". In: *Physics in Medicine and Biology* 55.13, pp. 3741–3751 (cit. on p. 35).

McKinnon, Peter J (2009). "DNA repair deficiency and neurological disease". In: *Nature Reviews Neuroscience* 10.2, pp. 100–112 (cit. on pp. 22, 23).

Miller, R C, M Lodge, M H Murad, and B Jones (2013). "Controversies in Clinical Trials in Proton Radiotherapy: The Present and the Future". In: *YSRAO* 23.2, pp. 127–133 (cit. on p. 24).

Mitaroff, A, W Kraft-Weyrather, O B Geiss, and G Kraft (1998). "Biological verification of heavy ion treatment planning." English. In: *Radiation and Environmental Biophysics* 37.1, pp. 47–51 (cit. on pp. 33, 35, 36, 77, 78, 107, 129, 135, 137).

Molinelli, S et al. (2013). "Dosimetric accuracy assessment of a treatment plan verification system for scanned proton beam radiotherapy: one-year experimental results and Monte Carlo analysis of the involved uncertainties". In: *Physics in Medicine and Biology* 58.11, pp. 3837–3847 (cit. on pp. 35, 44, 55–57, 61, 77, 82, 85, 107).

Niemantsverdriet, Maarten et al. (2012). "High and low LET radiation differentially induce normal tissue damage signals." In: *International journal of*

radiation oncology, biology, physics 83.4, pp. 1291–1297 (cit. on pp. 110, 129).

Paganetti, H (2012). "Range uncertainties in proton therapy and the role of Monte Carlo simulations". In: *Physics in Medicine and Biology* 57.11, R99–R117 (cit. on pp. 28, 59, 103).

— (2014). "Relative biological effectiveness (RBE) values for proton beam therapy. Variations as a function of biological endpoint, dose, and linear energy transfer". In: *Physics in Medicine and Biology* 59.22, R419–R472 (cit. on pp. 36, 111, 129, 132, 140).

Paganetti, H et al. (2002). "Relative biological effectiveness (RBE) values for proton beam therapy". In: *International Journal of Radiation Oncology* Biology* Physics* 53.2, pp. 407–421 (cit. on pp. 11, 24, 46).

Parcerisa, D S (2012). "Experimental and computational investigation of water-to-air stopping power ratio for ion chamber dosimetry in carbon ion radiotherapy". PhD thesis. University of Heidelberg, Germany (cit. on p. 49).

Parodi, K et al. (2012). "Monte Carlo simulations to support start-up and treatment planning of scanned proton and carbon ion therapy at a synchrotron-based facility". In: *Physics in Medicine and Biology* 57.12, pp. 3759–3784 (cit. on pp. 52, 53).

Riboldi, M, R Orecchia, and G Baroni (2012). "Real-time tumour tracking in particle therapy: technological developments and future perspectives". In: *The Lancet Oncology* 13.9, e383–e391 (cit. on p. 112).

Rogers, D W O (2006). "Fifty years of Monte Carlo simulations for medical physics". In: *Physics in Medicine and Biology* 51.13, R287–R301 (cit. on p. 50).

Rossi, S (2011). "The status of CNAO". In: *The European Physical Journal Plus* 126.8, p. 78 (cit. on pp. 11, 55, 56, 82).

Sanchez-Doblado, F et al. (2007). "Uncertainty Estimation in Intensity-Modulated Radiotherapy Absolute Dosimetry Verification." In: *Interna-*

tional Journal of Radiation Oncology • Biology • Physics 68.1, pp. 301–310 (cit. on p. 106).

Scholz, M. (2000). "Heavy ion tumour therapy". In: *Nucl. Instr. and Meth. in Phys. Res*, pp. 76–82 (cit. on p. 129).

Schulz-Ertner, D. et al. (2007). "Effectiveness of Carbon Ion Radiotherapy in the Treatment of Skull-Base Chordomas". In: *International Journal of Radiation Oncology*Biology*Physics* 68.2, pp. 449–457 (cit. on p. 129).

Schulz-Ertner, Daniela, Oliver Jaekel, and Wolfgang Schlegel (2006). "Radiation therapy with charged particles." In: *YSRAO* 16.4, pp. 249–259 (cit. on p. 11).

Sørensen, B., J. Overgaard, and N. Bassler (2011). "In vitro RBE-LET dependence for multiple particle types". In: *Acta Oncologica* 50.6, pp. 757–762 (cit. on pp. 16, 140).

Spielberger, B, M Scholz, M Kraemer, and G Kraft (2002). "Calculation of the x-ray film response to heavy charged particle irradiation". In: *Physics in Medicine and Biology* 47.22, p. 4107 (cit. on p. 44).

Tinganelli, W et al. (2013). "Influence of acute hypoxia and radiation quality on cell survival". In: *Journal of Radiation Research* 54.suppl 1, pp. i23–i30 (cit. on pp. 14, 15, 33, 37, 38, 41, 110, 129).

Tommasino, Francesco and Marco Durante (2015). "Proton Radiobiology". In: *Cancers* 7.1, pp. 353–381 (cit. on pp. 137, 140).

Tsujii, H. and T. Kamada (2012). "A review of update clinical results of carbon ion radiotherapy". In: *Japanese Journal of Clinical Oncology* 42.8, pp. 670–685 (cit. on pp. 24, 46).

Verhaegen, Frank and Jan Seuntjens (2003). "Monte Carlo modelling of external radiotherapy photon beams." In: *Physics in Medicine and Biology* 48.21, R107–64 (cit. on p. 50).

Vlachoudis, V (2009). "FLAIR: A powerful but user friendly graphical interface for FLUKA". In: *International Conference on Mathematics, Computational Methods & Reactor Physics (M&C 2009)* (cit. on p. 52).

Wera, Anne-Catherine, Anne-Catherine Heuskin, Helene Riquier, Carine Michiels, and Stephane Lucas (2013). "Low-LET Proton Irradiation of A549 Non-small Cell Lung Adenocarcinoma Cells: Dose Response and RBE Determination". In: *Radiation Research* 179.3, pp. 273–281 (cit. on pp. 110, 131, 141).

Wilson, R. R. (1946). "Radiological use of fast protons." In: *Radiology* 47, pp. 487–491 (cit. on p. 10).

Wink, Krista C J (2014). "Particle therapy for non-small cell lung tumors: where do we stand? A systematic review of the literature". In: *Frontiers in Oncology*, pp. 1–15 (cit. on p. 112).

Yajima, K, T Kanai, Y Kusano, and Shimojyu T (2009). "Development of a multi-layer ionization chamber for heavy-ion radiotherapy". In: *Physics in Medicine and Biology* 54.7, N107–114 (cit. on pp. 43, 58).

Yoshimoto, Y et al. (2015). "Carbon-ion beams induce production of an immune mediator protein, high mobility group box 1, at levels comparable with X-ray irradiation". In: *Journal of radiation research* 56.3, pp. 509–514 (cit. on p. 132).

Ziegler, J.F., M.D. Ziegler, and J.P. Biersack (2010). "SRIM - The stopping and range of ions in matter (2010)". In: *Nuclear Instruments and Methods in Physics Research B* 268, pp. 1818–1823. DOI: 10.1016/j.nimb.2010.02.091 (cit. on p. 59).

Zirkle, R.E. (1954). *The Radiobiological Importance of Linear Energy Transfer.* Vol. 1. New York: McGraw Hill, pp. 315–350 (cit. on pp. 14, 17).

Acronyms

FLUKA FLUktuierende KAskade or Fluctuating Cascade. 34, 35

BP Bragg Peak. 2, 39

CNAO Centro Nazionale di Adroterapia Oncologica. 35, 37, 39, 48, 49, 55, 57, 61

CT Computed Tomography. 34, 48, 65

DDS Dose Delivery Systems. 31, 35

DKFZ Deutsches Krebsforschungszentrum. 64

DNA Deoxyribonucleic acid. 1, 3, 4

HIT Heidelberg Ion Beam Therapy Center. 34, 39, 48, 49, 53–55, 61, 65

HT Hadron Therapy. 1, 5, 6, 13, 15, 32, 34, 37

LET Linear Energy Transfer. 2–5, 13, 16, 26, 29, 54, 93

MC Monte Carlo simulation. 31–34, 36, 38, 40–45, 48, 55, 58, 60, 68, 69, 79, 94, 95

PET Positron Emission Tomography. 34

PMMA Polymethyl Methacrylate. 35, 49, 51, 52, 67

QA Quality Assurance. 37

RBE Relative Biological Effectiveness. 4–6, 13, 15, 16, 20, 26, 29, 65, 93

SOBP Spread-out Bragg Peak. 2, 26, 40, 54

TPS Treatment Planning System. 31, 33–35, 37, 38, 40, 41, 45, 67

WEPL Water Equivalent Path Length. 33, 36, 39, 43, 46

List of Figures

List of Tables